博士論文 (要約)

Ab initio simulation of
the angle-resolved photoelectron spectrum
from atoms in intense laser pulses

(高強度レーザーパルスに照射された原子からの
角度分解光電子スペクトルの第一原理計算)

織茂　悠貴

Ab initio simulation of the angle-resolved photoelectron spectrum from atoms in intense laser pulses

Yuki Orimo

Department of Nuclear Engineering and Management,
Graduate School of Engineering, University of Tokyo

Abstract

Laser technologies to make laser pulses shorter and stronger have been drastically advanced in the past couple of decades. The technique enables us to generate high-intensity femtosecond (10^{-15} sec) laser pulses and leads to growth of the strong-field physics that studies nonperturbative and nonlinear optics: Perturbation treatment of laser-fields breaks down since the field intensity is too strong. Today, further shortening a duration of a laser pulse has been achieved, and it reaches a few tens of attoseconds (10^{-18} sec) in the state-of-the-art technology. Since the attosecond time scale corresponds to the timescale of electronic dynamics in atoms and molecules, it became possible to observe ultrafast electronic dynamics by using attosecond laser pulses as ultrashort camera shutters. The appearance of the attosecond laser pulses has arisen a new research area "attosecond physics", where observation and even control of the ultrafast electronic dynamics are studied.

Though such laser-induced electronic dynamics can be rigorously described by the time-dependent Schrödinger equation, solving it for multielectron systems poses a major challenge. To investigate many-electron dynamics in intense laser fields and attosecond light pulses by theoretical simulations, time-dependent multiconfiguration self-consistent field (TD-MCSCF) methods, which expresses a multielectron wave function as a superposition of Slater determinants, have been developed. A well-known theory of the TD-MCSCF methods is the multiconfiguration time-dependent Hartree-Fock (MCTDHF) method, which considers all the possible configurations for a given number of orbitals, and whose computational costs factorially increase against the number of electrons. To realize computationally less demanding simulations, the time-dependent complete-active-space self-consistent field (TD-CASSCF) method and the time-dependent occupation-restricted multiple-active-space (TD-ORMAS) method have been proposed. The former introduces orbital classification into doubly occupied core orbitals and fully correlated active orbitals. The latter further divides active orbitals into subgroups and restricts the electronic configurations. Flexible description of the wave function offered by the orbital classification and occupation restriction enables converged *ab initio* simulations of highly nonlinear, correlated multielectron dynamics in systems containing several tens of electrons.

While we have developed *ab initio* simulation methods, and enabled to simulate large systems which are considered as subjects of real experiments, direct comparison between ab initio simulations and experiments is still challenging. In particular, the extraction of photoelectron energy spectra (PES) and angle-resolved photoelectron energy spectra (ARPES), which are among important experimental probes for laser-matter interaction, is difficult. In principle, they could be calculated by projecting the departing photoelectron wave packet onto plane waves or Coulomb waves. This approach, however, requires retaining the complete wave function without being absorbed, leading to a huge simulation box and prohibitive computational cost. To circumvent this difficulty, the time-dependent surface flux (tSURFF) method has been developed, which extracts PES by integrating a wave function flux through a surface. Thus it allows one to use an absorbing boundary, that absorbs the photoelectron wave packet when it reaches the end of the spatial grid and suppresses unphysical reflections, bringing significant cost reduction. The tSURFF

method was first developed for single-electron systems and then applied to multielectron simulations with, e.g., the time-dependent configuration interaction singles method, and the time-dependent density functional theory. However. it has not been applied to general TD-MCSCF methods, which enable systematic improvement of accuracy, considering multielectron effects such as electronic correlation and the multiple ionization.

Against this background, we set our objective to develop a realtime *ab initio* simulation method to extract photoelectron spectra from multielectron atoms subject to intense laser fields, applying the tSURFF method to the TD-ORMAS method.

In order to take full advantage of the tSURFF method, not needing to hold the complete wave function within the simulation box, it is required to implement an efficient and accurate absorbing boundary. we have introduced exterior complex scaling (ECS) and infinite-range exterior complex scaling (irECS) as absorbing boundaries. ECS absorbs photoelectron wave packets, by analytically continuing the wave function into the complex plane without artificially modifying the system Hamiltonian or the wave function. Furthermore, the infinite-range exterior complex scaling (irECS) method significantly improves the efficiency over standard ECS by using an exponentially damped basis, thus moving the reflecting boundary to infinity. ECS and irECS as absorbing boundaries were originally formulated for single-electron systems. Thus We have applied these methods to the TD-ORMAS method, by neglecting the Coulomb force from electrons residing in the scaled region, which are far apart. However, we rigorously include all the other interactions (e.g. external fields, the nuclear potential and the Coulomb force from electrons in the unscaled region). In numerical demonstrations, we have shown that this implementation works well even when atoms undergo significant double ionization, and enables several times faster simulations than another absorbing boundary while keeping high accuracy.

To obtain photoelectron spectra from multiconfiguration wave functions, we have first introduced the photoelectron reduced density matrix, whose diagonal elements in the momentum space correspond to PES. In the application of the tSURFF method to the TD-ORMAS method, based on a physically reasonable assumption that the nuclear potential and interelectronic Coulomb interaction are negligible for photoelectron dynamics in the region distant from the nuclei, we have derived the equations of motion for the momentum amplitudes of each orbital. They contain an additional term arsing from interelectronic interaction compared with the single-electron case.

The present development has been applied to neon, beryllium, and argon atoms. In the simulations of a neon atom, we have compared PES obtained by the tSURFF method and directly projecting onto plain waves, and found that they completely agree with each other. This shows high accuracy of the tSRUFF method and the validity of the neglect of the electron-electron and nucleus-electron Coulomb interaction assumed in the application of the tSURFF method to the TD-ORMAS method. Next, we have computed one photon ionization cross section of a beryllium atom including Fano resonance. The overall structures of the cross sections obtained from TD-ORMAS simulations and experimental results show a good agreement, which indicates that we can correctly simulate the autoionization process, where electronic correlation plays an essential role. Finally, we have presented converged calculation of photoelectron spectra of above threshold ionization

(ATI) in an argon atom including electronic correlation, which would require prohibitive computational cost without tSURFF and irECS. Comparing the ATI ARPES computed with the time-dependent Hartree-Fock (TDHF) method and the converged one with the TD-ORMAS method, we have found a significant difference in a high energy region for which rescattering from the parent ion is involved, and especially in a direction perpendicular to the laser polarization. This indicates that electronic correlation is non-negligible in a detailed discussion of ATI ARPES.

As an extension of the development for atoms, we have presented an implementation of the TD-ORMAS method and the tSURFF method for molecules. From the theoretical perspective, this extension is straightforward. However, from a perspective of numerical simulations, the extension to molecular systems is not straightforward since the systems have no longer spherical symmetry, thus the spherical harmonics expansion, which efficiently discretizes atomic systems, is not suited for orbital discretization. In order to achieve efficient discretization of molecular systems, we have introduced the adaptive finite element method with multiresolution mesh in the Cartesian coordinate, which does not rely on the symmetry of systems. The concept of the multiresolution mesh is to discretize a region near the nuclei with fine mesh and the other regions with coarse mesh. As an absorbing boundary, we have implemented smooth exterior complex scaling, which is suited to the multiresolution method. For the demonstration of the present implementation, we have computed photoelecton momentum spectra from a hydrogen molecule. The positions of the computed single photon ionization peaks were found sufficiently close to the experimentally expected one. Moreover, comparing our results with photoelectron momentum spectra obtained by Fermi's golden rule, we have confirmed that photoelectron momentum spectra reflecting a molecular structure and laser polarizations are successfully computed by using our implementation.

In conclusion, to extract photoelectron spectra from laser-driven multielectron atoms, we have applied and implemented irECS and the tSURFF method to the TD-ORMAS method. In the application of the tSURFF method, we introduced photoelectron reduced density matrix, whose diagonal elements in the momentum space correspond to PES, and derived the equation of motion for the momentum amplitudes of each orbital. With this development, we have achieved highly accurate calculations of PES and ARPES with considerably reduced computational costs. In the simulations of an argon atom, we have revealed that electronic correlation affects the angular distribution of photoelectron yields in above threshold ionization spectra. Furthermore, we have extended the present development to molecular systems, and successfully computed photoelectron momentum spectra from a hydrogen molecule.

In this thesis, we have calculated photoelectron spectra without considering a state of the parent ion. However, in order to understand electronic dynamics after ionization or processes following photoemission, it is important to identify which ionic states are generated and how they are correlated with photoelectron spectra. This can be achieved by resolving the photoelectron reduced density matrix into contributions from an ionic state. It is expected that such analyses will lead to a better understanding of experimental results and precise prediction of high-field and ultrafast phenomena. Another

direction of future prospects is an application to systems considering nuclear dynamics. While we have presented the application of tSURFF to the TD-ORMAS method in this study, it is straightforward to extend it to other multielectron *ab initio* methods using time-dependent orbitals such as TD-MCSCF methods including nuclear dynamics. Such applications would enable us to compute photoelectron spectra from even more complicated systems and processes.

Contents

Chapter 1

Introduction

Laser technologies to make laser pulses shorter and stronger have been drastically advanced in the past couple of decades. One of the biggest developments in laser physics is chirped pulse amplification [1], which stretches a laser pulse and amplifies its intensity and squeezes it again. This technique enables us to generate high-intensity femtosecond (10^{-15} sec) laser pulses and leads to growth of the strong-field physics that studies nonperturbative and nonlinear optics: Perturbation treatment of laser-fields breaks down since the field intensity is too strong. Today, further shortening a duration of a laser pulse has been achieved, and it reaches a few tens of attoseconds (10^{-18} sec) in the state-of-the-art technology. Since the attosecond timescale corresponds to that of electronic dynamics in atoms and molecules, it became possible to observe ultrafast electronic dynamics by using attosecond laser pulses as ultrashort camera shutters. The appearance of the attosecond laser pulses has arisen a new research area "attosecond physics", where observation and even control of the ultrafast electronic dynamics are studied. It is expected that the knowledge and technologies in this field are applied to, for instance, developments of new optical devices and control of chemical reactions, where electronic dynamics plays the role of elementary processes.

Photoelectron spectroscopy is the most widely used to experimentally understand optical responses of matters exposed to laser pulses. It is well-known that photoelectron spectra can reveal electronic structures of matters in static states, but also photoelectron spectra are observed and analyzed to study strong-field phenomena and identify electronic dynamics on an attosecond time scale. In parallel with this, it is required that theoretical approaches to obtain accurate photoelectron spectra which can predict and explain experimental results. With this background, we develop an *ab initio* method to simulate photoelectron spectra from atoms and molecules exposed to strong and ultrashort laser pulses in this work.

In the rest of this chapter, we give an overview of strong-field physics and attosecond science, and *ab initio* simulation methods to describe multielectron dynamics subject to laser pulses in Sec. 1.1 and 1.2, respectively. In Sec. 1.3, we describe the difficulty in theoretically computing photoelectron spectra. In Sec. 1.4, the objective of this work is stated. We use atomic units unless otherwise mentioned throughout this thesis (see Appendix A for the details).

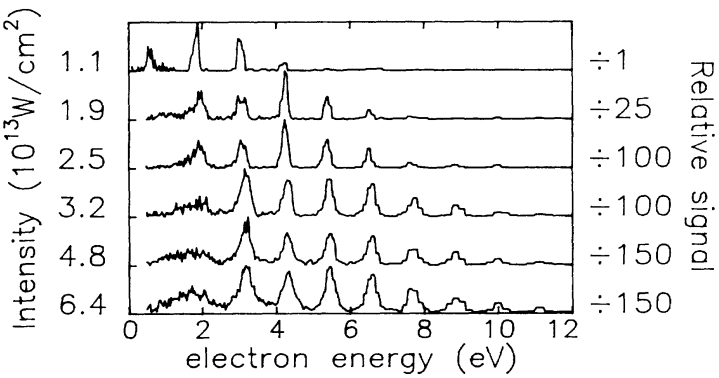

Figure 1.1: Experimentally obserbed photoelectron energy spectra of ATI in a xenon atom subject to 1064-nm light. This figure is cited from Ref. [2].

1.1 Strong field physics and Attosecond science

When we shine a strong laser pulse to atoms and molecules, various nonlinear optical phenomena that cannot be described by the perturbation theory, called strong-field phenomena, are observed. While laser technologies have been rapidly developed, the mechanism and applications of strong-field phenomena have been actively studied. In this section, we describe typical strong-field phenomena, above threshold ionization and high harmonic generation, and an important application of attosecond laser pulses, an observation of the charge migration.

1.1.1 Above threshold ionization

Under an intense laser with its intensity larger than about $10^{13}\,\mathrm{W/cm^2}$, we can observe a strong-field phenomenon, where atoms and molecules are ionized by absorbing more than the minimally required number of photons. This is known as above threshold ionization (ATI). Figure 1.1 presents an experimentally observed photoelectron energy spectra of ATI in a xenon atom [2], where we clearly see multiple ATI peaks corresponding to absorbed photon numbers. As shown in Fig 1.1, the ATI peaks do not obey the perturbation theory, which indicates that the peak values monotonically decrease as the number of photons increases. Another interesting feature in Fig. 1.1 is that the lowest order peak disappears as the field intensity increases. This can be understood through the pondermotive energy, which is the temporal averaged kinetic energy of a charged particle in an electromagnetic field, given by,

$$U_p = \frac{q^2 E_0^2}{4m\omega_0}, \tag{1.1}$$

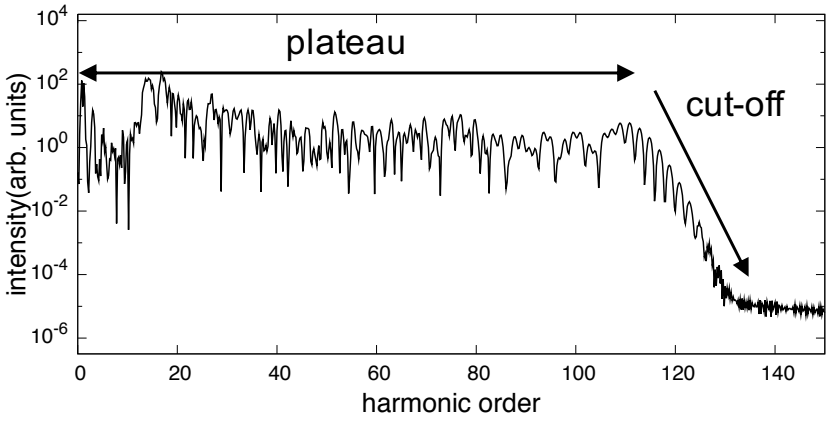

Figure 1.2: High harmonic spectrum from a helium atom exposed to a laser pulse with 800 nm wavelength and 8.0×10^{14} W/m^2 peak intensity, calculated by the MCTDHF method.

where q is a charge, m is mass of a particle, E_0 is an electric field amplitude, and ω_0 is its angular frequency. For electrons, it is given by,

$$U_p[\mathrm{eV}] = 9.337 \times 10^{-14} I_0[\mathrm{W/cm^2}]\lambda_0^2[\mu\mathrm{m}], \tag{1.2}$$

with I_0 and λ_0 being a field intensity and wavelength, respectively. A free electron in a laser field obtains the pondermotive energy U_p, and thus the ionization potential energy I_p effectively increases to $I_p + U_p$. Since the pondermotive energy U_p increases as a laser intensity increase as shown in Eq. (1.1), the lowest order ATI peak disappears in higher intensities.

1.1.2 High harmonic generation

Illuminating atoms and molecules by a laser pulse stronger than $\sim 10^{14}\,\mathrm{W/cm^2}$, they emit high order harmonics, which have integer multiples of the incident photon energy. This process is high harmonic generation (HHG). Figure 1.2 shows a typical high harmonic spectrum. We see a distinctive structure, which has a plateau region where the peak intensities do not decrease with the harmonic order increasing, and a sudden cut-off at which the peak intensities sharply decrease. The perturbation theory cannot explain this structure, and thus HHG is a nonperturbative process. However, this can be understood by a simple semiclassical model, called the three step model [3, 4]. This model describes HHG as follows.

1. *Tunneling ionization*: Nuclear Coulomb potentials are drastically distorted by laser fields and electrons ionize passing through the potential barrier by the tunneling effect.

2. *Acceleration*: After tunneling ionization, electrons are accelerated by oscillating laser fields.

3. *Recombination*: A part of electrons comes back to the parent ion position and collides with it, emitting a photon taking the kinetic energy of the electron and the ionization potential I_p.

The cut-off energy E_c is given as the sum of the maximum kinetic energy and the ionization potential within this model. By solving Newton's equation of motion for an electron under a periodically oscillating electric field [3], the maximum kinetic energy is obtained as $3.17U_p$, and thus the cut-off energy is given by

$$E_c \approx I_p + 3.17U_p. \tag{1.3}$$

It is known that this simple equation can successfully explain experimental results very well [5].

One of the important applications of HHG is the generation of light pulses with attosecond time width. As we mentioned above, high harmonic spectra have a plateau region extending to the cut-off energy. The cut-off order typically reaches a few tens order, thus by using HHG we can convert a laser pulse into a light with a frequency several tens times that of the incident laser. This broad spectrum makes it possible to generate attosecond light pulses.

1.1.3 Observation of the charge migration

The generation of attosecond light pulses using high order harmonics has enabled direct observation of electron dynamics in atoms and molecules, which was difficult with femtosecond laser pulses. Electrons bound to atoms and molecules move on an attosecond scale. To measure them, a faster shutter than that the motion is required.

Recently, attosecond light pulses were applied to observe the charge migration. Illuminating a molecule by a short light pulse with a photon energy sufficiently higher than the ionization potential, plural coherent ionized states are generated at the same time. This superposition of ionized states, which have different eigenenergies, has positively and negatively charged parts, and it has been theoretically predicted that these charges migrate in molecules on an attosecond time scale [6–8].

To cause this phenomenon, wave functions of ionized systems including photoelectrons must be overlapped. For example, it is difficult to observe the charge migration by using a femtosecond laser pulse. This is because in the case that a laser pulse with a longer pulse duration than the electronic time scale, electrons are emitted at various timings and thus the coherence of the system is lost. Hence, Calegari and *et al.* have employed an attosecond pulse with a time width lower than 300 as to induce charge migration in an amino acid molecule, and succeeded the first observation of this phenomenon in the world [9] (Fig. 1.3).

Since such photoionization and associated electronic dynamics are an elementary process that occurs when bio-molecules are exposed to radiation, it is expected that understanding of charge migration will lead to the elucidation of the effects of radiation on organisms from the molecular level. On the other hand, from the viewpoint of chemistry,

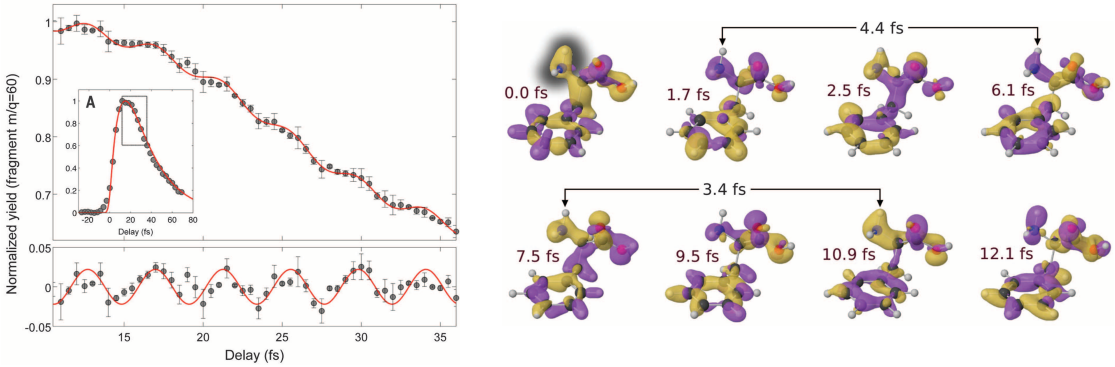

Figure 1.3: (Left) Yield of doubly charged ions as a function of pump-probe delay. (Right) Snapshots of relative variation of the charge density, calculated by the density functional theory. Vibration periods observed in these figures show a good agreement. These figures are cited from Ref. [9]

localized and oscillating charge in charge migration may influence molecular reactivity. Thus, is it expected that understanding and controlling of light-induced charge migration give a possibility of the control of chemical reaction.

1.2 *Ab-initio* simulations for laser-induced electronic dynamics

Electronic dynamics studied in the strong-field physics and attosecond science is complicated phenomena, which includes non-perturbative and nonlinear effects, and involves multiple states or paths excited by ultrashort pulses. Strong laser fields massively ionize and excite atoms and molecules. Furthermore, not only one electron, but also multiple electrons can be ionized and excited. This leads to a breakdown of the single-active electron (SAE) model [10], which considers only a valence electron, and requires to consider multielectron systems. Ultrashort pulses have broad energy spectra width due to the uncertainty principle of the Fourier transform. This yields many energy eigenstates through photoexcitation or photoionization, and many channels or paths are involved in the dynamics. It is often difficult to apply models considering only a few specific states for the dynamics. *Ab initio* simulations have an important role to understand and predict these phenomena. Although solving the time-dependent Schrödinger equation (TDSE) gives an exact description of the dynamics in the non-relativistic regime, it almost impossible to directly solve TDSE for many-body systems due to the exponential growth of the computational cost or the curse of dimensionality. To overcome this problem and enable *ab initio* simulations, the time-dependent multiconfiguration self-consistent field methods [11–15], which we describe below, have been developed.

1.2.1 Target systems

Before moving on to further detail of theoretical approaches, we first define systems to be handled in this work. We consider an atom or a molecule under a laser field. The total number of electron is N, which are composed of $N_\uparrow$ up-spin and $N_\downarrow$ down-spin electrons ($N = N_\uparrow + N_\downarrow$). The atomic nuclei are spatially fixed and treated as point charges.

When the wavelength of the laser field is much larger than the system size, spatial variation of the electromagnetic field can be negligible. This approximation is called the dipole approximation or long wavelength approximation. Laser pulses assumed in this work are mainly in the range of extreme ultraviolet (EUV) to near-infrared (NIR), whose wavelengths are much larger than atoms and small molecules. Thus we consider the laser-matter interaction within the dipole approximation [16]. Under the dipole approximation, the electric field is a spatially constant and the magnetic field is zero.

We use $\boldsymbol{r}$ as a spatial coordinate, σ as a spin coordinate and $\boldsymbol{x}$ as a set of them. The system Hamiltonian $H(t)$ and the time-dependent Schrödinger equation giving the dynamics of this system within the above condition is given by,

$$H(t) = \sum_{i=1}^{N} h_1(\boldsymbol{r}_i, \nabla_i, t) + \frac{1}{2}\sum_{i=1}^{N}\sum_{j=1}^{N} h_2(\boldsymbol{r}_i, \boldsymbol{r}_j), \tag{1.4}$$

$$i\frac{\partial}{\partial t}\Psi(x_1, x_2, \cdots, x_N, t) = H(t)\Psi(x_1, x_2, \cdots, x_N, t), \tag{1.5}$$

where $h_1(\boldsymbol{r}_i, \nabla_i, t)$ and $h_2(\boldsymbol{r}_i, \boldsymbol{r}_j)$ denote one-body and two-body terms, respectively,

$$h_1(\boldsymbol{r}_i, \nabla_i, t) = -\frac{\nabla_i^2}{2} + V_{\mathrm{N}}(\boldsymbol{r}_i) + V_{\mathrm{L}}(\boldsymbol{r}_i, \nabla_i, t), \tag{1.6}$$

$$h_2(\boldsymbol{r}_i, \boldsymbol{r}_j) = \frac{1}{|\boldsymbol{r}_i - \boldsymbol{r}_j|}. \tag{1.7}$$

The one body term $h_1(\boldsymbol{r}_i, \nabla_i, t)$ includes electronic kinetic energy, a Coulomb potential from atomic nuclei $V_{\mathrm{N}}(\boldsymbol{r}_i)$ and a potential of a laser field $V_{\mathrm{L}}(\boldsymbol{r}_i, \nabla_i, t)$, and the two body term is an interelectronic Coulomb potential.

The nuclear Coulomb potential is given by,

$$V_{\mathrm{N}}(\boldsymbol{r}_i) = \begin{cases} -\dfrac{Z}{|\boldsymbol{r}_i|} & \text{for atoms} \\ -\displaystyle\sum_{A}^{\text{nuclei}} \dfrac{Z_A}{|\boldsymbol{r}_i - \boldsymbol{R}_A|} & \text{for molecules} \end{cases}, \tag{1.8}$$

where $Z_A(Z)$ and $\boldsymbol{R}_A$ are the charge and position of a nucleus A, respectively. In the atom case, the nucleus is located at the origin.

The form of $V_{\mathrm{L}}(\boldsymbol{r}_i, \nabla_i, t)$ depends on a gauge. There are two famous choice: one is the

length gauge, and the other is the velocity gauge.

$$V_{\mathrm{L}}(\boldsymbol{r_i}, \nabla, t) = \begin{cases} \boldsymbol{E}(t) \cdot \boldsymbol{r_i} & \text{length gauge} \\ -i\boldsymbol{A}(t) \cdot \nabla_i & \text{velocity gauge} \end{cases} \tag{1.9}$$

Physical observables are independent of the choice of the gauges.

1.2.2 Multiconfiguration self-consistent field method

As shown in Eq.(1.5), N-particle TDSE in 3D space is a $3N(+1)$ dimensional partial derivative equation. If we try to numerically solve this equation by discretizing each dimension by L points, the computational complexity scales as $\mathcal{O}(L^{3N})$. This exponential growth depending on the number of particles causes difficulty in solving many-body TDSE. Two-electron systems are currently the largest system that can be directly solved.

The multiconfiguration self-consistent field (MCSCF) method has been developed to solve larger systems with low computational costs. The main idea is to express a multi-electron wave function as a superposition of multiple Slater determinants (configurations) composed of orthonormal single particle functions $\{\chi_p(\boldsymbol{x}, t)\}$, which are named spin orbitals.

$$\Psi(\boldsymbol{x}_1, \boldsymbol{x}_2, \cdots, \boldsymbol{x}_N, t) = \sum_I C_I(t) \begin{vmatrix} \chi_{I_1}(\boldsymbol{x}_1, t) & \chi_{I_2}(\boldsymbol{x}_1, t) & \cdots & \chi_{I_N}(\boldsymbol{x}_1, t) \\ \chi_{I_1}(\boldsymbol{x}_2, t) & \chi_{I_2}(\boldsymbol{x}_2, t) & \cdots & \chi_{I_N}(\boldsymbol{x}_2, t) \\ \vdots & \vdots & \ddots & \vdots \\ \chi_{I_1}(\boldsymbol{x}_N, t) & \chi_{I_2}(\boldsymbol{x}_N, t) & \cdots & \chi_{I_N}(\boldsymbol{x}_N, t) \end{vmatrix} \tag{1.10}$$

This decomposition of the wave function above is called the multiconfiguration expansion or configuration interaction (CI) expansion, and the space spanned by linear combination of the Slater determinants is referred to as configuration interaction (CI) space. If the spin orbitals constitute a complete basis set, which spans the single-particle Hilbert space, and all the possible Slater determinants are considered for the multiconfiguration expansion, Eq. (1.10) can always describe the exact wave function. However, the number of spin orbitals in a complete basis set is, in principle, infinity, and even in numerically discretized cases, it is numerous. Thus, for numerical computations, the CI space is restricted by using a part of the spin orbitals and a part of the configurations. Spin orbitals considered in CI expansion is referred to as occupied spin orbitals, and the rest is virtual spin orbitals or unoccupied spin orbitals. Figure 1.4 schematically shows a concept of spin orbitals and the MCSCF expansion. Expansion coefficients $\{C_I\}$, called CI coefficients, and orbitals are optimized within the restricted CI space based on the time-dependent variational principle (TDVP) [17–19]. The more spin orbitals and configurations are used for CI expansion, the better accuracy is achieved.

Time dependence of spin orbitals plays an important role for real-time simulations with laser pulses. Since laser fields can drastically change electronic states, if spin orbitals are fixed in time, numerous orbitals are required to accurately describe the dynamics. On the

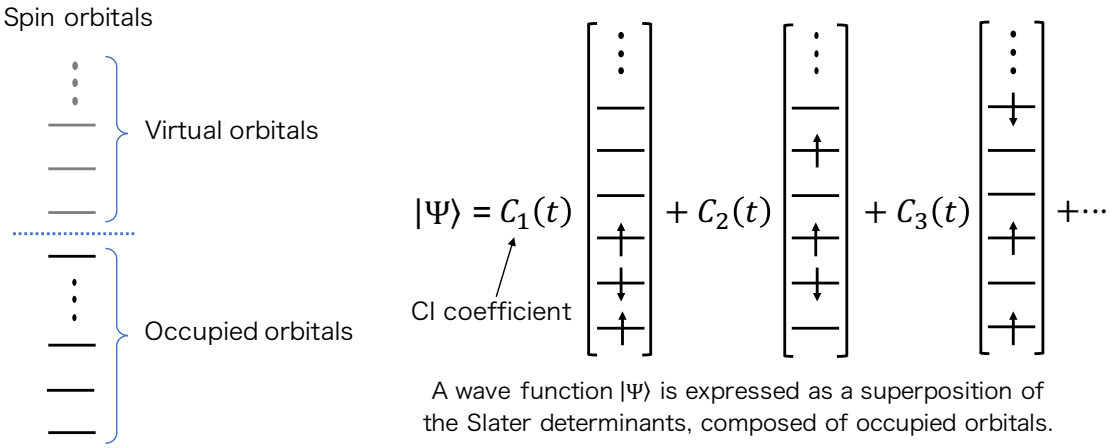

Figure 1.4: A schematic illustration of spin orbitals and a wave function expanded by the MCSCF method.

other hand, time-dependent orbitals flexibly vary, and a small number of them is sufficient to describe it.

Some representative methods in the MCSCF framework are reviewed below. For simplicity we hereinafter only treat spin-restricted cases, where up-spin orbitals and down-spin orbitals have same spatial dependency,

$$\chi_p(\boldsymbol{x}) = \begin{cases} \phi_p(\boldsymbol{r}) s_\uparrow(\sigma) \\ \phi_p(\boldsymbol{r}) s_\downarrow(\sigma) \end{cases} . \tag{1.11}$$

We call spacial function $\{\phi_p(\boldsymbol{r})\}$ spatial orbitals, or more simply orbitals. $s_\uparrow(\sigma)$ and $s_\downarrow(\sigma)$ are up-spin and down-spin eigenfunction, respectively.

$$s_\uparrow(\sigma) = \begin{cases} 1 & (\sigma = \uparrow) \\ 0 & (\sigma = \downarrow) \end{cases}, \quad s_\downarrow(\sigma) = \begin{cases} 0 & (\sigma = \uparrow) \\ 1 & (\sigma = \downarrow) \end{cases} \tag{1.12}$$

Time-dependent Hartree-Fock method

The time-dependent Hartree-Fock (TDHF) method is the simplest MCSCF method, which uses the same number of spin orbitals as the number of electrons. A wave function is expressed by a single Slater determinant.

Though TDHF requires less computational costs than other methods reviewed next and gives a good description of the ground-state, this method has difficulty in describing excitation and ionization processes in multielectron systems under laser fields. This problem is observed, for example, in a He atom as the simplest multielectron system. Let us

consider a wave function of one up-spin and one down spin electrons, which is given by,

$$\Psi(\boldsymbol{x}_1, \boldsymbol{x}_2) = \frac{1}{\sqrt{2}}\phi_1(\boldsymbol{r}_1)\phi_1(\boldsymbol{r}_2)(s_\uparrow(\sigma_1)s_\downarrow(\sigma_2) - s_\downarrow(\sigma_1)s_\uparrow(\sigma_2)). \tag{1.13}$$

In this wave function, electron 1 and electron 2 occupies the same orbital ϕ_1. Thus it is difficult to describe a situation where an electron is ionized and the other electron is bound by the nuclear potential. It is reported than the unrestricted Hartree-Fock method [20–22], which allows different spatial orbitals for up-spin and down-spin electrons, can improve this problem, but not reach sufficient accuracy [23].

Multiconfiguration time-dependent Hartree-Fock

To realize more accurate simulations than the TDHF method, the multiconfiguration time-dependent Hartree-Fock (MCTDHF) method has been proposed [11–13], which expands a multielectron wave function with all the Slater determinants constructed from a given number of spatial orbitals $\{\phi_p(t)\}$. This construction of multiconfiguration wave function using all the possible Slater determinants is called the full-CI expansion. Although this method can systematically improve accuracy by increasing the number of orbitals, and, in principle, reach the numerical convergence describing the exact wave function, its applications are limited to small systems, which include less than about 10 electrons, due to heavy computational costs of the full-CI method. In the full-CI expansion, the number of the Slater determinants is given by ${}_{N_{\rm orb}}C_{N_\uparrow} \times {}_{N_{\rm orb}}C_{N_\downarrow}$, where $N_{\rm orb}$ is the given number of orbitals and $N_\uparrow$ ($N_\downarrow$) is the number of up-spin (down-spin) electrons. Thus, this factorial increase of the full-CI dimension restricts the application of the MCTDHF method to larger systems.

Time-dependent complete-active-space self-consistent field method

To overcome the problem of the MCTDHF method and apply the TD-MCSCF method to the larger systems, it is required to decrease the number of the Slater determinants, while keeping the accuracy. The configurations considered in The MCTDHF method can include states where deeply-bound inner core electrons are excited or ionized. However, for atoms or molecules subject to a strong laser pulse with a long wavelength whose photon energy is considerably smaller than the ionization or excitation energy, it must be reasonable to assume that only valence electrons are ionized or excited and inner core excitation and ionization are negligible. Based on this assumption, the time-dependent complete-active-space self-consistent field (TD-CASSCF) method introduces an orbital classification, where spatial orbitals classified into doubly occupied and time-independent frozen core, doubly occupied and time-dependent dynamical core, and fully correlated active orbitals (Fig. 1.5). While dynamical core orbitals keeping the closed-shell model describe electric polarization depending on incident laser pulses and the Coulomb forces from other electrons, active orbitals can correctly describe ionization processes of valence

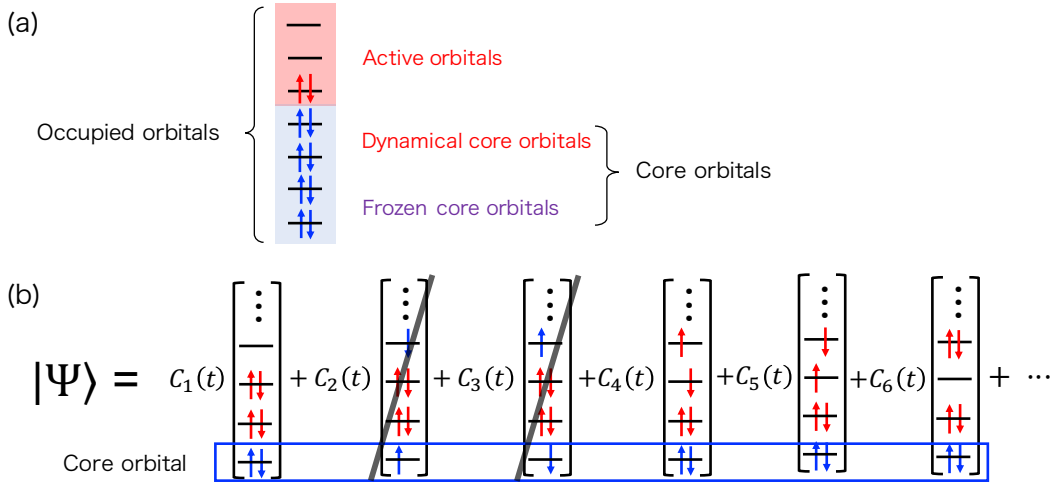

Figure 1.5: (a) Orbital classification in the TD-CASSCF method, where occupied orbitals are classified into doubly occupied and time-independent frozen core, doubly occupied and time-dependent dynamical core, and fully correlated active orbitals. (b) A schematic illustration of a wave function described with the TD-CASSCF method, where a core orbital is forced to be doubly occupied all the time, and thus the second and third configurations in this figure are not included in the CI expansion.

electrons. The TD-CASSCF method significantly reduces the number of configurations and the computational cost without degrading accuracy, and enables accurate simulations of multielectron dynamics such as high-harmonic generation from a neon atom and an argon atom [24, 25]. In addition to the advantage of the computational cost reduction, by comparing simulation results computed with different numbers of orbitals or different classifications of core and active orbitals, the TD-CASSCF method also enables analyses to reveal which orbital takes a dominant role in strong-field phenomena [26].

Time-dependent occupation restricted multiple-active-space method

Although the computational costs of the TD-CASSCF method are significantly reduced compared to the MCTDHF method, it still has factorial scaling. In order to solve this problem, the time-dependent occupation restricted multiple-active-space (TD-ORMAS) method further subdivide active orbitals into an arbitrary number of subgroups and poses the occupation restriction by specifying the minimum and maximum numbers of electrons distributed in each subgroup (theoretical details are given in Ch. 2) [15]. This method offers highly flexible constructions of the CI space including the MCTDHF and TD-CASSCF methods, and requires computational costs with polynomial scaling against the number of electrons depending on the choice of the subdivision and the occupation restriction. Because of the significant computational cost reduction, the TD-ORMAS method enables

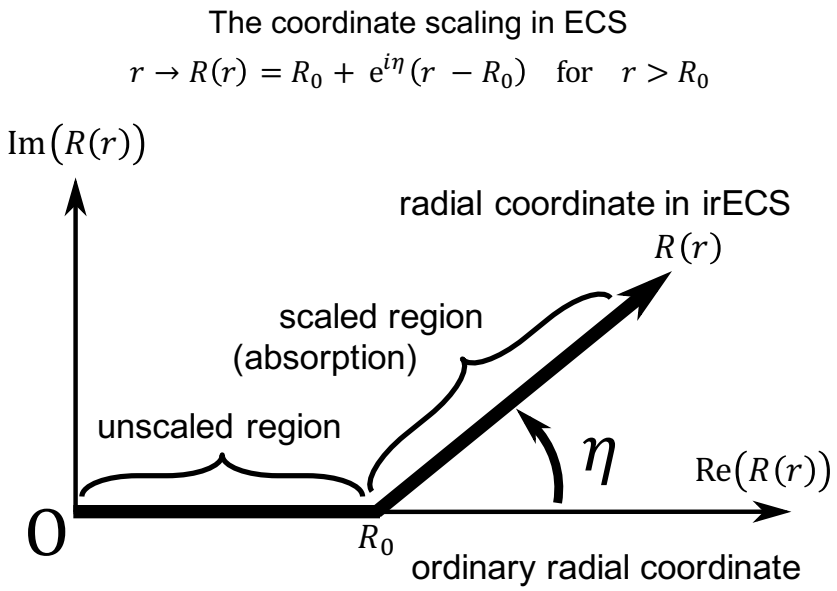

Figure 1.6: Schematic illustration of radial exterior complex scaling contour $R(r)$ with scaling radius R_0 and scaling angle η. In the scaled region ($r > R_0$), outgoing waves exponentially decay, and thus ECS performs as an absorbing boundary.

converged simulations of correlated multielectron dynamics in systems containing several tens of electrons such as a krypton atom [27].

1.2.3 Absorbing boundary condition

One of the key issues in real-time *ab initio* simulations of laser-induced dynamics is a huge computational cost arising from a large simulation box to describe photoionization. If a simulation box is not sufficiently large, photoelectron wave packets can reach the end of the box and be unphysically reflected. An absorbing boundary, which absorbs the photoelectron wave packet when it reaches the end of the spatial grid and suppresses unphysical reflection, plays a significantly important role to achieve large scale simulations.

Commonly used absorbing boundaries are the mask function [28] method, which multiplies a mask function to wave functions, and the complex absorbing potential [29, 30], which adds a complex potential into the system Hamiltonian. Though these methods partially suppress the unphysical reflection, reflection of unabsorbed outgoing waves still occurs.

Exterior complex scaling (ECS) [31] is considered to be more sophisticated, which analytically continues the wave function into the complex plane without artificially modifying the system Hamiltonian or the wave function (see Ch. 3 for the details). Figure 1.6 shows a schematic illustration of the analytical continuation in ECS. Furthermore, the infinite-range exterior complex scaling (irECS) method introduced in Ref. [32] signifi-

cantly improves the efficiency over standard ECS by using an exponentially damped basis, thus moving the reflecting boundary to infinity.

The application of ECS and irECS, originally formulated for single-electron problems, to strongly driven multielectron systems with the addition of the interelectronic Coulomb interaction so far has been limited. McCurdy *et al.* [31] introduced ECS to two-electron systems where the Coulomb interaction was approximated in the radial limit. Haxton *et al.* [33] used ECS in their MCTDHF implementation but mainly dealt with photoionization rather than strong-field phenomena. Telnov *et al.* [34] applied ECS to the time-dependent density functional theory to simulate high-harmonic generation from Ar. In the scaled region, however, they neglected the laser field and replaced the time-dependent Hartree and exchange-correlation potentials with their initial values. Majety *et al.* [35] have recently proposed the hybrid antisymmetrized coupled-channels method to calculate fully differential photoelectron spectra of multielectron systems subject to strong laser fields. Though irECS is used in the implementation, only an electronic coordinate is scaled in each channel as the method allows only single ionization. Zielinski *et al.* [36] have applied irECS to two-electron systems, where both the electronic coordinates are scaled. However, irECS has never been applied to TD-MCSCF methods.

1.3 Photoelectron spectra

As *ab initio* simulations have developed, we have enabled to simulate large systems which are considered as subjects of real experiments. Enabling a direct comparison between accurate *ab initio* simulations and experiments is one of the next steps for further development of technologies to observe and control the ultrafast electronic dynamics. Photoelectron energy spectra (PES) and their angular distribution, or angle-resolved photoelectron energy spectra (ARPES) are among important experimental probes for laser-matter interaction. Since PES have plenty of information on electronic states and photoemission dynamics, many time-resolved and angular-resolve analyses have been conducted [37–41].

One of the important techniques used in attosecond science is the attosecond streaking method [42–45], which first ionizes a target with an attosecond pulse, and modulates the photoelectron momentum with a delayed strong laser pulse. By Sweeping the delay time, we can obtain time-resolved information of photoelectron spectra. For instance, this method was used to analyze photoemission from a neon atom [46]. The time-resolved measurement with attosecond accuracy revealed that photoemission from the $2s$ orbital is delayed by 21 attoseconds compared to that from the $2p$ orbital.

On the other hand for *ab initio* numerical simulations, photoelectron spectra could be calculated, in principle, by projecting the departing photoelectron wave packet onto plane waves or Coulomb waves. This approach, however, requires retaining the complete wave function without being absorbed, leading to a huge simulation box and prohibitive computational cost. To circumvent this difficulty, Tao and Scrinzi have devised the time-dependent surface flux (tSURFF) method [47], which extracts PES by integrating the wave function flux through a surface. Thus it allows one to use an absorbing boundary,

bringing significant cost reduction.

The tSURFF method was first developed for single electron systems [47], and then applied to one-dimensional two-electron systems to obtain doubly differential photoelectron spectra [48]. Majety *et al.* have proposed the hybrid antisymmetrized coupled channels method [35], where only single ionization was allowed, and used the tSURFF method to calculate fully differential photoelectron spectra in multielectron systems. Zielinski *et al.* have applied the tSURFF method to three dimensional two-electron systems, and successfully calculated correlated photoelectron momentum spectra in double ionization [36]. Karamatskou *et al.* have applied the tSURFF method to the time-dependent configuration interaction singles (TDCIS) method [49] by neglecting all the multielectron meanfield potentials. Though The TDCIS method can describe multielectron systems, it allows only single ionization. Wopperer *et al.* have applied to the time-dependent density functional theory (TDDFT) with an assumption that photoelectron spectra can be directly obtained from the time-dependent Kohn-Sham orbitals [50]. However, the tSURFF has not been applied to general TD-MCSCF methods, which enables systematic improvement of accuracy, considering multielectron effects such as the electronic correlation and the multiple ionization.

1.4 Objective

Though photoelectron spectra are often observed in experiments to explore electronic dynamics and structures, it is difficult to theoretically compute accurate spectra including multielectron effects. The objective of this thesis is to develop a realtime *ab initio* simulation method to extract photoelectron spectra from multielectron atoms subject to intense laser fields. To accomplish this challenging task, we combine irECS as an efficient and accurate absorbing boundary and the tSURFF method with the TD-ORMAS method.

We have applied irECS to the TD-ORMAS method, by neglecting the Coulomb force from electrons residing in the scaled region, which are far apart. However, we rigorously include all the other interactions (e.g. external fields, the nuclear potential and the Coulomb force from electrons in the unscaled region). This implementation works well even when atoms undergo significant double ionization, and enables several times faster simulations than the mask function method while keeping high accuracy. In the application of the tSURFF method, based on a physically reasonable assumption that the nuclear potential and interelectronic Coulomb interaction are negligible for photoelectron dynamics in the region distant from the nuclei, we have derived the equations of motion for the momentum amplitudes of each orbital, and implemented the tSURFF method for atoms subject to linearly polarized laser pulses. As a result of this development, we have achieved highly accurate calculations of PES and angle-resolved PES with considerably reduced computational costs, and revealed that electronic correlation affects the angular distribution of photoelectron yields in above threshold ionization spectra of an Ar atom. Furthermore, we present an extension of this development to molecular systems implemented with the adaptive finite element method.

This thesis is organized as follows. Chapter 2 gives a review of the theory of the TD-ORMAS method and its implementation for atoms. In Ch. 3, we reviews ECS for single-electron systems, and describe our numerical implementation of irECS and application of irECS to the TD-ORMAS method. The accuracy and efficiency of irECS in the application are also shown in this chapter. In Ch. 4, we describe the theoretical application and numerical implementation of the tSURFF method to the TD-ORMAS method, and show numerical applications. The extension to extract photoelectron spectra from molecules is described in Ch. 5. Chapter. 6 concludes this thesis and discuss future prospects.

Chapter 2

The Time-dependent occupation restricted multiple-active-space method

In this chapter, we review the theory of the time-dependent occupation restricted multiple-active-space (TD-ORMAS) method proposed in Ref. [15] and the derivation of equations of motion. After the review of the theory, we explain our implementation of the TD-ORMAS method for atoms subject to a linearly polarized laser pulse, detailed in Ref. [24].

2.1 The ORMAS model

In this section, we define the occupation restricted multiple-active-space (ORMAS) model. The systems considered in this section are an atom and a molecule under a laser field, which are detailed in Subsec. 1.2.1, including $N_\uparrow$ up-spin and $N_\downarrow$ down-spin electrons and $N(= N_\uparrow + N_\downarrow)$ electrons in total.

We assume that single electron Hilbert space is spanned by the complete set of N_b orthonormal spatial orbitals $\{\phi_\mu\}$. The Fermion creation and annihilation operator associated with spatial orbitals $\{\phi_\mu\}$ and a spin coordinate σ are defined as $\hat{a}^\dagger_{\mu\sigma}$ and $\hat{a}_{\mu\sigma}$. The orbital set is divided into n occupied orbitals and $N_b - n$ virtual orbitals. In the ORMAS model, as the MCSCF method, the wave function is constructed by occupied orbital sets.

The core orbital technique introduced in the TD-CASSCF method [14], where orbitals classified into doubly occupied and time-independent frozen core, doubly occupied and time-dependent dynamical core, and fully correlated active orbitals, is also applicable to the ORMAS model. We define core orbitals (n_{fc} frozen and n_{dc} dynamical cores) as the first $n_c(= n_{\mathrm{fc}} + n_{\mathrm{dc}})$ occupied orbitals, and thus the rest of $n_a(= n - n_c)$ orbitals are classified into active orbitals. Since core orbitals are always doubly occupied, $N_c(= 2n_c)$ electrons are classified into core electrons, and $N_a(= N - N_c)$ electrons are active electrons. We refer to the core orbital and active orbital subset as $\mathcal{C}$ and $\mathcal{A}$.

Based on the definition above, a MCSCF wave function, not restricted to the ORMAS

model, respect to a given CI space P can be written as,

$$|\Psi\rangle = C_I \hat{\Phi}_C \sum_I^P |I\rangle\,, \tag{2.1}$$

$$\hat{\Phi}_C = \prod_{\sigma=\uparrow,\downarrow} \prod_{i\in\mathcal{C}} \hat{a}^\dagger_{i\sigma}, \tag{2.2}$$

$$|I\rangle = \prod_{\sigma=\uparrow,\downarrow} \prod_{t\in\mathcal{A}} (\hat{a}^\dagger_{t\sigma})^{I_{t\sigma}} |\rangle\,, \tag{2.3}$$

where $|\rangle$ denotes the vacuum state, and $I_{t\sigma}$, which equals to 1 or 0, means whether a spin orbital $\phi(\boldsymbol{r})s_\sigma(\tau)$ is included in a configuration I or not. $\hat{\Phi}_C$ and $|I\rangle$ represent the core and active orbital parts.

The ORMAS model further subdivides the active orbital subset $\mathcal{A}$ into a given number G of subgroups. We consider a direct sum decomposition of $\mathcal{A}$,

$$\mathcal{A} = \mathcal{A}_1 \oplus \mathcal{A}_2 \oplus \cdots \oplus \mathcal{A}_G, \tag{2.4}$$

$$\begin{aligned}
\mathcal{A}_1 &= \{\phi_1^{(1)}, \phi_2^{(1)}, \cdots, \phi_{n_1}^{(1)}\}, \\
\mathcal{A}_2 &= \{\phi_1^{(2)}, \phi_2^{(2)}, \cdots, \phi_{n_2}^{(2)}\}, \\
&\cdots \\
\mathcal{A}_G &= \{\phi_1^{(G)}, \phi_2^{(G)}, \cdots, \phi_{n_G}^{(G)}\},
\end{aligned} \tag{2.5}$$

$$n_a = \sum_g^G n_g. \tag{2.6}$$

n_g orbitals belonging to $\mathcal{A}$ are assigned to $\mathcal{A}_g$. The occupation restriction is achieved by imposing a lower limit and an upper limit to the number of electrons in each group,

$$\begin{aligned}
N_1^{\min} &\le N_1 \le N_1^{\max}, \\
N_2^{\min} &\le N_2 \le N_2^{\max}, \\
&\cdots \\
N_G^{\min} &\le N_G \le N_G^{\max},
\end{aligned} \tag{2.7}$$

$$N_a = \sum_g^G N_g. \tag{2.8}$$

N_g denote the number of electrons distributed in an orbital subgroup $\mathcal{A}_g$. All the possible configurations within those orbital subgrouping and occupation restriction construct the ORMAS-CI space P_{ORMAS}. It should be noticed that this construction of the CI space includes the MCTDHF method and the TD-CASSCF method, which are the case of $G = 1$.

2.2 Derivation of the equations of motion

In this section, we derive the equations of motion in the TD-ORMAS method from the time-dependent variational principle (TDVP) [19]. The system Hamiltonian is given in Eqs.(1.4)-(1.9). Here we show it again in the second quantization form,

$$\hat{H} = \sum h_{1\nu}^{\mu} \hat{E}_{\nu}^{\mu} + \frac{1}{2} \sum_{\mu\nu\lambda\gamma} h_{2\nu\gamma}^{\mu\lambda} \hat{E}_{\nu\gamma}^{\mu\lambda}, \tag{2.9}$$

where $h_{1\nu}^{\mu}$ and $h_{2\nu\gamma}^{\mu\lambda}$ are the matrix elements of one-electron and two-electron terms, respectively,

$$h_{1\nu}^{\mu} = \int d\boldsymbol{r} \phi_{\mu}^{*}(\boldsymbol{r}) h_1(\boldsymbol{r}, \nabla, t) \phi_{\nu}(\boldsymbol{r}) \tag{2.10}$$

$$h_{2\nu\gamma}^{\mu\lambda} = \int d\boldsymbol{r}_1 d\boldsymbol{r}_2 \phi_{\mu}^{*}(\boldsymbol{r}_1) \phi_{\lambda}^{*}(\boldsymbol{r}_2) h_2(\boldsymbol{r}_1, \boldsymbol{r}_2) \phi_{\gamma}(\boldsymbol{r}_2) \phi_{\nu}(\boldsymbol{r}_1). \tag{2.11}$$

The operator $\hat{E}_{\nu}^{\mu}$ and $\hat{E}_{\nu\gamma}^{\mu\lambda}$ represent,

$$\hat{E}_{\nu}^{\mu} = \sum_{\sigma=\uparrow,\downarrow} \hat{a}_{\mu\sigma}^{\dagger} \hat{a}_{\nu\sigma}, \tag{2.12}$$

$$\hat{E}_{\nu\gamma}^{\mu\lambda} = \sum_{\sigma,\tau=\uparrow,\downarrow} \hat{a}_{\mu\sigma}^{\dagger} a_{\lambda\tau}^{\dagger} \hat{a}_{\gamma\tau} \hat{a}_{\nu\sigma}. \tag{2.13}$$

The time-dependent variational principle requires the action integral S,

$$S[\Psi] = \int_{t_0}^{t_1} dt \, \langle \Psi | \hat{H} - i \frac{\partial}{\partial t} | \Psi \rangle \,, \tag{2.14}$$

to be stationary respect to variation of a wave function. The variation of the action integral δS from variation of a wave function is given by,

$$\begin{aligned} \delta S[\Psi] &= S[\Psi + \delta\Psi] - S[\Psi] \\ &= \int_{t_0}^{t_1} dt \left\{ \langle \delta\Psi | \hat{H} - i \frac{\partial}{\partial t} | \Psi \rangle + \langle \Psi | \hat{H} - i \frac{\partial}{\partial t} | \delta\Psi \rangle \right\} \\ &= \int_{t_0}^{t_1} dt \left\{ \langle \delta\Psi | \hat{H} - i \frac{\partial}{\partial t} | \Psi \rangle + \left(\langle \Psi | \, \hat{H} + i \, \langle \dot{\Psi} | \right) | \delta\Psi \rangle \right\}. \end{aligned} \tag{2.15}$$

The transformation from the first to the second line uses the partial integral and a boundary condition $\delta\Psi(t_0) = \delta\Psi(t_1) = 0$.

The variation of the ORMAS wave function is arisen from variation of CI coefficients $C_I \to C_I + \delta C_I$ and orbitals $|\phi_\mu\rangle \to |\phi_\mu\rangle + |\delta\phi_\mu\rangle$. The variation of orbitals can be by orbitals as a complete basis set of the Hilbert space,

$$|\delta\phi_\mu\rangle = \sum_{\nu} \Delta_{\mu}^{\nu} \, |\phi_\nu\rangle \,, \tag{2.16}$$

$$\Delta_{\mu}^{\nu} = \langle \phi_\nu | \delta\phi_\mu \rangle \,. \tag{2.17}$$

We impose orbital orthonormality on the orbital variation since orbitals are assumed to keep orthonormal after time-propagation. This is achieved by making the matrix $\{\Delta_\mu^\nu\}$ anti-Hermitian, which is derived from the following condition.

$$\langle \phi_\nu + \delta\phi_\nu | \phi_\mu + \delta\phi_\mu \rangle = \delta_\mu^\nu \tag{2.18}$$

Time derivative of orbitals is also expanded, as well as the orbital variation,

$$|\dot{\phi}_\mu\rangle = \sum_\nu X_\mu^\nu |\phi_\nu\rangle , \tag{2.19}$$

$$X_\mu^\nu = \langle \phi_\nu | \dot{\phi}_\mu \rangle . \tag{2.20}$$

Again, in order to keep orbital orthonormality after time-propagation, we assume the matrix $\{X_\mu^\nu\}$ anti-Hermitian which comes from,

$$\frac{\partial}{\partial t} \langle \phi_\nu | \phi_\mu \rangle = 0. \tag{2.21}$$

This condition is, in another way, achieved by the Lagrange multipliers method, which adds,

$$\sum_{\nu\mu} L_\mu^\nu (\langle \phi_\nu | \phi_\mu \rangle - \delta_\mu^\nu), \tag{2.22}$$

with the Lagrange multipliers L_μ^ν to the action integral $S[\Psi]$ (Eq. (2.14)). Both the ways lead to the same equations of motion. The time derivative of a wave function $\dot{\Psi}$ and the variation allowed in the ORMAS wave function $|\delta\Psi\rangle$ are given by,

$$|\dot{\Psi}\rangle = \dot{C}_I \hat{\Phi}_c \sum_I^{P_{\mathrm{ORMAS}}} |I\rangle + \hat{X} |\Psi\rangle , \tag{2.23}$$

$$|\delta\Psi\rangle = \delta C_I \hat{\Phi}_c \sum_I^{P_{\mathrm{ORMAS}}} |I\rangle + \hat{\Delta} |\Psi\rangle . \tag{2.24}$$

$$\tag{2.25}$$

The operator $\hat{X}$ and $\hat{\Delta}$ are the second quantization expressions of the matrices $\{X_\mu^\nu\}$ and $\{\Delta_\mu^\nu\}$, respectively,

$$\hat{X} = \sum_{\nu\mu} X_\mu^\nu \hat{E}_\mu^\nu, \tag{2.26}$$

$$\hat{\Delta} = \sum_{\nu\mu} \Delta_\mu^\nu \hat{E}_\mu^\nu. \tag{2.27}$$

The stationary condition of Eq (2.15) leads to,

$$\frac{\delta S}{\delta C_I} = \frac{\delta S}{\delta C_I^*} = 0 \quad I \in P_{\mathrm{ORMAS}}, \tag{2.28}$$

$$\frac{\delta S}{\delta \Delta_\mu^\nu} = 0. \tag{2.29}$$

Here, We can independently treat C_I and C_I^* based on the Wirtinger derivatives, which enables us to consider derivatives with respect to δC_I and δC_I^* instead of $\mathrm{Re}(\delta C_I)$ and $\mathrm{Im}(\delta C_I)$. The condition $\delta S / \delta \Delta_\mu^{\nu *} = 0$ is automatically considered in Eq. (2.29) due to the anti-Hermiticity of the matrix $\{\Delta_\mu^\nu\}$.

By inserting Eq. (2.23) and Eq. (2.24) to Eq (2.15), we obtain a more concrete expression of the stationary condition,

$$i\dot{C}_I = \sum_J^{P_{\mathrm{ORMAS}}} (\langle I|\hat{\Phi}_C^\dagger \hat{H} \hat{\Phi}_C|J\rangle - i\,\langle I|\hat{\Phi}_C^\dagger \hat{X} \hat{\Phi}_C|J\rangle) C_J, \tag{2.30}$$

$$i\,\langle \Psi|\hat{E}_\mu^\nu \hat{\Pi} \hat{X} - \hat{X}\hat{\Pi}\hat{E}_\mu^\nu|\Psi\rangle = \langle \Psi|\hat{E}_\mu^\nu \hat{\Pi}\hat{H} - \hat{H}\hat{\Pi}\hat{E}_\mu^\nu|\Psi\rangle\,. \tag{2.31}$$

The operator $\hat{\Pi}$ denotes a projector $\hat{1} - \sum_I^{P_{\mathrm{ORMAS}}} \hat{\Phi}_c\,|I\rangle\,\langle I|\,\hat{\Phi}_c^\dagger$, which projects out a wave function into the orthogonal complement of the CI space P_{ORMAS}. Equation (2.30) is the equations of motion of CI coefficients, which is determined when the orbital time derivatives matrix $\{X_\mu^\nu\}$ are figured out. The matrix $\{X_\mu^\nu\}$ is determined as a solution of Eq. (2.31). Note that, Eq. (2.31) has a complicated form, but this essentially forms a system of linear equations of $\{X_\mu^\nu\}$.

For the following discussion, we introduce a notion of orbital indices for each orbital subspace. That is,

$$i, j, k, l \equiv \text{core orbitals}, \tag{2.32a}$$

$$t, u, v, w \equiv \text{active orbitals}, \tag{2.32b}$$

$$o, p, q, r, s, p', q' \equiv \text{occupied orbitals}, \tag{2.32c}$$

$$a, b, c \equiv \text{virtual orbitals}, \tag{2.32d}$$

$$\mu, \nu, \lambda, \gamma, \delta \equiv \text{general orbitals (all the subspaces)}. \tag{2.32e}$$

Then, we first classify an orbital pair ν, μ based on orbital subspaces and the result of $\hat{\Pi}\hat{E}_\mu^\nu\,|\Psi\rangle$, where $\{\hat{E}_\mu^\nu\}$ replaces an orbital ϕ_μ with ϕ_ν in a wave function. All the possible operators $\{\hat{E}_\mu^\nu\}$ are listed as,

$$\{\hat{E}_\mu^\nu\} = \{\hat{E}_j^i, \hat{E}_t^i, \hat{E}_i^t, \hat{E}_u^t, \hat{E}_a^p, \hat{E}_p^a, \hat{E}_b^a\}. \tag{2.33}$$

The first class is the orbital pairs of core-core and virtual-virtual, which result in $\hat{\Pi}\hat{E}_\mu^\nu\,|\Psi\rangle = 0$. For the core-core pair, $\hat{E}_j^i\,|\Psi\rangle$ equals $2\delta_j^i\,|\Psi\rangle$, and thus $\hat{\Pi}\hat{E}_j^i\,|\Psi\rangle = 0$. For the virtual-virtual pair, an ORMAS wave function does not include virtual orbitals, then $\hat{E}_b^a\,|\Psi\rangle = 0$. In this case, Eq. (2.31) reduces a trivial equation, where the matrix $\{X_\mu^\nu\}$ can

be an arbitrary anti-Hermitian matrix including the zero matrix.

The second class is the orbital pairs of core-active $\{i,t\}$, active-core $\{t,i\}$, virtual-occupied $\{a,p\}$ and occupied-virtual $\{p,a\}$, where Eq. (2.31) reduces a simpler equation and we can directly solve it. For the core-active and active-core pairs, $\hat{E}^i_t|\Psi\rangle = 0$, and then $\hat{\Pi}\hat{E}^i_t|\Psi\rangle = 0$ and $\hat{\Pi}\hat{E}^t_i|\Psi\rangle = \hat{E}^t_i|\Psi\rangle$. For the virtual-occupied and occupied-virtual pairs, $\hat{E}^a_p|\Psi\rangle = 0$, and then $\hat{\Pi}\hat{E}^a_p|\Psi\rangle = 0$, and $\hat{\Pi}\hat{E}^p_a|\Psi\rangle = \hat{E}^p_a|\Psi\rangle$. In this case, the projector $\hat{\Pi}$ can be replaced with the identity operator in Eq. (2.31), and this leads to,

$$i\langle\Psi|[\hat{E}^\nu_\mu,\hat{X}]|\Psi\rangle = \langle\Psi|[\hat{E}^\nu_\mu,\hat{H}]|\Psi\rangle\,. \tag{2.34}$$

Thus, we can write down Eq. (2.31) with respect to the matrix element X^μ_μ,

$$i\sum_\lambda(X^\nu_\lambda D^\lambda_\mu - D^\nu_\lambda X^\lambda_\mu) = \sum_\lambda(h_1{}^\nu_\lambda D^\lambda_\mu - D^\nu_\lambda h_1{}^\lambda_\mu) + \sum_{\lambda,\delta,\gamma}(h_2{}^{\nu\delta}_{\lambda\gamma}P^{\lambda\gamma}_{\mu\delta} - P^{\nu\delta}_{\lambda\gamma}h_2{}^{\lambda\gamma}_{\mu\delta}). \tag{2.35}$$

D^μ_ν and $P^{\mu\lambda}_{\nu\gamma}$ denote the one-body and two-body reduced density matrix (RDM) elements,

$$D^\mu_\nu = \langle\Psi|\hat{E}^\nu_\mu|\Psi\rangle\,, \tag{2.36}$$

$$P^{\mu\lambda}_{\nu\gamma} = \langle\Psi|\hat{E}^{\nu\gamma}_{\mu\lambda}|\Psi\rangle\,. \tag{2.37}$$

In Eq. (2.35), the dummy indices λ,δ,γ run over all the orbitals, but nonzero elements of RDMs are, in general, $D^i_j = 2\delta^i_j, D^t_u, P^{ij}_{kl} = 4\delta^i_l\delta^j_k - 2\delta^i_k\delta^j_l, P^{it}_{uj}, P^{it}_{ju}, P^{tu}_{vw}$. Thus, Eq. (2.35) can be decomposed into,

$$i\sum_u^{\text{active}} X^i_u(D^u_t - 2\delta^u_t) = \sum_u^{\text{active}} h_1{}^i_u(D^u_t - 2\delta^u_t) + \sum_{p,q,r}^{\text{occupied}}(h_2{}^{iq}_{pr}P^{pr}_{tq} - P^{iq}_{pr}h_2{}^{pr}_{tq}) \quad \text{for } \{\nu,\mu\} = \{i,t\}, \tag{2.38}$$

$$i\sum_u^{\text{active}}(D^t_u - 2\delta^t_u)X^u_i = \sum_u^{\text{active}}(D^t_u - 2\delta^t_u)h_1{}^u_i - \sum_{p,q,r}^{\text{occupied}}(h_2{}^{tq}_{pr}P^{pr}_{iq} - P^{tq}_{pr}h_2{}^{pr}_{iq}) \quad \text{for } \{\nu,\mu\} = \{t,i\}, \tag{2.39}$$

$$i2X^a_i = 2h_1{}^a_i + \sum_{q,r,s}^{\text{occupied}} h_2{}^{ar}_{qs}P^{qs}_{ir} \quad \text{for } \{\nu,\mu\} = \{a,i\}, \tag{2.40}$$

$$i2X^i_a = 2h_1{}^i_a + \sum_{q,r,s}^{\text{occupied}} P^{ir}_{qs}h_2{}^{qs}_{ar} \quad \text{for } \{\nu,\mu\} = \{i,a\}, \tag{2.41}$$

$$i\sum_u^{\text{active}} X^a_u D^u_t = \sum_u^{\text{active}} h_1{}^a_u D^u_t + \sum_{q,r,s}^{\text{occupied}} h_2{}^{ar}_{qs}P^{qs}_{tr} \quad \text{for } \{\nu,\mu\} = \{a,t\}, \tag{2.42}$$

$$i\sum_{u}^{\text{active}} D_u^t X_a^u = \sum_{u}^{\text{active}} D_u^t h_{1a}^{\ u} + \sum_{q,r,s}^{\text{occupied}} P_{qs}^{tr} h_{2ar}^{\ qs} \quad \text{for } \{\nu,\mu\} = \{t,a\}. \tag{2.43}$$

Equations (2.39), (2.41) and (2.43) are identical to Eqs. (2.38), (2.40)and (2.42) due to anti-Hermiticity of the matrix $\{X_\mu^\nu\}$. Although we have introduced frozen core orbitals as time-independent orbitals, this is justified only in the length gauge. As for the velocity gauge, gauge-transformation of frozen core orbitals is required to preserve gauge-invariance [24]. Then, a frozen core orbital at time t is given as

$$|\phi_i(t)\rangle = \begin{cases} |\phi_i(0)\rangle & \text{length gauge} \\ \exp(-i\boldsymbol{A}(t)\cdot\hat{\boldsymbol{r}})\,|\phi_i(0)\rangle & \text{velocity gauge} \end{cases}, \quad \phi_i \in \text{frozen core}.$$

Thus, when orbital ϕ_i is a frozen core orbital, the orbital time-derivative element X_μ^i is given by

$$X_\mu^i = -X_i^{\mu *} = \begin{cases} 0 & \text{length gauge} \\ -i\boldsymbol{E}(t)\cdot\langle\phi_\mu|\hat{\boldsymbol{r}}|\phi_i\rangle & \text{velocity gauge} \end{cases}, \quad \phi_i \in \text{frozen core}.$$

On the other hand, when orbital ϕ_i is a dynamical core orbital, Eq. (2.39) and Eq. (2.40) reads,

$$X_i^t = -X_i^{t*} = -ih_{1i}^{\ t} + i\sum_{u}^{\text{active}} ((D-2\boldsymbol{I})^{-1})_u^t \sum_{p,q,r}^{\text{occupied}} (h_{2pr}^{\ uq} P_{iq}^{pr} - P_{pr}^{uq} h_{2iq}^{\ pr}) \qquad \phi_i \in \text{dynamical core}, \tag{2.44}$$

$$X_i^a = -X_i^{a*} = -ih_{1i}^{\ a} - i\frac{1}{2}\sum_{q,r,s}^{\text{occupied}} h_{2qs}^{\ ar} P_{ir}^{qs} \quad \phi_i \in \text{dynamical core}, \tag{2.45}$$

where D and $\boldsymbol{I}$ denote the one-body reduce matrix and identity matrix. And Eq. (2.42) reads,

$$X_t^a = -X_a^{t*} = -ih_{1t}^{\ a} - i\sum_{u}^{\text{active}}\sum_{q,r,s}^{\text{occupied}} h_{2qs}^{\ ar} P_{ur}^{qs} (D^{-1})_t^u. \tag{2.46}$$

Note that Eqs. (2.44) and (2.45) can be expressed as single equation,

$$X_p^a = -X_a^{p*} = -ih_{1p}^{\ a} - i\sum_{o,q,r,s}^{\text{occupied}} h_{2qs}^{\ ar} P_{or}^{qs} (D^{-1})_p^o. \tag{2.47}$$

The third class is the orbital pairs of active-active $\{t,u\}$. This pair has two types, which are an intragroup and intergroup pair. For the intragroup pair t,u, where ϕ_t and ϕ_u belong to a same active orbital subgroup $\mathcal{A}_g$, $\hat{\Pi}\hat{E}_u^t\,|\Psi\rangle = 0$. Thus, as well as the first class, Eq. (2.31) reduces to a trivial equation, and the matrix X_μ^ν can be an arbitrary anti-Hermitian matrix. For the intergroup pair t,u, where ϕ_t and ϕ_u belong to different active

orbital subgroups, $\hat{\Pi}\hat{E}^t_u|\Psi\rangle$ includes components of both the P_{ORMAS} and the orthogonal complement of P_{ORMAS}. Thus we need to directly solve Eq. (2.31), which forms a system of linear equations within intergroup pairs $\{t,u\}$,

$$i{\sum_{v,w}}'(A_{tu,vw}-A_{vw,tu})X^v_w = b_{tu}, \tag{2.48}$$

where $\sum_{v,w}{}'$ denotes summation over all permutations of intergroup pairs and,

$$A_{tu,vw} = \langle\Psi|\hat{E}^t_u\hat{\Pi}\hat{E}^v_w|\Psi\rangle\,, \tag{2.49}$$
$$b_{tu} = \langle\Psi|\hat{E}^t_u\hat{\Pi}\hat{H}|\Psi\rangle - \langle\Psi|\hat{H}\hat{\Pi}\hat{E}^t_u|\Psi\rangle\,. \tag{2.50}$$

In this work, we numerically solve Eq. (2.48) by singular value decomposition. All the matrix elements X^ν_μ are determined up to here.

We finally derive the equations of motion of orbitals. Time derivatives of orbitals are expressed as,

$$|\dot{\phi_p}\rangle = \sum_\mu |\phi_\mu\rangle\, X^\mu_p \tag{2.51}$$
$$= \sum_a^{\text{virtual}} |\phi_a\rangle\, X^a_p + \sum_q^{\text{occupied}} |\phi_q\rangle\, X^q_p. \tag{2.52}$$

Inserting Eq. (2.47) into the first term of above the equation, it is possible to remove virtual orbitals,

$$\sum_a^{\text{virtual}} |\phi_a\rangle\, X^a_p = -i \sum_a^{\text{virtual}} |\phi_a\rangle\langle\phi_a| \left[\hat{h}_1|\phi_p\rangle + \sum_{o,q,r,s}^{\text{occupied}} \hat{W}^r_s|\phi_q\rangle\, P^{qs}_{or}(D^{-1})^o_p\right] \tag{2.53}$$
$$= -i\hat{Q}\left[\hat{h}_1|\phi_p\rangle + \sum_{o,q,r,s}^{\text{occupied}} \hat{W}^r_s|\phi_q\rangle\, P^{qs}_{or}(D^{-1})^o_p\right], \tag{2.54}$$

where we introduce a projection operator $\hat{Q}$ by using completeness of orbitals,

$$\hat{Q} = \sum_a^{\text{virtual}} |\phi_a\rangle\langle\phi_a| = 1 - \sum_p^{\text{occupied}} |\phi_p\rangle\langle\phi_p| \tag{2.55}$$

and the mean field operator $\hat{W}^r_s$, which is given by, in the coordinate space,

$$W^r_s(\boldsymbol{r}_1) = \int d\boldsymbol{r}_2\phi^*_r(\boldsymbol{r}_2)h_2(\boldsymbol{r}_1,\boldsymbol{r}_2)\phi_s(\boldsymbol{r}_2) = \int d\boldsymbol{r}_2\frac{\phi^*_r(\boldsymbol{r}_2)\phi_s(\boldsymbol{r}_2)}{|\boldsymbol{r}_1-\boldsymbol{r}_2|}. \tag{2.56}$$

Thus, the equations of motion of dynamical core and active orbitals are obtained as,

$$i|\dot{\phi_p}\rangle = \hat{Q}\left[\hat{h}_1|\phi_p\rangle + \sum_{o,q,r,s}^{\text{occupied}} \hat{W}^r_s|\phi_q\rangle\, P^{qs}_{or}(D^{-1})^o_p\right] + i\sum_q^{\text{occupied}} |\phi_q\rangle\, X^q_p, \tag{2.57}$$

with $\{X_p^q\}$ given by Eqs. (2.2), (2.47) and (2.48).

2.3 Implementation of the TD-ORMAS method

In this section, we explain our implementation of the TD-ORMAS method, which considers an atom under a linearly polarized laser field. The polarization axis is z direction. Especially, the spatial discretization method of orbitals and the time propagation method for orbitals and CI coefficients are described.

We assume orbitals in the polar coordinate (r, θ, ϕ), and that orbitals are expanded with $L_{\max}$ spherical harmonics,

$$\phi_p(r,\theta,\phi) = \sum_{l=0}^{L_{\max}} \sum_{m=-l}^{l} \frac{\phi_p^{lm}(r)}{r} Y_{lm}(\theta,\phi). \tag{2.58}$$

$\phi_p^{lm}(r)$ denote a radial part of orbitals with an angular quantum number l and a magnetic quantum number m. The radial part is discretized with the finite-element discrete-variable-representation (FEDVR) basis [51–53], which we describe the detail below. In numerical simulations, we first prepare a ground state by using the imaginary time propagation, and next propagate the ground state under a laser field in real-time. In both imaginary and real-time propagation, we employ the exponential integrator scheme [54], which the detail is also given below.

2.3.1 Finite-element discrete-variable-representation basis

The FEDVR basis is based on the finite element method with the Gauss-Lobatto quadrature and polynomial basis passing through quadrature points. We consider a radial region $[0, R_{\max}]$ and divide it into N_{FE} finite elements with boundaries

$$r^{(0)} = 0, r^{(1)}, \cdots, r^{(N_{\mathrm{FE}}-1)}, r^{(N_{\mathrm{FE}})} = R_{\max}.$$

In i th finite element $[r^{(i-1)}, r^{(i)}]$, we set M_{GL} th order Gauss-Lobatto quadrature points $\{r_{i,m} \mid m = 1, \cdots, M_{\mathrm{GL}}\}$, whose first and last points are identical to the left and right boundary of a given region, and then Lagrange polynomial functions associated with the m th quadrature point can be defined as,

$$L_{i,m}(r) = \prod_{m' \neq m} \frac{r - r_{i,m'}}{r_{i,m} - r_{i,m'}}, \tag{2.59}$$

where this function is defined only in $[r^{(i-1)}, r^{(i)}]$ and has zero value outside the region. This polynomial has a delta function like property of $L_{i,m}(r_{i,m'}) = \delta_{m'}^m$, which can be easily checked by inserting $r_{i,m'}$ into Eq. (2.59). By using this property, we can construct an

approximately orthonormal basis with the Gauss-Lobatto quadrature weights $\{w_{i,m}\}$,

$$\tilde{L}_{i,m}(r) = \frac{L_{i,m}(r)}{\sqrt{w_{i,m}}}, \tag{2.60}$$

$$\int dr \tilde{L}_{i,m}(r)\tilde{L}_{i,m'}(r) \simeq \sum_{k=1}^{M_{\mathrm{GL}}} w_{i,k}\tilde{L}_{i,m}(r_{i,k})\tilde{L}_{i,m'}(r_{i,k}) = \delta^m_{m'}. \tag{2.61}$$

M_{GL} th order Gauss-Lobatto quadrature can exactly integrate up to $2M_{\mathrm{GL}} - 3$ th order polynomials, but $\tilde{L}_{i,m}(r)\tilde{L}_{i,m'}(r)$ is $2M_{\mathrm{GL}} - 2$ th order polynomial. This is the reason why the orthonormality holds only within the approximation. The FEDVR method uses $\tilde{L}_{i,m'}(r)$ as i th finite element basis.

Though we can construct a basis set supporting the whole region $[0, R_{\mathrm{max}}]$ by collecting the finite element basis belonging to each finite element, this basis set can describe a discontinuous function at the finite element boundaries. Thus, to ensure the continuity of discretized functions, we need to remove finite element basis functions associated with quadrature points at each finite element boundary except for the left boundary of the first finite element ($r = 0$) and the right boundary of the last finite element ($r = R_{\mathrm{max}}$), and introduce the bridging function instead,

$$\frac{L_{i,M_{\mathrm{GL}}}(r) + L_{i+1,1}(r)}{\sqrt{w_{i,M_{\mathrm{GL}}} + w_{i+1,1}}}. \tag{2.62}$$

Then we obtain FEDVR basis $f_{i,m}(r)$,

$$f_{i,m}(r) = \begin{cases} \dfrac{L_{i,M_{\mathrm{GL}}}(r) + L_{i+1,1}(r)}{\sqrt{w_{i,M_{\mathrm{GL}}} + w_{i+1,1}}} & m = 1, M_{\mathrm{GL}} \text{ and } i \neq 1, N_{\mathrm{FE}} \\ \tilde{L}_{i,m}(r) & \text{else} \end{cases}. \tag{2.63}$$

For simplicity, we relabel $f_{i,m}(r)$ as $f_k(r)$, where k denote a set of indices (i, m), and define integral wights $\tilde{w}_k$ for the whole region $[0, R_{\mathrm{max}}]$ as,

$$\tilde{w}_k = \tilde{w}_{i,m} = \begin{cases} w_{i,M_{\mathrm{GL}}} + w_{i+1,1} & m = 1, M_{\mathrm{GL}} \text{ and } i \neq 1, N_{\mathrm{FE}} \\ w_{i,m} & \text{else} \end{cases}. \tag{2.64}$$

With this definition, the orthonormality of the FEDVR basis can be expressed as,

$$\int_0^{R_{\mathrm{max}}} dr f_k(r) f_{k'}(r) \simeq \sum_\kappa \tilde{w}_\kappa f_k(r_\kappa) f'_k(r_\kappa) = \delta^k_{k'}. \tag{2.65}$$

The radial part of orbitals $\phi^{lm}_p(r)$ can be approximated or discretized with the FEDVR

basis,

$$\phi_p^{lm}(r) \simeq \sum_k c_{klm}^p f_k(r), \tag{2.66}$$

$$c_{klm}^p = \sqrt{\tilde{w}_k}\phi_p^{lm}(r_k). \tag{2.67}$$

The second equation approximates $\int dr f_k(r)\phi_p^{lm}(r)$ with the Gauss-Lobbato quadrature. The expansion coefficient c_{klm} is determined only by a function value $\phi_p^{lm}(r_k)$ at a grid point r_k. Discrete-variable-representation (DVR) means this property. A local potential $V(r)$, for example Coulomb potential, is discretized as a diagonal matrix,

$$V_{kk'} = \int dr f_k(r)V(r)f_{k'}(r) \simeq V(r_k)\delta_{k'}^k. \tag{2.68}$$

The radial derivative matrix $\{K_{kk'}^r\}$ is evaluated as,

$$K_{kk'}^r = \int dr f_k(r)\frac{\partial}{\partial r}f_{k'}(r) = \sum_\kappa \tilde{w}_\kappa f_k(r_\kappa)\frac{\partial f_{k'}}{\partial r}(r_\kappa) \tag{2.69}$$

and the radial derivative of polynomial $\frac{\partial L_{i,m}}{\partial r}(r)$ at a grid point $r_{i,m'}$ required for the evaluation of Eq. (2.69) is given by,

$$\frac{\partial L_{i,m}}{\partial r}(r_{i,m'}) = \begin{cases} \dfrac{1}{2w_{i,m}}(\delta_1^m - \delta_{M_{\mathrm{GL}}}^m) & m = m' \\ \dfrac{1}{r_{i,m} - r_{i,m'}} \displaystyle\prod_{\mu\neq m,m'} \frac{r_{i,m'} - r_{i,\mu}}{r_{i,m} - r_{i,\mu}} & m = m' \end{cases}. \tag{2.70}$$

The second derivative of FEDVR basis has a delta-like singularity at finite element boundaries due to the discontinuity of the finite element basis $L_{i,m}(r)$. However, the second derivative matrix $T^r = \{T_{kk'}^r\}$ can be evaluated by using integration by parts as well as the usual finite element method,

$$T_{kk'}^r = \int dr f_k(r)\frac{\partial^2}{\partial r^2}f_{k'}(r) = -\int dr \partial f_k \partial r(r)\frac{\partial f_{k'}}{\partial r}(r) \tag{2.71}$$

$$= -\sum_\kappa \tilde{w}_\kappa \frac{\partial f_k}{\partial r}(r_\kappa)\frac{\partial f_{k'}}{\partial r}(r_\kappa). \tag{2.72}$$

Both the first and second derivative matrices are band matrices since the FEDVR basis lies only in one finite element or two finite elements. This structure enables efficient derivative operations.

By inserting Eq. (2.66) into Eq. (3.8), we obtain the following orbital discretization,

$$\phi_p(r,\theta,\phi) = \sum_{klm} c_{klm}^p \frac{f_k(r)}{r}Y_{lm}(\theta,\phi), \tag{2.73}$$

where $\frac{f_k(r)}{r}Y_{lm}(\theta,\phi)$ is called the spherical FEDVR basis [24, 52].

2.3.2 Spatial discretization of the equations of motion

The Equation of motion for orbitals (2.57) is converted into a vector equation by inserting Eq. (4.15) and projecting onto a FEDVR basis,

$$i\dot{\boldsymbol{c}}^p = (1 - \sum_q \boldsymbol{c}^q \boldsymbol{c}^{q\dagger}) \left[\tilde{h}_1 \boldsymbol{c}^p + \sum_{o,q,r,s} \tilde{W}_s^r \boldsymbol{c}^q P_{or}^{qs} (D^{-1})_p^o \right] + i \sum_q \boldsymbol{c}^q X_p^q. \tag{2.74}$$

$\boldsymbol{c}^p$ denote a coefficient vector of orbital p, whose elements are defined as $\{c_{klm}^p\}$. $\tilde{h}_1$ and $\tilde{W}_s^r$ are matrices of the single-electron term of the Hamiltonian h_1 and the mean field potential W_s^r (Eq. (2.56)), respectively. This section considers an atom, whose nuclear Coulomb potential is given by $V_{\mathrm{N}}(r,\theta,\phi) = Z/r$ with nuclear charge Z, under a z polarized laser field. Their matrix elements in the FEDVR basis are defined as,

$$\tilde{h}_{1\,k'l'm'}^{klm} = \int r^2 dr \sin\theta d\theta d\phi \frac{f_k(r)}{r} Y_{lm}^*(\theta,\phi) \left[-\frac{1}{2}\Delta - \frac{Z}{r} - iA_z(t)\frac{\partial}{\partial z} \right] \frac{f_{k'}(r)}{r} Y_{l'm'}(\theta,\phi), \tag{2.75}$$

$$\tilde{W}_{s\,k'l'm'}^{r\,klm} = \int r^2 dr \sin\theta d\theta d\phi \frac{f_k(r)}{r} Y_{lm}^*(\theta,\phi) W_s^r(r,\theta,\phi) \frac{f_{k'}(r)}{r} Y_{l'm'}(\theta,\phi). \tag{2.76}$$

$A_z(t)$ denotes the z component of a laser vector potential.

The Equation of motion for CI coefficients (2.30) itself is also a vector equation,

$$i\dot{\boldsymbol{C}} = (\tilde{H} - i\tilde{X})\boldsymbol{C}, \tag{2.77}$$

where $\boldsymbol{C}$ is a coefficient vector $\{C_I\}$, and $\tilde{H} = \{H_{IJ}\}$ and $X = \tilde{\{X_{IJ}\}}$ are matrices defined as

$$\begin{aligned} H_{IJ} &= \langle I|\hat{\Phi}_C^\dagger \hat{H} \hat{\Phi}_C|J\rangle \\ &= \sum_{\mu\nu} h_1{}_\nu^\mu \langle I|\hat{\Phi}_C^\dagger \hat{E}_\nu^\mu \hat{\Phi}_C|J\rangle + \frac{1}{2}\sum_{\mu\nu\lambda\gamma} h_{2\nu\gamma}^{\mu\lambda} \langle I|\hat{\Phi}_C^\dagger \hat{E}_{\nu\gamma}^{\mu\lambda} \hat{\Phi}_C|J\rangle, \end{aligned} \tag{2.78}$$

$$X_{IJ} = \langle I|\hat{\Phi}_C^\dagger \hat{X} \hat{\Phi}_C|J\rangle = X_\nu^\mu \langle I|\hat{\Phi}_C^\dagger \hat{E}_\nu^\mu \hat{\Phi}_C|J\rangle, \tag{2.79}$$

with $h_1{}_\nu^\mu = (\boldsymbol{c}^\mu)^\dagger \tilde{h}_1 \boldsymbol{c}^\nu$ and $h_{2\nu\gamma}^{\mu\lambda} = \langle\phi_\mu|\hat{W}_\gamma^\lambda|\phi_\nu\rangle = (\boldsymbol{c}^\mu)^\dagger \tilde{W}_\gamma^\lambda \boldsymbol{c}^\nu$. X_ν^μ, defined in Sec. 2.2, is calculated with $h_1{}_\nu^\mu$ and $\langle\phi_\mu|\hat{W}_\gamma^\lambda|\phi_\nu\rangle$. We evaluate the matrices $\tilde{h}_1$ and $\tilde{W}_s^r$ in the following subsections.

The matrix elements of the single-electron term

We first calculate the matrix elements of $\tilde{h}_1$. The Laplace operator in the polar coordinate is expressed as,

$$\Delta = \frac{1}{r}\frac{\partial^2}{\partial r^2}r + \frac{1}{r^2}\left[\frac{1}{\sin\theta}\frac{\partial}{\partial\theta}\left(\sin\theta\frac{\partial}{\partial\theta}\right) + \frac{1}{\sin\theta}\frac{\partial^2}{\partial\phi^2}\right]. \tag{2.80}$$

The inside of the square bracket of the second term is the square of the angular momentum operator. Thus, the Laplacian matrix element $L^{klm}_{k'l'm'}$ is given by,

$$\begin{aligned} L^{klm}_{k'l'm'} &= \int r^2 dr \sin\theta d\theta d\phi \frac{f_k(r)}{r} Y^*_{lm}(\theta,\phi)\Delta\frac{f_{k'}(r)}{r}Y_{l'm'}(\theta,\phi) \\ &= \left(T^r_{kk'} - \frac{l(l+1)}{r_k^2}\delta^k_{k'}\right)\delta^l_{l'}\delta^m_{m'}, \end{aligned} \tag{2.81}$$

where $T^r_{kk'}$ denotes the radial second derivative matrix element defined in Eq. (2.71). The atomic nuclear Coulomb potential is local and spherical symmetric, and thus the matrix element $V^{klm}_{k'l'm'}$ is straightforward calculated as,

$$V_{\mathrm{N}}{}^{klm}_{k'l'm'} = -\frac{Z}{r_k}\delta^k_{k'}\delta^l_{l'}\delta^m_{m'}. \tag{2.82}$$

For the laser field potential, the derivative operator of the z direction is given as, in the polar coordinate,

$$\frac{\partial}{\partial z} = \cos\theta\frac{\partial}{\partial r} - \frac{\sin\theta}{r}\frac{\partial}{\partial\theta}, \tag{2.83}$$

and then the matrix element $V_{\mathrm{L}}{}^{klm}_{k'l'm'}$ is given as

$$V_{\mathrm{L}}{}^{klm}_{k'l'm'} = -iA_z(t)\left(K^r_{kk'} - \frac{(l'+1)\delta^l_{l'+1} - (l+1)\delta^{l+1}_{l'}}{r_l}\delta_{kk'}\right)\alpha^{lm}_{l'm'}, \tag{2.84}$$

$$\alpha^{lm}_{l'm'} = \int \sin\theta d\theta d\phi Y^*_{lm}(\theta,\phi)\cos\theta Y_{l'm'}(\theta,\phi) \tag{2.85}$$

$$= \left[\sqrt{\frac{(l'+1)^2 - m'^2}{(2l'+1)(2l'+3)}}\delta^l_{l'+1} + \sqrt{\frac{(l+1)^2 - m'^2}{(2l+1)(2l+3)}}\delta^{l+1}_{l'}\right]\delta^m_{m'}. \tag{2.86}$$

Thus, the matrix element of the single electron term reads

$$\tilde{h}_1{}^{klm}_{k'l'm'} = -\frac{1}{2}L^{klm}_{k'l'm'} + V_{\mathrm{N}}{}^{klm}_{k'l'm'} + V_{\mathrm{L}}{}^{klm}_{k'l'm'}. \tag{2.87}$$

The matrix elements of the mean field potential

The mean field potential $W_s^r(\boldsymbol{r}_1)$ can be obtained by directly integrating

$$W_s^r(\boldsymbol{r}_1) = \int d\boldsymbol{r}_2 \frac{\phi_r^*(\boldsymbol{r}_2)\phi_s(\boldsymbol{r}_2)}{|\boldsymbol{r}_1 - \boldsymbol{r}_2|}. \tag{2.88}$$

However, this approach has disadvantages in accuracy due to the singularity $1/|\boldsymbol{r}_1 - \boldsymbol{r}_2|$ and requires huge computational costs that scales $\mathcal{O}(N_{\text{grid}}^2)$, where N_{grid} denotes the total number of spatial grids. For this potential, by taking advantage of $1/|\boldsymbol{r}_1 - \boldsymbol{r}_2|$ being a Green function of the Laplacian, solving the following Poisson equation,

$$\Delta W_s^r(\boldsymbol{r}) = -4\pi\phi_r^*(\boldsymbol{r})\phi_s(\boldsymbol{r}), \tag{2.89}$$

is more accurate and efficient [52]. To reduce this Poissonn equation in 3 dimensional space into a radial Poisson equation, we introduce the multipole expansion of $1/|\boldsymbol{r}_1 - \boldsymbol{r}_2|$,

$$\frac{1}{|\boldsymbol{r}_1 - \boldsymbol{r}_2|} = \sum_{l=0}^{\infty}\sum_{m=-l}^{l} \frac{4\pi}{2l+1}\frac{r_<^l}{r_>^{l+1}} Y_{lm}(\theta_1,\phi_1)Y_{lm}^*(\theta_2,\phi_2), \tag{2.90}$$

$$r_< = \min(r_1, r_2),\ r_> = \max(r_1, r_2), \tag{2.91}$$

and the spherical harmonics expansions of $W_s^r(\boldsymbol{r})$ and $\phi_r^*(\boldsymbol{r})\phi_s(\boldsymbol{r})$,

$$W_s^r(\boldsymbol{r}) = \sum_{lm} \frac{(V_s^r)_{lm}(r)}{r} Y_{lm}(\theta,\phi), \tag{2.92}$$

$$\phi_r^*(\boldsymbol{r})\phi_s(\boldsymbol{r}) = \sum_{lm} \frac{(\rho_s^r)_{lm}(r)}{r} Y_{lm}(\theta,\phi). \tag{2.93}$$

By inserting Eqs. (2.90), (2.92) and (2.93) into Eq. (2.89), we obtain the radial Poisson equation of $(V_s^r)_{lm}(r)$,

$$\left(\frac{\partial^2}{\partial r^2} - \frac{l(l+1)}{r^2}\right)(V_s^r)_{lm}(r) = -4\pi(\rho_s^r)_{lm}(r), \tag{2.94}$$

with the boundary conditions,

$$(V_s^r)_{lm}(0) = 0, \tag{2.95}$$

$$(V_s^r)_{lm}(R_{\max}) = \frac{1}{R_{\max}^{(2l+1)}}\int_0^{R_{\max}} dr r(\rho_s^r)_{lm}(r). \tag{2.96}$$

This radial Poisson equation is discretized with the FEDVR basis and transformed into a linear equation,

$$\tilde{L}_l(\boldsymbol{\rho}_s^r)_{lm}(\boldsymbol{V}_s^r)_{lm} = -4\pi(\boldsymbol{\rho}_s^r)_{lm}, \tag{2.97}$$

where $\tilde{L}_l = \{(\tilde{L}_l)_{k'}^k\}$ is the matrix of $\left(\frac{\partial^2}{\partial r^2} - \frac{l(l+1)}{r^2}\right)$, and the coefficient vector $(\boldsymbol{\rho}_s^r)_{lm} =$

$\{(\rho_s^r)_{klm}\}$ is evaluated as

$$(\rho_s^r)_{klm} = \frac{1}{\sqrt{\tilde{w}_k}}(c_{klm}^r)^* c_{klm}^s, \tag{2.98}$$

where we use the DVR property that the each coefficient corresponds to the discretized function value at each grid point. As a solution of Eq. (2.97), we obtain $(\boldsymbol{V}_s^r)_{lm} = \{(V_s^r)_{klm}\}$, and the mean field potential is given by

$$W_s^r(\boldsymbol{r}) = \sum_{klm}(V_s^r)_{klm}\frac{f_k(r)}{r}Y_{lm}(\theta,\phi). \tag{2.99}$$

Finally, the matrix elements of $W_s^r(\boldsymbol{r})$ (Eq. (2.76)) is evaluated as

$$\tilde{W}_{s\,k'l'm'}^{rklm} \simeq \sum_{l_1}\sum_{m_1}\frac{(V_s^r)_{kl_1m_1}}{\sqrt{\tilde{w}_k}r_k}\delta_{k'}^k c_{l_1m_1}, \tag{2.100}$$

$$\begin{aligned} c_{l_1m_1} &= \int \sin\theta d\theta d\phi Y_{lm}^*(\theta,\phi)Y_{l_1m_1}(\theta,\phi)Y_{l'm'}(\theta,\phi) \\ &= \int_{-1}^{1} dx P_{lm}(x)P_{l_1m_1}(x)P_{l'm'}(x)\delta_{m_1+m'}^m, \end{aligned} \tag{2.101}$$

where $P_{lm}(x)$ denotes a normalized associated Legendre polynomial. The integral over the product of three normalized associated Legendre polynomials is evaluated by the Gauss-Legendre quadrature with a sufficient order for the polynomials.

2.3.3 The exponential integrator

The equations of motion (Eqs. (2.74) and (2.30)) are usually stiff differential equations. Especially, the single-electron term $\tilde{h}_1$ including the Laplacian and Coulomb potential with the singularity makes time propagation unstable. To achieve stable time propagation with a moderate time-step size , we employ the exponential integrator scheme, which solves a linear and stiff term exactly and mitigates the stiffness. We first review the exponential integrator for general cases, and next describe our application to the TD-ORMAS method.

A review of the exponential integrator

We consider a simple nonlinear partial derivative equation,

$$\frac{\partial}{\partial t}u(t) = Lu(t) + N(u(t)), \tag{2.102}$$

where $u(t)$ is a function we want to propagate, L denote a linear operator, for example the Laplacian, and $N(u(t))$ denotes a nonlinear term. This equation has a formal exact

solution,

$$u(t) = \mathrm{e}^{Lt}u(t) + \int_0^t d\tau \mathrm{e}^{L(t-\tau)}N(u(\tau)). \tag{2.103}$$

In time discretization, we assume that a solution $u(t_n)$ at the n th time step, and then the next time step solution is obtained as

$$u(t_{n+1}) = \mathrm{e}^{Lh_n}u(t_n) + \int_0^{h_n} d\tau \mathrm{e}^{L(h_n-\tau)}N(u(\tau)), \tag{2.104}$$

$$h_n = t_{n+1} - t_n. \tag{2.105}$$

This update scheme is called the exponential integrator. The contribution of the linear operator L is exactly integrated as e^{Lh_n}, and thus this scheme has a great advantage in the time-propagation stability in a case that L is a stiff operator. The integral of the nonlinear term can be evaluated with various approaches [54–56].

In our application, we use the 4th order Runge-Kutta type scheme [54] for the integral in Eq. (2.104), which is called the 4th order exponential time differencing Runge-Kutta method. This scheme first computes three preliminary estimations, similarly to the usual Runge-Kutta method,

$$a_n = \mathrm{e}^{Lh_n/2}u(t_n) + \frac{h_n}{2}\frac{\mathrm{e}^{Lh_n/2} - I}{Lh_n/2}N(u(t_n)), \tag{2.106a}$$

$$b_n = \mathrm{e}^{Lh_n/2}u(t_n) + \frac{h_n}{2}\frac{\mathrm{e}^{Lh_n/2} - I}{Lh_n/2}N(a_n), \tag{2.106b}$$

$$c_n = \mathrm{e}^{Lh_n/2}a_n + \frac{h_n}{2}\frac{\mathrm{e}^{Lh_n/2} - I}{Lh_n/2}(2N(b_n) - N(a_n)), \tag{2.106c}$$

and finally obtain the next time-step solution,

$$\begin{aligned} u(t_{n+1}) = \mathrm{e}^{Lh_n}u(t_n) &+ h_n\frac{-4 - Lh_n + \mathrm{e}^{Lh_n}(4 - 3Lh_n + (Lh_n)^2)}{L^3h_n^3}N(u(t_n)) \\ &+ h_n\frac{4 + 2Lh_n + 2\mathrm{e}^{Lh_n}(-2 + Lh_n)}{L^3h_n^3}(N(a_n) + N(b_n)) \\ &+ h_n\frac{-4 - 3Lh_n - (Lh_n)^2\mathrm{e}^{Lh_n}(4 - Lh_n)}{L^3h_n^3}N(c_n). \end{aligned} \tag{2.107}$$

Application of the exponential integrator to the TD-ORMAS method

To adapt the exponential integrator to the TD-ORMAS method, we split the equations of motion (2.74) and (2.30) into linear terms and nonlinear terms. The equation of motion for orbitals (2.74) is transformed as

$$\dot{\boldsymbol{c}}^p = -i\tilde{h}_1\boldsymbol{c}^p + \sum_q (i\boldsymbol{c}^{q\dagger}\tilde{h}_1\boldsymbol{c}^p + X_p^q)\boldsymbol{c}^q - i(1 - \sum_q \boldsymbol{c}^q\boldsymbol{c}^{q\dagger})\sum_{o,q,r,s}\tilde{W}_s^r\boldsymbol{c}^q P_{or}^{qs}(D^{-1})_p^o. \tag{2.108}$$

We treat only the first term of the right hand side as a linear term, and the rest as a nonlinear term. For the equation of motion for CI coefficients (2.77), we treat it as a linear equation, and the nonlinear term is absent.

Matrix functions e^A and $\varphi(A) = (\mathrm{e}^A - I)/A$ with a matrix A required in Eq. (2.106) are evaluated by $[3,3]$ order Padé approximation (3rd order for both the numerator and denominator). The other matrix functions in Eq. (2.107) are evaluated by substituting the Padé approximation of $\varphi(A)$ into the matrix exponential functions of Eq. (2.107).

Chapter 3

Application of infinite-range exterior complex scaling to the TD-ORMAS method

One source of the huge computational cost of the TD-MCSCF simulations arises from a large simulation box required to accommodate electrons ejected through laser-induced ionization. These electrons can fly infinitely far away in principle. Therefore, the use of an efficient absorbing boundary is key to reducing the computational cost and achieving larger scale simulations. In this work, we introduce efficient absorbing boundaries of exterior complex scaling (ECS) [31] and infinite-range exterior complex scaling (irECS) [32] to the TD-ORMAS method [15, 57].

This chapter is organized as follows. In Sec. 3.1, we briefly review exterior complex scaling for a single-electron system. In Secs. 3.2 and 3.3, we describe our numerical implementation of ECS and irECS, adopting the spherical finite-element discrete variable representation (FEDVR) basis. Section 3.4 discusses how to apply ECS and irECS to the TD-ORMAS method. In Sec. 3.5, we numerically assess the efficiency and accuracy of our application of ECS and irECS. We consider atomic systems in the polar coordinate for the application of ECS described in this chapter. However, our application can be straightforwardly extended to general coordinate systems such as the Cartesian coordinate.

3.1 Exterior complex scaling for a single-electron system

Let us consider TDSE for a single-electron system in a laser field with the velocity-gauge, since ECS as an absorbing boundary properly works in the velocity-gauge [31],

$$\begin{aligned} i\frac{\partial}{\partial t}\Psi(\boldsymbol{r},t) &= h_1(t)\Psi(\boldsymbol{r},t) \\ &= \left(-\frac{\nabla^2}{2} + V_N(\boldsymbol{r}) - i\boldsymbol{A}(t)\cdot\nabla\right)\Psi(\boldsymbol{r},t). \end{aligned} \tag{3.1}$$

ECS in the polar coordinate is based on the coordinate scaling,

$$r \to R(r) = \begin{cases} r & (r < R_0) \\ R_0 + (r - R_0)\mathrm{e}^{\lambda + i\eta} & (r > R_0), \end{cases} \tag{3.2}$$

where λ and η is real numbers, and specifically η is called a scaling angle. For $\eta > 0$, outgoing waves exponentially decay at radii $r > R_0$ and numerically vanish before they reach the simulation boundary and are unphysically reflected.

The transformation Eq. (3.2) defines an "exterior complex scaling operator" $\hat{U}_{\eta R_0}$

$$(\hat{U}_{\eta R_0}\Psi)(\boldsymbol{r}) := \begin{cases} \Psi(\boldsymbol{R}(r)) & (r < R_0) \\ \mathrm{e}^{\frac{\lambda + i\eta}{2}} \dfrac{R(r)}{r} \Psi(\boldsymbol{R}(r)) & (r > R_0), \end{cases} \tag{3.3}$$

where,

$$\boldsymbol{R}(r) = \frac{R(r)}{r}\boldsymbol{r}. \tag{3.4}$$

The factor $\mathrm{e}^{\frac{\lambda+i\eta}{2}} R(r)/r$ ensures that $U_{\eta R_0}$ is unitary for $\eta = 0$. In the unitary case, one can replace $h_1(t)$ in Eq. (3.1) with

$$\hat{h}_{\eta=0R_0}(t) = \hat{U}_{\eta=0R_0}\hat{h}_1(t)\hat{U}^{-1}_{\eta=0R_0}, \tag{3.5}$$

without changing the dynamics. The solution for the scaled Hamiltonian is trivially $\Psi_{\eta=0R_0} := \hat{U}_{\eta=0R_0}\Psi$ and coincides with the unscaled solution Ψ for $r < R_0$.

In the ECS case for $\eta > 0$, the scaled operator is $\hat{h}_{\eta R_0}(t) = \hat{h}_1(t)$ on $r < R_0$ and for $r > R_0$

$$\hat{h}_{\eta R_0} = -\frac{1}{2}\nabla^2_{\eta R_0} + V_{\mathrm{N}}[\boldsymbol{R}(r)] - i\boldsymbol{A}(t)\cdot\nabla_{\eta R_0}, \tag{3.6}$$

with the scaled nabla operator $\nabla_{\eta R_0}$ given by

$$\begin{aligned} \nabla_{\eta R_0} &= \boldsymbol{e}_r \frac{1}{\mathrm{e}^{\lambda + i\eta} r} \frac{\partial}{\partial r} r \\ &+ \frac{1}{R(r)\sin\theta}\left(\boldsymbol{e}_\theta \frac{\partial}{\partial\theta}\sin\theta + \boldsymbol{e}_\phi \frac{\partial}{\partial\phi}\right). \end{aligned} \tag{3.7}$$

Note that terms depending on radial coordinates are only different from the original Hamiltonian. This form of the scaled operator is formally obtained by analytically continuing that of the unitary case [Eq. (3.5)] with $\eta = 0 \to \eta \neq 0$ [58]. The essential point of ECS is that, given sufficient analyticity properties of $h_{\eta R_0}$, also for $\eta > 0$ the solution $\Psi_{\eta R_0}$ remains invariant on $r < R_0$, while it decays exponentially in the absorbing region [32].

For the numerical solution of the complex scaled TDSE with the simple scaling of Eq. (3.6) one needs to ensure that the discretization method can represent the discontinuous behavior of the solution at $r = R_0$, Eq. (3.3). This is the case for the FEDVR basis set described below.

While ECS is usually applied on a finite discretization range, one can infinitely extend

the scaled region by using a finite number of exponentially damped basis functions [32]. This method, called infinite-range ECS, not only has a conceptual advantage of simulating the entire space with artificially modifying neither the system Hamiltonian nor the wave functions, but also has achieved high accuracy and efficiency with a considerably smaller number of basis functions [32].

3.2 Implementation of ECS with FEDVR method

In this work, we implement ECS and irECS with a spherical-FEDVR basis [51, 52], whose details are given in Subsec. 2.3.1. Here, as usual, we set $\lambda = 0$ in the scaling factor. The implementation of usual ECS (not infinite-range) for single-electron systems with a spherical FEDVR basis has been discussed by Rescigno and McCurdy [52, 59]. We follow their approaches, where the factor $e^{\frac{\lambda+i\eta}{2}}$ appearing in Eq. (3.3) is dropped off, and the factor $R(r)/r$ is absorbed into a radial part of a wave function and basis functions. Namely, we consider the following scaled wave function and discretization,

$$\frac{R(r)}{r}\Psi(R(r),\theta,\phi) = \sum_{l=0}^{L_{\max}} \sum_{m=-l}^{l} \frac{\Psi_{lm}(R(r))}{r} Y_{lm}(\theta,\phi), \tag{3.8}$$

$$\Psi_{lm}(R(r)) = \sum_{k} c_{klm} f_k(r), \tag{3.9}$$

where $f_k(r)$ and $Y_{lm}(\theta,\phi)$ denote a FEDVR basis and a spherical harmonics, respectively.

Since we drop the factor $e^{\frac{\lambda+i\eta}{2}}$, the scaled wave function is continuous. However, the first and second derivatives are still discontinuous. To correctly represent these discontinuous behaviors, we set R_0 to be identical to a finite element boundary. Matrix elements of the scaled single-electron Hamiltonian (Eq. (3.6)) in the FEDVR basis are obtained by simply replacing each operator and potential with scaled one in Eqs. (2.68), (2.69) and (2.71).

3.3 Implementation of infinite-range ECS with extended FEDVR method

In the original development of irECS presented by Scrinzi [32], Laguerre polynomials times an exponential weight function has been used as an infinite-range basis function in the last finite element. To combine the original concept of irECS and our FEDVR implementation, we introduce Gauss-Laguerre-Radau quadrature points [60, 61] to construct DVR basis functions in the last finite element extending to infinity. Gauss-Laguerre-Radau quadrature approximates the semi-infinite integral of an exponentially damped function

as

$$\int_{r_\mathrm{L}}^{\infty} dr e^{-\alpha(r-r_L)} f(r) \approx \sum_{i=1}^{N_\mathrm{grid}} w_i f(r_i) \tag{3.10}$$
$$r_L = r_1 < r_2 < \cdots < r_{N_\mathrm{grid}}$$

with w_i's and r_i's being quadrature weights and points, The left endpoint is included in the quadrature points. which enables us to construct FEDVR-like basis functions introduced below.

For irECS, we use the following exponentially damped functions as the finite element basis functions on the last element,

$$y_i(r) = \begin{cases} e^{-\frac{\alpha}{2}(r-r_L)} \dfrac{L_i(r)}{\sqrt{w_i}} & (r \geq r_L) \\ 0 & (r < r_L) \end{cases} \tag{3.11}$$

with Lagrange polynomials,

$$L_i(r) = \prod_{j \neq i} \frac{r - r_j}{r_i - r_j}. \tag{3.12}$$

Note that these basis functions are not truncated within a finite range unlike usual FEDVR basis, but extend to the infinite range and decay exponentially due to the factor $e^{-\frac{\alpha}{2}(r-r_L)}$. This infinitely-extended exponential tail can describe exponentially damped wave functions by ECS and provides high accuracy with a small number of basis functions.

The basis functions appear as orthonormal under the approximate Gauss quadrature,

$$\begin{aligned} \int_0^{\infty} dr\, y_i(r) y_j(r) &\approx \sum_{k=1}^{N_\mathrm{grid}} w_k e^{\alpha(r_k - r_L)} y_i(r_k)^* y_j(r_k) \\ &= \delta_{ij}. \end{aligned} \tag{3.13}$$

Thus, in the last finite element a radial part of scaled wave functions $\varphi(r)$ is expressed by

$$\varphi(r) \approx \sum_{i}^{N_\mathrm{grid}} c_i y_i(r) \tag{3.14}$$

$$c_i = \int_0^{\infty} dr\, y_i(r) \varphi(r) \approx \sqrt{e^{-\frac{\alpha}{2}(r_i - r_L)} w_i}\, \varphi(r_i). \tag{3.15}$$

Likewise, the matrix elements of one-body potentials are diagonal,

$$V_{ij} = \int_0^{\infty} dr\, y_i(r) V(r) y_j(r) \approx V(r_i) \delta_{ij}. \tag{3.16}$$

The first derivative of the basis functions are given by

$$\frac{\partial}{\partial r} y_i(r) = \frac{1}{\sqrt{w_i}} e^{-\frac{1}{2}\alpha(r-r_L)} P_i(r), \tag{3.17}$$

where

$$\begin{aligned} P_i(r) &= -\frac{\alpha}{2} L_i(r) + \frac{\partial}{\partial r} L_i(r) \\ &= \begin{cases} \dfrac{1}{r_i - r_j} \displaystyle\prod_{k \neq i,j} \frac{r_j - r_k}{r_i - r_k} & \text{for } r = r_j,\ i \neq j \\ -\dfrac{1}{2w_1} \delta_{i1} & \text{for } r = r_j,\ i = j. \end{cases} \end{aligned} \tag{3.18}$$

Thus, the matrix elements of the radial second derivative operator can be expressed under Gauss quadrature by using a partial integral,

$$\begin{aligned} \int_0^\infty dr\, y_i(r) \frac{\partial^2}{\partial r^2} y_j(r) &= -\int_0^\infty dr \frac{\partial}{\partial r}(y_i(r)) \frac{\partial}{\partial r}(y_j(r)) \\ &\approx -\sum_k \frac{w_k}{\sqrt{w_i w_j}} P_i(r_k) P_j(r_k) \end{aligned} \tag{3.19}$$

For simplicity, we have discussed without considering the bridge function to connect the element boundary between the last element and the second to last element. In the actual implementation, we introduced this as well as in the usual FEDVR method [51].

3.4 Application of ECS to the TD-ORMAS multielectron dynamics

In this section, we discuss how to apply ECS to TD-ORMAS method of the multielectron dynamics involving the interelectronic Coulomb interaction. By analogy with the single-electron case, we propagate the scaled orbital function $\hat{U}_{\eta R_0} |\phi_p\rangle$ rather than the unscaled $|\phi_p\rangle$, by transforming Eq. (2.57) into the scaled equation of motion (EOMs) of the orbitals,

$$\begin{aligned} i\hat{U}_{\eta R_0} |\dot{\phi_p}\rangle = &\left[1 - \sum_{q'}^{\text{occpuied}} (\hat{U}_{\eta R_0} |\phi_{q'}\rangle)(\langle\phi_{q'}| \hat{U}^{-1}_{\eta R_0})\right] \\ &\times \left[(\hat{U}_{\eta R_0} \hat{h}_1 \hat{U}^{-1}_{\eta R_0})(\hat{U}_{\eta R_0} |\phi_p\rangle) + \sum_{o,q,r,s}^{\text{occupied}} (\hat{U}_{\eta R_0} \hat{W}^r_s \hat{U}^{-1}_{\eta R_0})(\hat{U}_{\eta R_0} |\phi_q\rangle) P^{qs}_{or} (D^{-1})^o_p\right] \\ &+ i \sum_q^{\text{occupied}} \hat{U}_{\eta R_0} |\phi_q\rangle X^q_p, \end{aligned} \tag{3.20}$$

A significant difference from the EOMs without ECS is that $\{\langle\phi_p| \hat{U}^{-1}_{\eta R_0}\}$is required, instead of $\{\langle\phi_p|\}$, to apply $\hat{Q} = 1 - \sum_{q'} |\phi_{q'}\rangle \langle\phi_{q'}|$ and evaluate matrix elements of W and X. It

is formally defined in the coordinate space as

$$(\langle\phi_p|\,\hat{U}_{\eta R_0}^{-1})\,|\boldsymbol{r}\rangle = \left[\langle\boldsymbol{r}|\left(\hat{U}_{(-\eta)R_0}\,|\phi_p\rangle\right)\right]^*. \tag{3.21}$$

It should be noticed that information of $\{\langle\phi_p|\,\hat{U}_{\eta R_0}^{-1}\}$ is available in the unscaled region but *not* available in the scaled region during the simulation, which poses a problem. Although formally one might attempt to obtain these by analytically continuing $\{\hat{U}_{\eta R_0}\,|\phi_p\rangle\}$, such a procedure turns out to be numerically unstable.

Since the scaled region is usually far from the origin, it is reasonable to assume that the scaled part of the orbital functions hardly affects the electron dynamics close to the nucleus and that the interaction between electrons residing in the scaled region is negligible. Thus, we approximately neglect $\{\langle\phi_p|\,\hat{U}_{\eta R_0}^{-1}\}$ in the scaled region wherever their information is necessary to evaluate the right-hand side (RHS) of Eq. (3.20).

Specifically, the scaled mean field operator is approximated as,

$$\begin{aligned} U_{\eta R_0}\hat{W}_s^r(\boldsymbol{r})U_{\eta R_0}^{-1} &= \hat{W}_s^r(\boldsymbol{R}(r)) \\ &\approx \int_{r'<R_0} d\boldsymbol{r}'\frac{\phi_r^*(\boldsymbol{r}')\phi_s(\boldsymbol{r}')}{|\boldsymbol{R}(r)-\boldsymbol{r}'|} \\ &\equiv \hat{W}'^r_s(\boldsymbol{R}(r)) \end{aligned} \tag{3.22}$$

Here, it should be noticed that the Coulomb force acting on a scaled-region electron ($r > R_0$) from an unscaled-region electron ($r' < R_0$) is not neglected. Hence, the effect of the ionic Coulomb potential is properly taken into account in the dynamics of departing electrons. The way to numerically evaluate the truncated scaled mean field operator $\hat{W}'^r_s(\boldsymbol{R}(r))$ is given in Subsec. 3.4.1. Then, in the second term of the RHS of Eq. (3.20),

$$(\langle\phi_{q'}|\,\hat{U}_{\eta R_0}^{-1})(\hat{U}_{\eta R_0}\hat{W}_s^r\hat{U}_{\eta R_0}^{-1})(\hat{U}_{\eta R_0}\,|\phi_q\rangle), \tag{3.23}$$

is approximated as,

$$\int_{r<R_0} d\boldsymbol{r}\phi_{q'}^*(\boldsymbol{r})\hat{W}'^r_s(\boldsymbol{R}(r))\phi_q(\boldsymbol{r}). \tag{3.24}$$

Similarly, the single-electron term of the Hamiltonian defined in Eq. (2.10) is approximated as,

$$h_{1p}^{q'} \approx \int_{r<R_0} d\boldsymbol{r}\phi_{q'}^*(\boldsymbol{r})\hat{h}(\boldsymbol{r})\phi_p(\boldsymbol{r}). \tag{3.25}$$

In order to evaluate the matrix elements $h_{2sq}^{rp} = W_{sq}^{rp}$ required to evaluate the matrix elements of X (Eqs. (2.2), (2.47) and (2.48)) and to propagate CI coefficients using Eq. (2.77), we need to evaluate the following Coulomb matrix elements,

$$W_{sq}^{rp} = \int d\boldsymbol{r}d\boldsymbol{r}'\frac{\phi_r^*(\boldsymbol{r})\phi_p^*(\boldsymbol{r}')\phi_q(\boldsymbol{r}')\phi_s(\boldsymbol{r})}{|\boldsymbol{r}-\boldsymbol{r}'|}, \tag{3.26}$$

which we approximate as, truncating the integral within the unscaled region as well as Eq. (3.24),

$$W_{sq}^{rp} \approx \int_{r<R_0} d\boldsymbol{r}\phi_p^*(\boldsymbol{r})\hat{W}'^r_s(\boldsymbol{R}(r))\phi_q(\boldsymbol{r}). \tag{3.27}$$

3.4.1 Scaled interelectronic Coulomb interaction

We describes how to numerically evaluate $\hat{W}'^r_s(\vec{R}(r))$ [Eq. (3.22)]. By using the multipole expansion of $1/|\vec{r}-\vec{r}'|$ given in (2.90),

$$\frac{1}{|\vec{r}-\vec{r}'|} = \sum_{l=0}^{\infty}\sum_{m=-l}^{l}\frac{4\pi}{2l+1}\frac{r_<^l}{r_>^{l+1}}Y_{lm}^*(\theta',\phi')Y_{lm}(\theta,\phi),$$

where $r_>(r_<)$ is the greater (smaller) of r and r', the truncated mean field operator $\hat{W}'^r_s(\vec{r})$ can be expanded as,

$$\hat{W}'^r_s(\vec{r}) = \sum_{lm}\frac{(V'^r_s)_{lm}(r)}{r}Y_{lm}(\theta,\phi), \tag{3.28}$$

where $(V'^r_s)_{lm}(r)$ is given by,

$$(V'^r_s)_{lm}(r) = \frac{4\pi}{2l+1}r\int_0^{R_0}dr'\frac{r_<^l}{r_>^{l+1}}r'(\rho_s^r)_{lm}(r'), \tag{3.29}$$

with,

$$(\rho_s^r)_{lm}(r') = r'\int d\Omega' Y_{lm}^*(\theta',\phi')\phi_r^*(\boldsymbol{r}')\phi_s(\boldsymbol{r}'). \tag{3.30}$$

In the unscaled region ($r < R_0$), we obtain $(V'^r_s)_{lm}(r)$ by solving Poisson equation [52],

$$\left(\frac{d^2}{dr^2}-\frac{l(l+1)}{r^2}\right)((V'^r_s)_{lm}(r)) = -4\pi(\rho_s^r)_{lm}(r). \tag{3.31}$$

In the scaled region ($r > R_0$), on the other hand, $(V'^r_s)_{lm}(r)$ is simplified into,

$$(V'^r_s)_{lm}(r) = \frac{4\pi}{2l+1}\frac{1}{r^l}\int_0^{R_0}dr'r'^{l+1}(\rho_s^r)_{lm}(r'), \tag{3.32}$$

which can be evaluated by numerical integration. Hence $\hat{W}'^r_s(\vec{R}(r))$ is expressed as

$$\hat{W}'^r_s(\vec{R}(r)) = \sum_{lm}\frac{4\pi}{2l+1}\frac{1}{R(r)^{l+1}}Y_{lm}(\theta,\phi)\int_0^{R_0}dr'r'^{l+1}(\rho_s^r)_{lm}(r'). \tag{3.33}$$

Table 3.1: Absorbing boundaries tested for Be. n_{ua} (n_{ab}) denotes the number of grid points in the non-absorption (absorption) region, and L_{a} the radial thickness of the absorption region. The radius R_{max} of the whole simulation region is given by $R_{\mathrm{mask}} + L_{\mathrm{a}}$ or $R_0 + L_{\mathrm{a}}$.

	absorber	R_{mask} or R_0	n_{ua}	L_{a}	n_{ab}
A	mask	320	1600	80	400
B	irECS	40	200	∞	40
C	irECS	52	260	∞	40
D	mask	52	260	8	40
E	mask	88	440	56	280

3.5 Numerical examples

In this section, we assess the performance of the implementation of irECS to the TD-ORMAS method described in the previous sections, simulating many-electron atoms in an intense near-infrared laser pulse. We assume a laser field linearly polarized in the z direction of the following form:

$$E(t) = \sqrt{I_0} \sin \omega t \sin^2 \left(\pi \frac{t}{NT} \right), \ (0 \leq t \leq NT), \tag{3.34}$$

where I_0 is a peak intensity, T is a period at the central frequency $\omega = 2\pi/T$ and N is the total number of optical cycles. We gauge the performance of simulations with irECS against nominally "exact" results converged with respect to a simulation box size and obtained with the mask function boundary. In the latter, orbital functions are multiplied by a mask function,

$$M(\vec{r}) = \begin{cases} 1 & \text{for } |\vec{r}| < R_{\mathrm{mask}} \\ \cos^{\frac{1}{4}} \left(\dfrac{\pi}{2} \dfrac{|\vec{r}| - R_{\mathrm{mask}}}{R_{\mathrm{max}} - R_{\mathrm{mask}}} \right) & \text{for } |\vec{r}| \geq R_{\mathrm{mask}}, \end{cases} \tag{3.35}$$

after each time step, where R_{mask} and R_{max} denote the absorption boundary and the simulation box radius, respectively.

3.5.1 Beryllium

We first simulate a Beryllium atom subject to a laser field with $I_0 = 3.0 \times 10^{14}$ W/cm^2, $\lambda = 800$nm (the quiver radius is 28.5 a.u.), $N = 5$, and $(n_{\mathrm{a}}, n_{\mathrm{dc}}, n_{\mathrm{fc}}) = (4, 0, 1)$. Each orbital function is expanded with 47 spherical harmonics and discretized with radial finite elements 4 a.u. long except for the last irECS element. Each finite element, including the irECS element, has 21 grid points. The scaling angle η is set to be 15° and the dumping factor *alpha* of irECS is set to be 0.5. Five different conditions used for absorption boundaries are listed on Table 3.1.

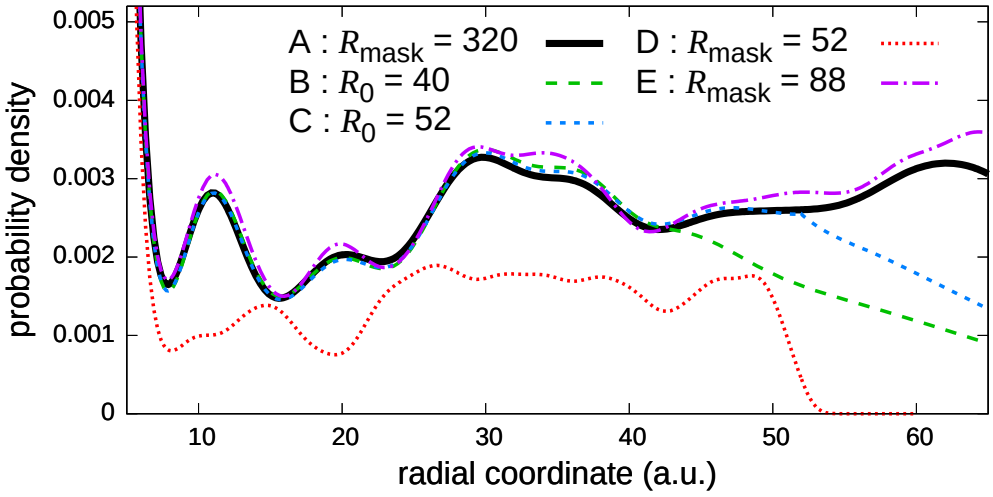

Figure 3.1: Electron radial distribution function $\rho(r)$ after the laser pulse for the case of Be exposed to a laser pulse with 800 nm wavelength and 3.0×10^{14} W/cm^2 peak intensity, calculated with different absorbing boundaries listed in Table 3.1.

Figure 3.1 compares the electron radial distribution functions defined as

$$\rho(r) = Nr^2 \int d\sigma d\Omega d\vec{x}_2 d\vec{x}_3 \cdots \vec{x}_n \left|\Psi(\vec{x}, \vec{x}_2, \cdots, \vec{x}_n)\right|^2, \tag{3.36}$$

after the pulse, calculated with different absorption boundaries. The irECS delivers much better results (B and C) than the mask function (D). Nevertheless, the irECS results slightly deviate from the exact solution (A) even if the scaling radius is almost twice the quiver radius. In the present case, the Be atom is nearly totally ionized, and double ionization amounts to 50 % (Fig. 3.2). Hence, the deviation may be attributed to the neglect of the Coulomb interaction in and from the scaled region and/or the loss of information on the wave function in the scaled region.

In order to reveal the effect of the latter, we have performed a simulation with a sufficiently large domain with the mask function ($R_{\mathrm{mask}} = 320$ a.u. and $R_{\mathrm{max}} = 400$ a.u.) but with the integrals truncated at $r = 28$ a.u., as described in Sec. 3.4. We compare the result with the exact one and that from irECS with $R_0 = 28$ a.u. in Fig. 3.3 . The "truncated" and irECS results overlap each other and slightly deviate from the exact solution, which indicates that the slight deviations in Figs. 3.1 and 3.3 stem from the neglect of the Coulomb interaction in and from the scaled region. One may be surprised that the loss of information on orbital functions at the absorption boundary hardly affects simulation results within the absorption radius. This may be because the TD-ORMAS (and MCTHDF, TD-CASSCF) equations of motion assume the orthonormality of the true (, i.e., unscaled) orbital functions $\{|\psi_p\rangle\}$, even though their numerically propagated portions $\{\hat{U}_{\eta R_0}|\psi_p\rangle\}$ are not orthonormal in general. Consequently, information on the absorbed part, though its explicit form is unknown, is partially retained, which enables accurate simulations. It should also be noticed that, since we construct the total wave

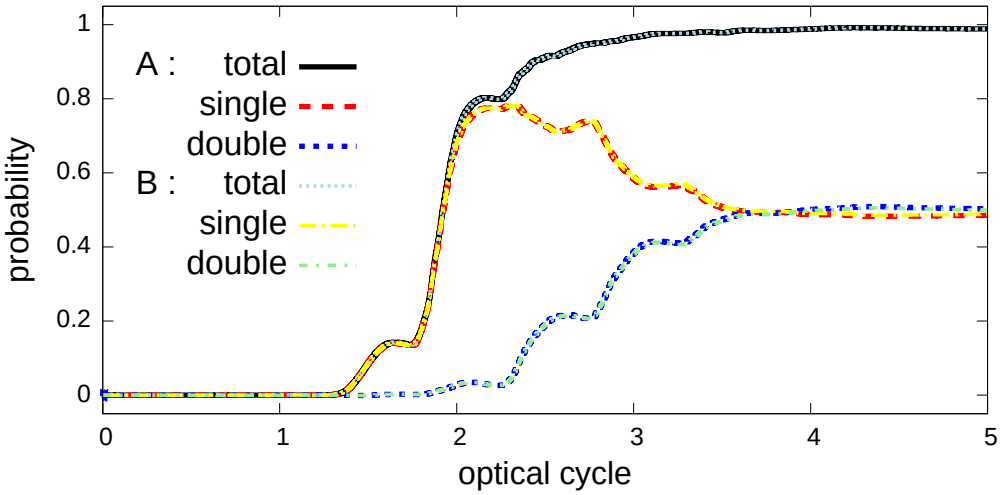

Figure 3.2: Time evolution of single, double, and total ionization probabilities of Be exposed to a laser pulse with 800 nm wavelength and 3.0×10^{14} W/cm^2 peak intensity. For convenience, we define single (double) ionization probability as that of finding one (two) electron(s) outside the 20 a.u. radius. The total ionization probability is calculated as their sum.

function based on single-electron orbitals, even if one or more electrons are absorbed, we can continue to follow the associated dynamics of the other unabsorbed electrons. This is in great contrast to the time-dependent close-coupling simulations [62–65], where, if one electron reaches the absorption boundary, the corresponding part of the total wave function is completely lost.

In spite of the small discrepancy in Fig. 3.1, irECS gives the time evolution of single/double ionization (Fig. 3.2) and the high-harmonic spectrum (Fig. 3.4), which is calculated as the magnitude squared of the Fourier transform of dipole acceleration, in excellent agreement with the exact results. In particular, the mask function with $R_{\mathrm{mask}} = 52$ fails to reproduce, the sharp drop of the harmonic spectral intensity after the cutoff because of unphysical reflection. It is remarkable that the neglect of the Coulomb interaction in and from the scaled region is a good approximation and that irECS works excellently even under such massive double ionization. We have reduced computational costs by 66% compared with the best case of the mask function (E) to obtain a converged high harmonic spectrum (B).

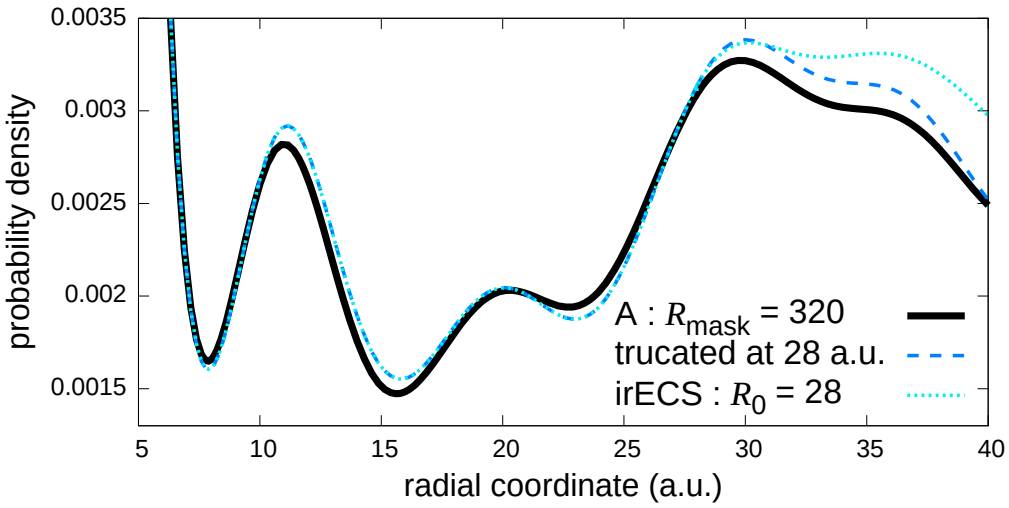

Figure 3.3: Electron radial distribution function $\rho(r)$ after the laser pulse for the case of Be exposed to a laser pulse with 800 nm wavelength and 3.0×10^{14} W/cm^2 peak intensity. We compare the results using the mask boundary ($R_{\text{mask}} = 320\,\text{a.u.}$) without (thick solid) and with (thin dashed) the integral truncations at 28 a.u., as described in Sec. 3.4, and the result using the irECS with $R_0 = 28\,\text{a.u.}$ (dotted).

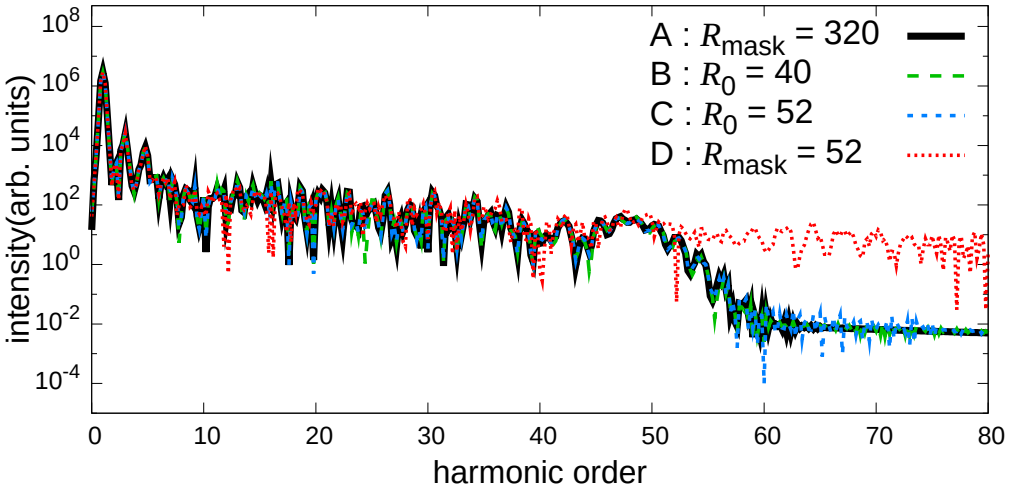

Figure 3.4: High harmonic spectra from Be exposed to a laser pulse with 800 nm wavelength and 3.0×10^{14} W/cm^2 peak intensity, calculated with different absorbing boundaries A-D listed in Table 3.1.

Table 3.2: Absorbing boundaries tested for Ne.

	absorber	R_{mask} or R_0	n_{ua}	L_{a}	n_{ab}
A	mask	256	1280	64	320
B	irECS	60	300	∞	60
C	mask	60	300	12	60

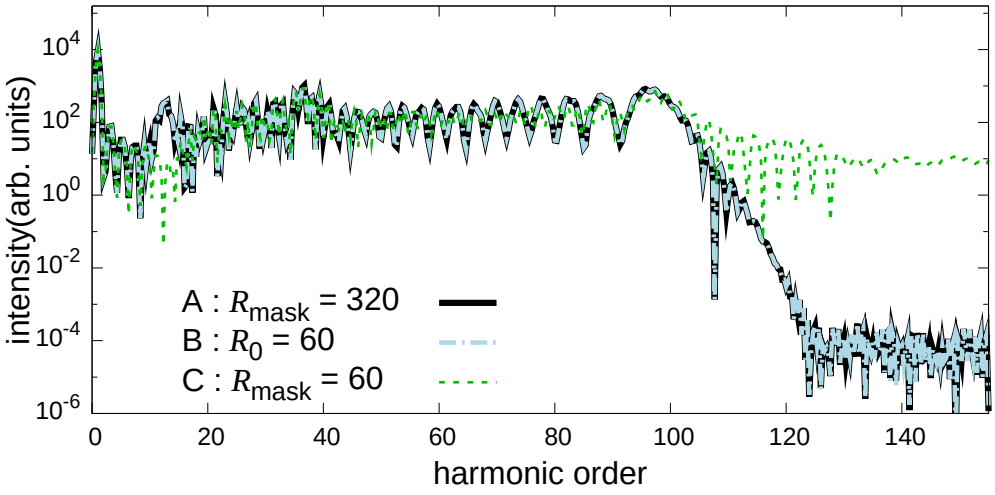

Figure 3.5: High harmonic spectra from Ne exposed to a laser pulse with 800 nm wavelength and 8.0×10^{14} W/cm^2 peak intensity, calculated with different absorbing boundaries listed in Table 3.2.

3.5.2 Neon

Finally, as a typical target atom used for attosecond-pulse generation, we simulate HHG from a Neon atom subject to a laser pulse with $I_0 = 8.0 \times 10^{14}$ W/cm^2, $\lambda = 800\,\mathrm{nm}$, and $N = 3$. We use 8 active orbitals and 1 dynamical core, i.e., $(n_{\mathrm{a}}, n_{\mathrm{dc}}, n_{\mathrm{fc}}) = (8, 1, 0)$. Each orbital function is expanded with 47 spherical harmonics and discretized with radial finite elements 4 a.u. long except for the last irECS element. Each finite element, including the irECS element, has 21 grid points. The scaling angle η is fixed to 15° and the dumping factor α of irECS is set to be 0.5. Three different conditions used for absorption boundaries are listed in Table 3.2.

If we use the same radius $R_0, R_{\mathrm{mask}} = 60\,\mathrm{a.u.}$ of the non-absorbing region and number $n_{\mathrm{ab}} = 60$ of grid points in the absorption region, the irECS result (B) perfectly overlaps with the "exact" result (C) obtained with a large simulation box ($R_{\mathrm{mask}} = 256\,\mathrm{a.u.}$), while the mask boundary (C) fails (Fig. 3.5). As in the case of He, the ionization probability (about 4 %) is relatively small due to the large ionization potential (21.6 eV) of a Ne atom, so that the truncation of integrals introduced to apply ECS to the TD-CASSCF method leads to almost no error. The computational cost of the irECS simulation B is reduced by 80% compared with case A.

Chapter 4

Application of the tSURFF method to the TD-ORMAS method

The photoelectron momentum amplitude (PMA) $a(\boldsymbol{k}, t)$ for momentum $\boldsymbol{k}$ and photoelectron energy spectra (PES),

$$\rho(E, t) = \int d\Omega |a(\boldsymbol{k}, t)|^2 |\boldsymbol{k}|^2 \quad (E = |\boldsymbol{k}|^2/2), \tag{4.1}$$

can in principle be approximately calculated by projecting the outgoing wave packet residing outside a given radius R_s onto the plane wave $p_{\boldsymbol{k}}(\boldsymbol{r}) = (2\pi)^{-3/2} \exp(i\boldsymbol{k} \cdot \boldsymbol{r})$ at a time t sufficiently after the pulse. Then, for example in single-electron systems, PMA is given by,

$$\begin{aligned} a(\boldsymbol{k}, t) &= \langle p_{\boldsymbol{k}}(\boldsymbol{r}, t) | \hat{\theta}(R_s) | \Psi(t) \rangle \,, \\ &\equiv \int p^*_{\boldsymbol{k}}(\boldsymbol{r}, t) \theta(|\boldsymbol{r}| - R_s) \Psi(\boldsymbol{r}, t) d^3\boldsymbol{r}, \\ &= \int_{r > R_s} p^*_{\boldsymbol{k}}(\boldsymbol{r}, t) \Psi(\boldsymbol{r}, t) d^3\boldsymbol{r}. \end{aligned} \tag{4.2}$$

where $\theta(x)$ denotes the Heaviside function to extract photoelectron wave packets. However, to use this approach, the complete wave function without being absorbed is required, which leads to a prohibitive computational cost. If the system has low energy photoelectrons or a laser pulse with a long time duration is irradiated, the simulation duration gets longer and the required size of the simulation box can reach a few thousand atomic units. To overcome this problem, the time-dependent surface flux (tSURFF) method developed by Tao and Scrinzi [47] converts the spatial integral of a wave function in Eq. (4.2) into time integral of a surface flux of the wave function.

In this chapter, we combine this tSURFF method with the TD-ORMAS method to extract photoelectron energy spectra from multielectron systems [66]. Under a physically reasonable assumption that the nuclear potential and interelectronic Coulomb interaction are negligible for photoelectron dynamics in the region distant from the nuclei, we apply the tSURFF method and derive the equations of motion for the momentum amplitudes of each orbital. As results of our application, we achieve highly accurate calculations of angle-resolved PES with considerably reduced computational costs.

This chapter is organized as follows. We review the tSURFF method for single-electron systems in Sec. 4.1. In Sec. 4.2, we describe our theoretical application and numerical implementation of tSURFF to the TD-ORMAS method. Numerical results are presented in Sec. 4.3.

4.1 the tSURFF method for single-electron systems

In this section, we briefly review the tSURFF method [47] for single-electron systems governed by TDSE,

$$i\frac{\partial}{\partial t}\Psi(\boldsymbol{r},t) = h_1(t)\Psi(\boldsymbol{r},t), \tag{4.3}$$

$$h_1(t) = -\frac{1}{2}\nabla^2 + V(\boldsymbol{r}) - i\boldsymbol{A}(t)\cdot\nabla, \tag{4.4}$$

where $V(\boldsymbol{r})$ denotes the nuclear potential.

The tSURFF method calculates PES by time integration of the wave function surface flux, based on an assumption that the nuclear potential does not affect the time evolution of the distant photoelectron wave packet. Under this assumption, the Volkov wave functions and photoelectron wave packets in the region $|\boldsymbol{r}| > R_\mathrm{s}$ are evolved by the same nuclear-potential-free Hamiltonian

$$h_\mathrm{s} = -\frac{1}{2}\nabla^2 - i\boldsymbol{A}(t)\cdot\nabla. \tag{4.5}$$

By taking time derivative of Eq. (4.2), we obtain the EOM of the momentum amplitude,

$$-i\frac{\partial}{\partial t}a(\boldsymbol{k},t) = \langle\chi_{\boldsymbol{k}}(t)|[h_\mathrm{s},\theta(R_\mathrm{s})]|\Psi(t)\rangle\,, \tag{4.6}$$

where $\chi_{\boldsymbol{k}}(t)$ denotes the Volkov wave function, which is a momentum eigenfunction of the Hamiltonian h_s. As shown in Ref. [47], since all the terms appearing in the commutator $[h_\mathrm{s},\theta(R_\mathrm{s})]$ contain delta functions $\delta(r-R_\mathrm{s})$ [see Eq. (4.18) below], wave functions and their spatial derivative only on the surface $|\boldsymbol{r}| = R_\mathrm{s}$ are required to solve Eq. (4.6). Hence, it is no longer needed to keep the whole wave function and allowed to use an absorbing boundary, which leads to a significant computational cost reduction.

4.2 Application of the tSURFF method to the TD-ORMAS simulations

4.2.1 Photoelectron reduced density matrix

To obtain PES in multielectron systems described by the multiconfiguration expansion Eq. (2.1), we define the photoelectron reduced density matrix (PRDM). Since our def-

inition of ionization is based on the spatial domain $|\boldsymbol{r}| > R_s$, the single particle reduced density matrix of a photoelectron in the coordinate space can be defined as,

$$P(\boldsymbol{r},\boldsymbol{r'}) = \sum_{pq} \langle \boldsymbol{r}| \, \theta(R_s) \, |\phi_p\rangle \, D^p_q \, \langle \phi_q| \, \theta(R_s) \, |\boldsymbol{r'}\rangle \, . \tag{4.7}$$

In the momentum space, its elements are given by,

$$\begin{aligned} \tilde{P}(\boldsymbol{k},\boldsymbol{k'}) &= \int d\boldsymbol{r} d\boldsymbol{r'} \, \langle \chi_{\boldsymbol{k}}(t)|\boldsymbol{r'}\rangle \, P(\boldsymbol{r},\boldsymbol{r'}) \, \langle \boldsymbol{r}|\chi_{\boldsymbol{k}}(t)\rangle \\ &= \sum_{pq} \langle \chi_{\boldsymbol{k}}(t)| \, \theta(R_s) \, |\phi_p\rangle \, D^p_q \, \langle \phi_q| \, \theta(R_s) \, |\chi_{\boldsymbol{k'}}(t)\rangle \, . \end{aligned} \tag{4.8}$$

The diagonal part $\tilde{P}(\boldsymbol{k},\boldsymbol{k})$ is interpreted as photoelectron momentum distribution, and, then, PES is given by,

$$\rho(E) = \int d\Omega \tilde{P}(\boldsymbol{k},\boldsymbol{k})|\boldsymbol{k}|^2. \tag{4.9}$$

A similar definition of the PRDM as Eq. (4.8) and the direct projection onto scattering states were used to compute photoelectron spectrum in Ref. [67].

4.2.2 EOMs of momentum amplitudes of orbitals

In this subsection, we derive the EOM of the momentum amplitude of orbital p,

$$a_p(\boldsymbol{k},t) = \langle \chi_{\boldsymbol{k}}(t)|\theta(R_\mathrm{s})|\phi_p\rangle \, , \tag{4.10}$$

which appears in Eq. (4.8). We assume that the nuclear potentials are negligible for photoelectrons as in the single-electron case and additionally that the interelectronic Coulomb interaction does not affect the dynamics of photoelectrons in the region beyond the radius R_s. Then, the orbital EOM Eq. (2.57) can be approximated as,

$$\begin{aligned} i\,|\dot{\phi_p}\rangle =& (\hat{h}_\mathrm{s} + \hat{V}_\mathrm{N})\,|\phi_p\rangle + \sum_{o,q,r,s}^{\text{occupied}} \hat{W}^r_s \, |\phi_q\rangle \, P^{qs}_{or} (D^{-1})^o_p \\ &- \sum_{q'} |\phi_{q'}\rangle \left[\hat{h}_\mathrm{s}{}^{q'}_p + \sum_{o,q,r,s}^{\text{occupied}} \hat{W}^{q'r}_{qs} P^{qs}_{or} (D^{-1})^o_p + i X^{q'}_p \right] \qquad (4.11) \\ \simeq& \hat{h}_\mathrm{s}\,|\phi_p\rangle - \sum_{q'} |\phi_{q'}\rangle \left[\hat{h}_1{}^{q'}_p + \sum_{o,q,r,s}^{\text{occupied}} \hat{W}^{q'r}_{qs} P^{qs}_{or} (D^{-1})^o_p + i X^{q'}_p \right] . \qquad (4.12) \end{aligned}$$

It should be noticed that the nuclear and mean field potentials in the third term of Eq. (4.11) remain after the approximation (Eq (4.12)), since they include the effect of the potentials inside R_s (see also Fig. 4.1).

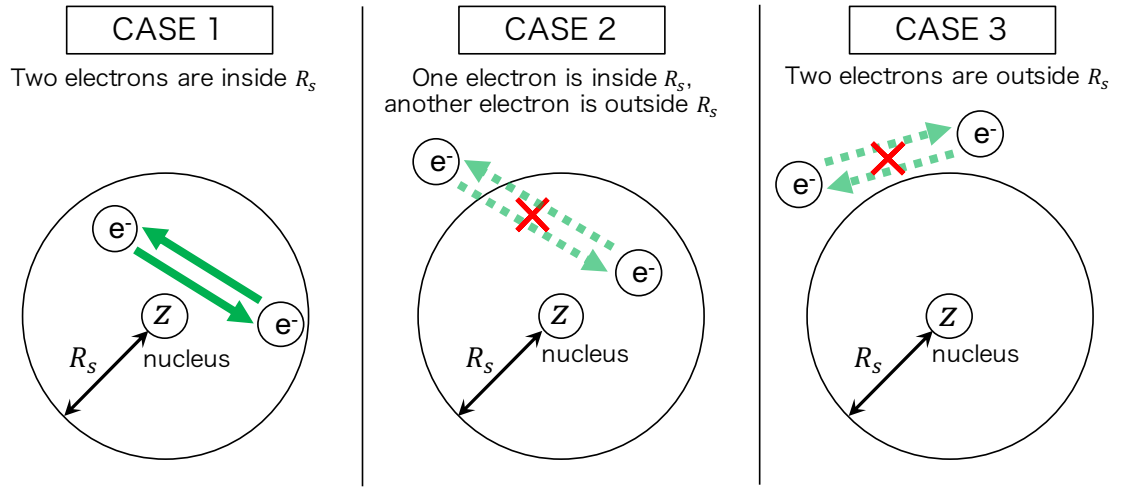

Figure 4.1: A schematic illustration of the approximation of interelectronic Coulomb interaction in the application of the tSURFF method to the TD-ORMAS method. In the cases that one electron is inside R_s and another electron is outside R_s, or two electron are outside R_s, the Coulomb interaction is neglected. However, in the case that two electrons are inside R_s, the interelectronic Coulomb interaction is exactly considered.

By differentiating $a_p(\boldsymbol{k})$ in time, the EOMs of $a_p(\boldsymbol{k})$ is obtained as

$$\frac{\partial}{\partial t}a_p(\boldsymbol{k},t) = i\langle\chi_{\boldsymbol{k}}(t)|[h_s,\theta(R_s)]|\phi_p(t)\rangle + i\sum_q a_q(\boldsymbol{k},t)R_p^q, \tag{4.13}$$

where for the simplicity of equations we define a matrix R as

$$R_p^{q'} = \hat{h}_{1p}^{\ q'} + \sum_{o,q,r,s}^{\text{occupied}} \hat{W}_{qs}^{q'r}P_{or}^{qs}(D^{-1})_p^o + iX_p^{q'}. \tag{4.14}$$

Note the second term in Eq. (4.13) represents a significant difference from the single-electron case [Eq. (4.6)]. As we stated above, this term includes the effect of nuclear and interelectronic potentials inside R_s and is not negligible even when we consider photoelectrons outside R_s; for example, the phase variation due to the energy of the ionic core is reflected in photoelectron momentum spectra through this term.

It may not be a priori obvious if the Coulomb interaction between electrons in the outer region is negligible. A numerical validation of this approximation will be given in Sec. 4.3.

4.2.3 Implementation

In this subsection, we describe the implementation of the tSURFF method to TD-ORMAS simulations. We consider multielectron atoms subject to a laser pulse linearly polarized in the z direction. The orbitals are discretized with spherical finite-element discrete-variable-

representation (FEDVR) basis functions as shown in Eq. (4.15),

$$\phi_p(r,\theta,\phi) = \sum_{klm} c^p_{klm} \frac{f_k(r)}{r} Y_{lm}(\theta,\phi). \tag{4.15}$$

On the other hand, we discretize the orbital momentum amplitudes with grid points in the spherical coordinates, where the Volkov wave function for a momentum $\boldsymbol{k} = (k, \theta_k, \psi_k)$ is given by,

$$\begin{aligned}\chi_{\boldsymbol{k}}(\boldsymbol{r},t) = &\frac{\exp(-i\Lambda(\boldsymbol{k},t))}{(2\pi)^{3/2}} \\ &\times \sum_{lm} 4\pi i^l Y^*_{lm}(\theta_k,\psi_k) j_l(kr) Y_{lm}(\theta,\psi),\end{aligned} \tag{4.16}$$

with $j_l(kr)$ being the spherical Bessel function of the first kind and $\Lambda(\boldsymbol{k},t)$ the Volkov phase given by,

$$\Lambda(\boldsymbol{k},t) = \int_0^t \frac{1}{2}[\boldsymbol{k} - \boldsymbol{A}(\tau)]^2 d\tau. \tag{4.17}$$

The commutator in Eq. (4.6) can be rewritten as,

$$\begin{aligned}[h_s, \theta(R_s)] = &-\frac{1}{2}\left[\frac{\partial}{\partial r}\delta(r-R_s) + \delta(r-R_s)\frac{\partial}{\partial r}\right] \\ &- \frac{\delta(r-R_s)}{r} + iA_z(t)\cos(\theta)\delta(r-R_s),\end{aligned} \tag{4.18}$$

with z component $A_z(t)$ of the vector potential $\boldsymbol{A}(t)$. Using Eqs. (4.16) and (4.17) and introducing $g^p_{lm}(r) = \sum_k c^p_{klm} f_k(r)/r$, we can decompose the first term of Eq. (4.13) into,

$$\begin{aligned}\langle\chi_{\boldsymbol{k}}(t)|[h_s,\theta(R_s)]|\phi_p(t)\rangle = &\frac{\exp i\Lambda(\boldsymbol{k},t)}{(2\pi)^{3/2}} 4\pi \sum_{lm}(-i)^l \times \\ &\Big[Y_{lm}(\theta_k,\psi_k)\frac{R_s^2}{2}\{j_l^{*\prime}(kR_s) g^p_{lm}(R_s) - j_l^*(kR_s) g^{p\,\prime}_{lm}(R_s)\} \\ &+ iA_z(t)\sum_{l'm'}(-i)^{l'm'} Y_{l'm'}(\theta_k,\psi_k)) R_s^2 j_l^*(kR_s) g^p_{lm}(R_s) \alpha^{l'm'}lm\Big],\end{aligned} \tag{4.19}$$

where $j_l^{*\prime}(r)$ and $g_l^{p\prime}(r)$ denote the radial derivative of $j_l^*(r)$ and $g_l^p(r)$, respectively. $\alpha^{l'm'}_{lm}$ given in Eq. (2.85) denotes $\int d\Omega Y^*_{l'm'}(\theta,\phi) cos\theta Y_{lm}(\theta,\phi)$. For the second term in Eq. (4.13), since the matrix R is evaluated during the orbital propagation [Eq. (2.57)], we can reuse it.

We integrate Eq. (4.13) with the first order exponential integrator [54] by treating Eq. (4.13) as simultaneous inhomogeneous linear differential equations. The evolution of a vector $\boldsymbol{a}(\boldsymbol{k},t) \equiv \{a_p(\boldsymbol{k},t)\}$ from the time t to $t+\Delta t$ is described as

$$\boldsymbol{a}(\boldsymbol{k},t+\Delta t) = \boldsymbol{a}(\boldsymbol{k},t)\exp[i\Delta t R(t)] + \boldsymbol{S}(t)\frac{\exp[i\Delta t R(t)] - 1}{R(t)}, \tag{4.20}$$

where the vector $\boldsymbol{S}(t) = \{S_p(t)\}$ are defined as,

$$S_p(t) = \langle \chi_{\boldsymbol{k}}(t) | [h_s, \theta(R_s)] | \phi_p(t) \rangle \,. \tag{4.21}$$

We compute $\exp[i\Delta t R(t)]$ by directly diagonalizing $R(t)$ at every time step, which is not demanding since the size of $R(t)$ is $[N_{\mathrm{orb}} \times N_{\mathrm{orb}}]$ and the number of orbitals N_{orb} usually falls within the range from a several to several tens.

4.3 Numerical results

In this section, we present numerical applications of the implementation of tSURFF to the TD-MCSCF method described in the previous section. The electric field of the laser pulse is assumed to have the following shape for simulations of a Ne atom (Sec. 4.3.1) and a Be atom (Sec. 4.3.2):

$$E(t) = \sqrt{I_0} \sin^2\left(\pi \frac{t}{N_{\mathrm{opt}} T}\right) \sin \omega t, \ 0 \le t \le N_{\mathrm{opt}} T, \tag{4.22}$$

and for Ar atom (Sec. 4.3.3):

$$E(t) = e(t) \sin \omega t, \tag{4.23}$$

$$e(t) = \begin{cases} \sqrt{I_0} \dfrac{t}{2T}, & 0 < t \le 2T \\ \sqrt{I_0}, & 2T < t \le (N_{\mathrm{opt}} - 2)T \\ \sqrt{I_0} \dfrac{N_{\mathrm{opt}} T - t}{2T}, & (N_{\mathrm{opt}} - 2)T < t \le N_{\mathrm{opt}} T \end{cases}, \tag{4.24}$$

where I_0 is a peak intensity, T is a period at the central frequency $\omega = 2\pi/T$, and N_{opt} is the total number of optical cycles.

4.3.1 Neon

We first calculate the PES of a neon atom subject to an attosecond pulse with a peak intensity of $2.5 \times 10^{12} \mathrm{W/cm^2}$, a wavelength of 12.398 nm corresponding to 100 eV photon energy, and $N_{\mathrm{opt}} = 16$. The results by tSURFF and direct projection on plane waves are compared. As an absorbing boundary, we use irECS with a scaling radius R_0 of 40 a.u for tSURFF and 400 a.u for direct projection. The latter is large enough to hold the departing wave packet from two-photon ionization. $R_s = 40\,\mathrm{a.u.}$ for tSURFF, and the wave packet outside this radius is used for projection.

We do TD-CASSCF simulations with 3 kinds of orbital classifications $(n_{\mathrm{fc}}, n_{\mathrm{dc}}, n_{\mathrm{a}}) = (0,0,5)$, $(0,0,9)$, and $(1,0,8)$, where n_{fc}, n_{dc}, and n_{a} are the number of frozen-core, dynamical-core, and active orbitals, respectively. Note that the first and second correspond to the time-dependent Hartree-Fock (TDHF) [68] and MCTDHF methods, respectively.

The results are shown in Fig. 4.2. We see single photon ionization peaks (around 30 - 90 eV) and two photon above threshold ionization (ATI) peaks (around 130 eV - 190eV) from $2s$ and $2p$ orbitals. The agreement between the results by tSURFF and direct projection is excellent. In Fig. 4.3, we compare the photoelectron angular distributions calculated with the tSURFF method and direct projection. Again, we find excellent agreement. These show the validity of the neglect of the electron-electron and nucleus-electron Coulomb interaction beyond R_s assumed in the application of the tSURFF method to the TD-ORMAS method.

While the single-photon ionization peaks from $2s$ and $2p$ orbitals are expected to be at 51.5 and 78.4 eV, respectively, based on the experimental values of the binding energies [69], the peaks in the calculated spectra are located at 47.5 and 76.7 eV in Fig. 4.2(a), 48.9 and 77.9 eV in (b), and 48.7 and 77.9 eV in (c), coming closer to the experimental positions with increasing number of orbitals. Otherwise, TDHF gives results similar to the MCTDHF and TD-CASSCF ones for this process.

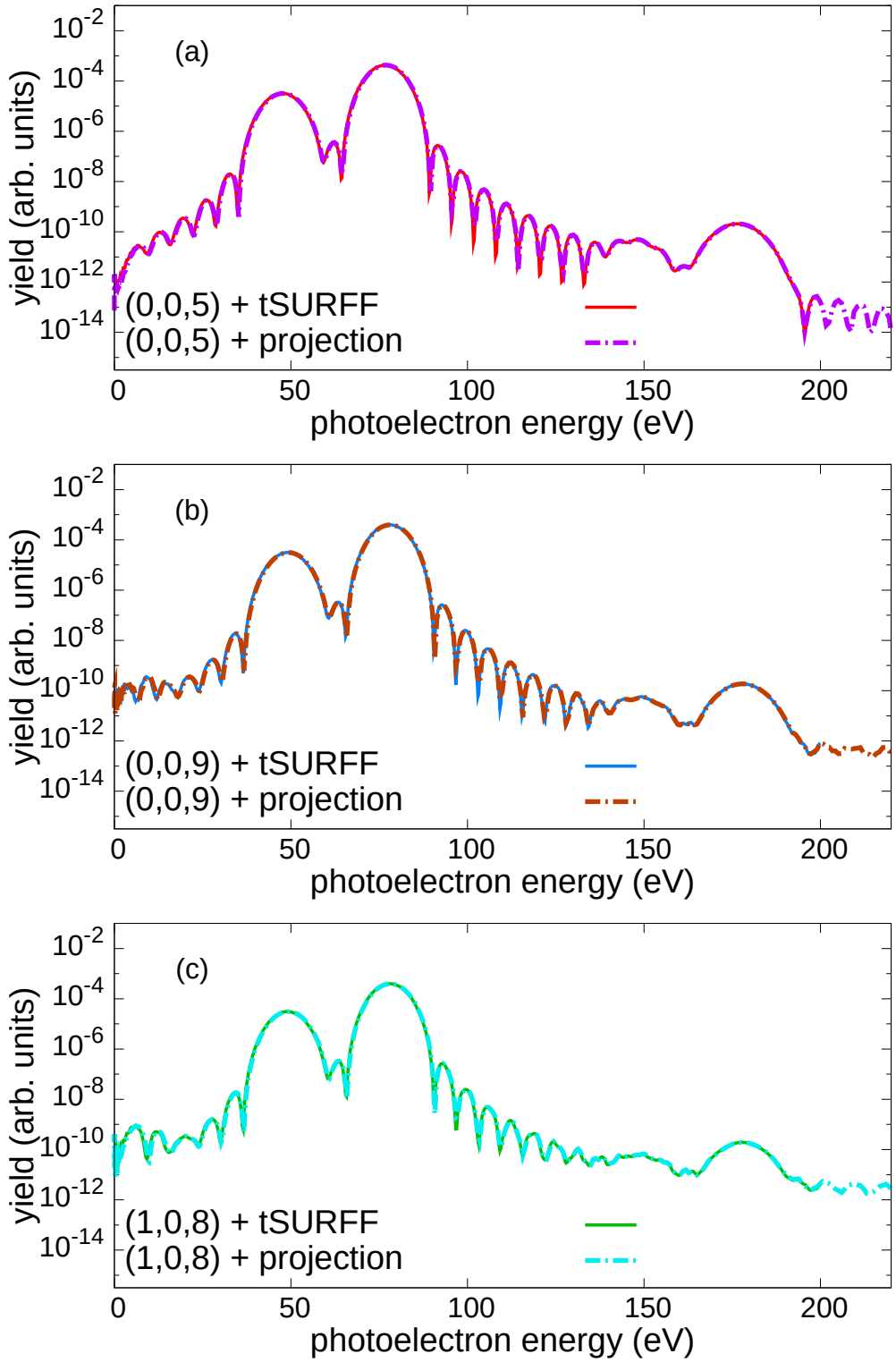

Figure 4.2: Photoelectron energy spectra of a Ne atom subject to an attosecond pulse with 100eV photon energy calculated with orbital classification (a) $(n_{\mathrm{fc}}, n_{\mathrm{dc}}, n_{\mathrm{a}}) = (0,0,5)$ (TDHF), (b) $(0,0,9)$ (MCTDHF), and (c) $(1,0,8)$ (TD-CASSCF). The results by tSURFF and direct projection are compared.

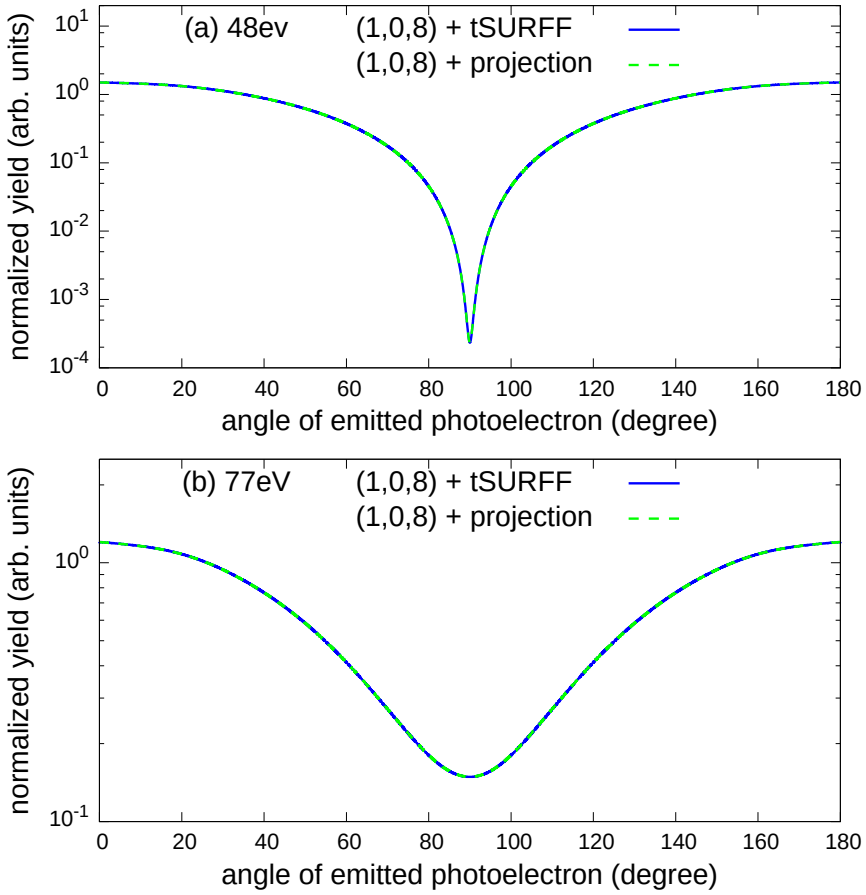

Figure 4.3: Photoelectron angular distribution from a Ne atom at (a) 48 eV and (b) 77 eV, calculated with orbital classification $(n_{\mathrm{fc}}, n_{\mathrm{dc}}, n_{\mathrm{a}}) = (1, 0, 8)$. The results extracted with the tSURFF method and direct projection are compared. The angle-integrated yield is normalized to unity.

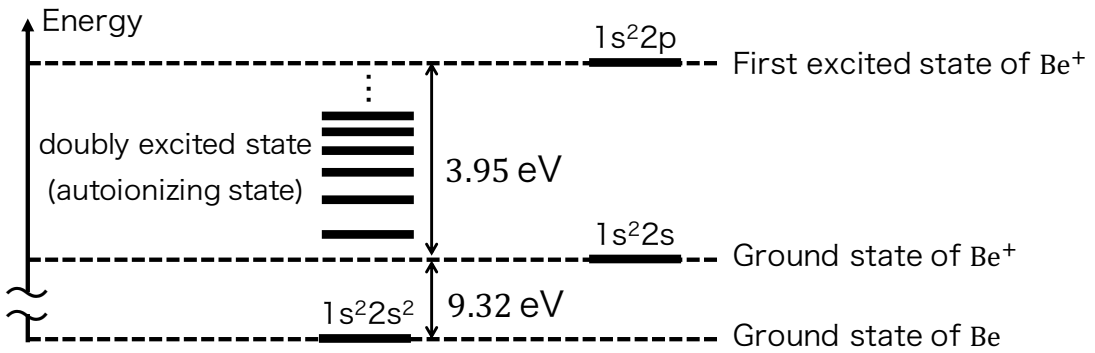

Figure 4.4: Energy level diagram of a Be atom. There are many doubly excited states leading to autoionization between the energy levels of the Be^+ ground state and the first excited state.

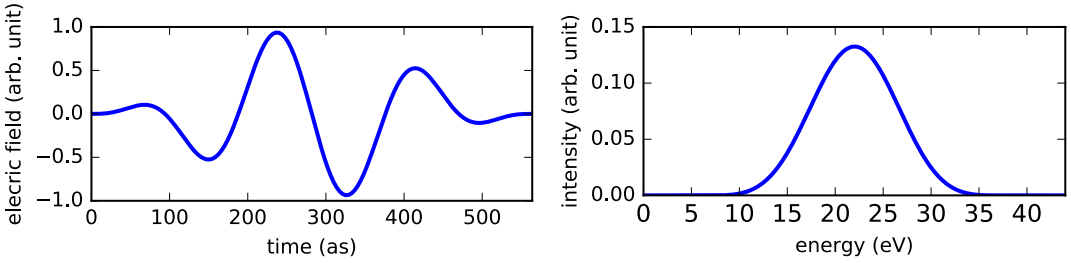

Figure 4.5: Temporal shape and intensity spectrum of the laser pulse considered for the case of Be.

4.3.2 Beryllium

In this subsection, we compute one photon ionization cross section of a Be atom including Fano resonance with the TD-CASSCF method. A Be atom has multiple doubly excited states above the ground state of Be^+, which lead to autoionization (Fig. 4.4) [70–72]. Photoelectron wave packets generated by direct ionization and autoionization can interfere with each other, and photoionization cross section show a complicated resonance profile. The shape of the profile was first theoretically described by U. Fano [73], and thus this phenomenon is called Fano resonance.

In order to observe the Fano resonance of a Be atom, we simulate a Be atom subject to a laser pulse with a peak intensity of $1.0 \times 10^{14} \mathrm{W/cm^2}$, a wavelength of 56.31 nm corresponding to about 22 eV photon energy, and $N_{\mathrm{opt}} = 3$. The temporal shape and energy spectrum of the pulse are shown in Fig. 4.5. In the TD-CASSCF method, we use 4 active orbitals and 1 frozen core, i.e., $(n_{\mathrm{a}}, n_{\mathrm{dc}}, n_{\mathrm{fc}}) = (4, 0, 1)$. irECS with a scaling radius R_0 of 88 a.u is used for an absorbing boundary. Photoelectron energy spectra are extracted by the tSURFF method with $R_{\mathrm{s}} = 88\,\mathrm{a.u.}$ and the cross section $\sigma(E)$ is calculated

by dividing photoelectron energy spectra $\rho(E)$ by the laser pulse energy spectra $I(E)$,

$$\sigma(E) = \frac{\rho(E)}{I(E)}. \tag{4.25}$$

Figure 4.6(a) presents one photon ionization cross section of a Beryllium atom with respect to the total time of propagation, and Fig 4.6(b) presents an experimental result measured with synchrotron radiation [74]. In Fig 4.6(a), we see that the doubly excited states decay over time and a fine resonant structure gradually appears. The overall structures of the cross sections obtained from our simulation and the experiment show a good agreement. This indicates that we can correctly simulate the autoionization process of doubly excited states, where electronic correlation plays an essential role. Since the ionization potential in the TD-CASSCF simulation depends on the number of orbitals, the cross section computed with the simulation is slightly shifted to the lower energy side. This can be improved by increasing the number of orbitals as well as the Ne simulations in the previous subsection.

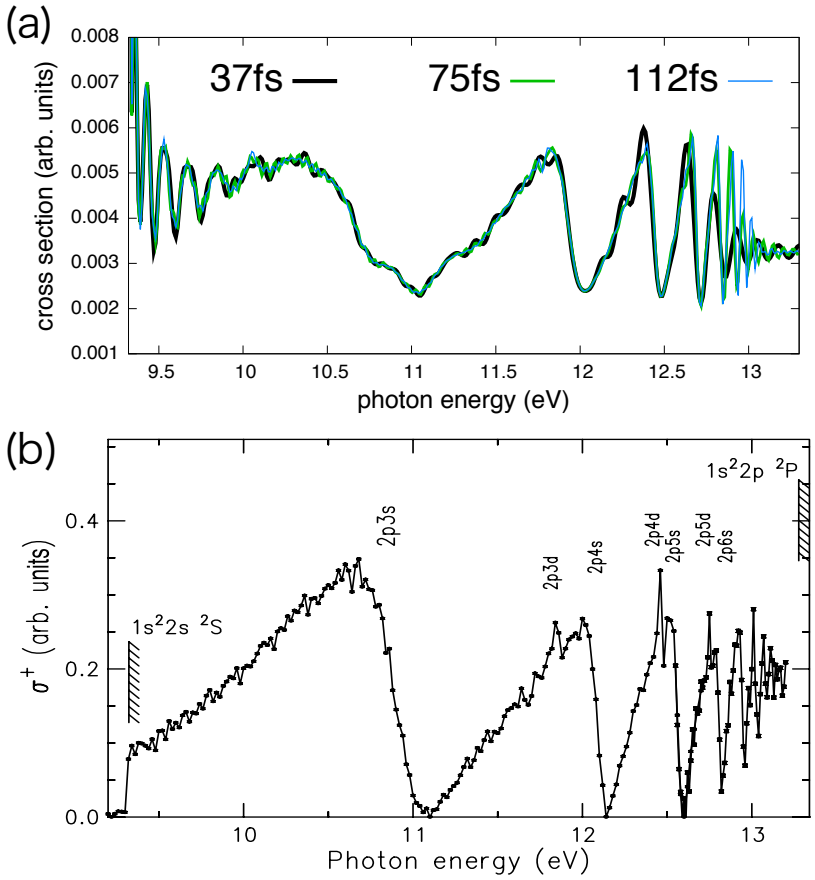

Figure 4.6: (a) One photon ionization cross section of a Beryllium atom calculated as the ratio of photoelectron energy spectra to pulse energy spectra with respect to the total time of propagation. The laser pulse used to calculate photoelectron energy spectra has a photon energy of 22 eV, an intensity of 1.0×10^{14}W/cm^2 and 3 optical cycles. (b) One photon ionization cross section of a Beryllium atom experimentally measured with monochromatized synchrotron radiation.Figure (b) is cited from Ref. [74], and modified to remove a least-square fitting curve in the original figure.

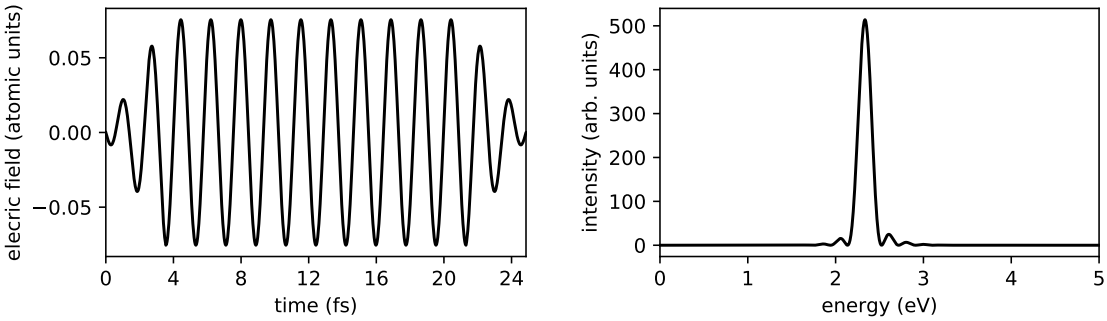

Figure 4.7: Temporal shape and intensity spectrum of the laser pulse considered for the case of Ar.

4.3.3 Argon

Next, we simulate ATI of an Ar atom subject to an intense visible laser pulse using the TD-ORMAS method and discuss the effect of electronic correlation. We consider a pulse, which has a peak intensity of $2.0 \times 10^{14}\,\mathrm{W/cm^2}$, a wavelength of 532 nm, and a pulse width of $N_{\mathrm{opt}} = 14$ optical cycles. The ponderomotive energy U_p is 5.285 eV. The temporal shape and energy spectrum of the pulse are shown in Fig. 4.7. We continue simulations for 24 fs after the end of the pulse without external fields so that the ejected electron wave packet entirely passes through the surface, i.e., the total simulation duration is ca. 50 fs.

Here, we subdivide n_{a} active orbitals into 4 and $(n_{\mathrm{a}} - 4)$ orbitals, as schematically illustrated in Fig. 4.8 for orbital decomposition $(n_{\mathrm{c}}, n_{\mathrm{d}}, n_{\mathrm{a}}) = (5, 0, 13)$. By setting the maximum number of electrons in the second subgroup [$(n_{\mathrm{a}} - 4)$ active orbitals] to 2 or 3, the configurations with up to double (SD) or triple (SDT) excitation are considered, respectively.

We first check the convergence with respect to the tSURFF radius R_{s} by using orbital classification $(n_{\mathrm{fc}}, n_{\mathrm{dc}}, n_{\mathrm{a}}) = (5, 0, 4)$ without excitation restriction and setting $R_0 = R_{\mathrm{s}}$. The calculated PES is virtually converged with $R_{\mathrm{s}} \geq 40\,\mathrm{a.u.}$ (Fig. 4.9). For $R_{\mathrm{s}} = 12$ and $20\,\mathrm{a.u.}$, on the other hand, we see deviation from the converged spectrum, considered to be an error introduced by the neglect of the Coulomb interaction beyond R_{s}. Especially, photoelectron yields in the lower energy region are overestimated, probably because low energy scattering states are sensitive to the tail of the nuclear Coulomb potential [47]. We set R_{s} and R_0 to be 40 a.u. in the rest of this subsection.

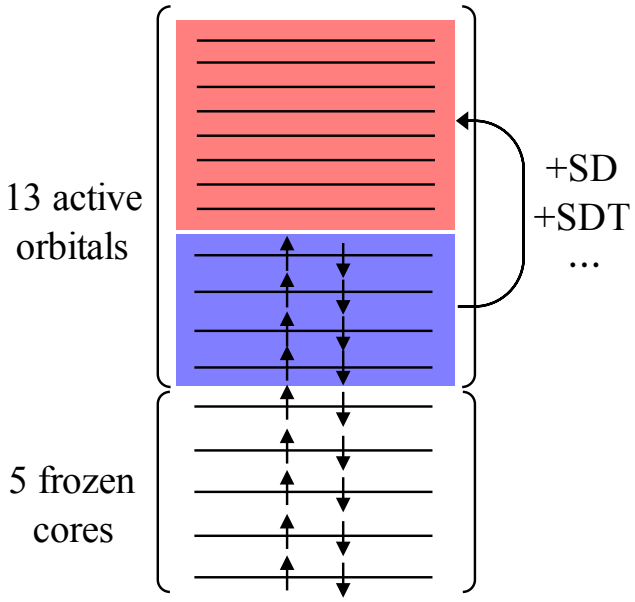

Figure 4.8: An example of the orbital subdivision of the TD-ORMAS method for an Ar atom with 18 electrons, which wave function is composed of 5 frozen cores and 13 active orbitals, $(n_{\mathrm{c}}, n_{\mathrm{d}}, n_{\mathrm{a}}) = (5, 0, 13)$. The excitation restrictions SD (SDT, $\cdots$) indicates that single and double (single, double and triple, $\cdots$) excitation from the blue to red group are only allowed.

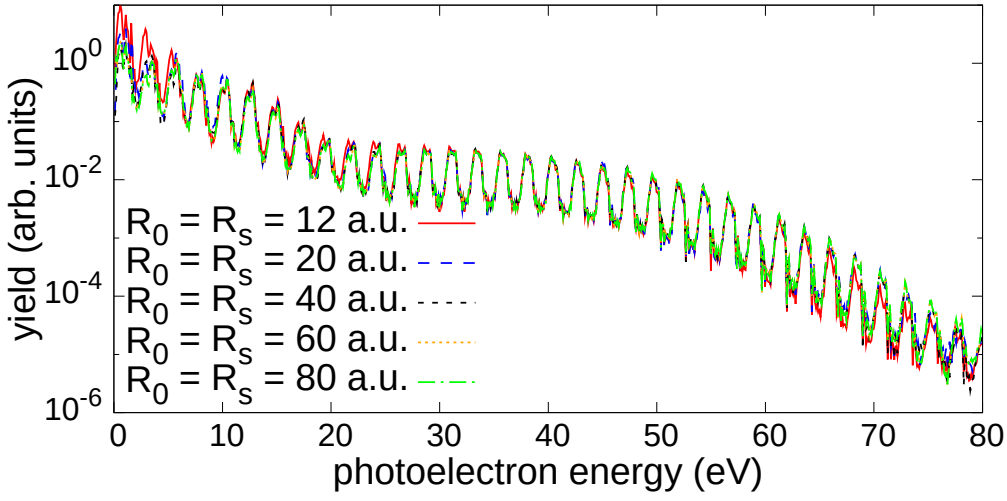

Figure 4.9: Photoelectron energy spectra of an Ar atom subject to a visible intense laser pulse with a wavelength of 532 nm and an intensity of 2.0×10^{14} W/cm^2. The results calculated with different values of $R_{\mathrm{s}} = R_0$ are compared. The orbital classification used is $(n_{\mathrm{fc}}, n_{\mathrm{dc}}, n_{\mathrm{a}}) = (5, 4, 0)$ without excitation restriction.

Figure 4.10 shows PES calculated with different orbital classifications. We can recognize the direct cutoff at $2U_p$ and rescattering cutoff at $10U_p$. In Fig. 4.10(a), the results with different numbers of active orbitals within single and double (SD) excitation are compared. The spectrum is nearly converged with 25 and 29 active orbitals. Figure 4.10(b) compares the results with SD and SDT excitation restriction and full CI (TD-CASSCF), with 13 active orbitals. The SDT and full CI results almost overlap each other, indicating that SDT is sufficient for numerical convergence. Thus, the result using 25 active orbitals with SDT excitation is expected to be numerically nearly exact. Then, in Figs. 4.10(c) and 4.11, we compare the PES calculated using 13, 20 and 25 active orbitals with SDT excitation restriction and also the TDHF result. The peak positions slightly depend on the number of orbitals, as we have also seen in Fig. 4.2. Moreover, in the TDHF case, the peaks are significantly broadened. The ATI peak position E_n corresponding to n-photon absorption is given by,

$$E_n = n\hbar\omega - I_\mathrm{p} - U_\mathrm{p}, \tag{4.26}$$

where I_p is the ionization potential. The difference in peak position observed in Fig. 4.10 can be attributed to that in I_p, which depends on the number of orbitals and excitation restriction. In addition, in mean-field approaches such as TDHF, the ionization potential effectively increases as ionization proceeds and the electron density near the nucleus decreases [75]. This results in the peak broadening.

To elucidate that this effect occurs in the TDHF simulation, we compare time evolution of the single ionization probabilities calculated with TDHF method and TD-ORMAS method using 25 active orbitals and SDT excitation restriction in Fig. 4.12. The ionization probability is defined as the probability of finding one electron outside the 20 a.u. radius. We can see the ionization probabilities agree with each other until around 5 optical cycles. However, after that, the ionization rate of the TDHF method decreases as the ionization proceeds, and thus the TDHF method underestimates the ionization probability. This finally results in 7% less than the TD-ORMAS simulation, where the TDHF and TD-ORMAS method show the probabilities to be approximately 22% and 29% at the end of the simulations. This indicates that ionization is suppressed as ionization proceeds in the TDHF method, which supports that the ionization potential effectively increases and the peak broadening stems from that.

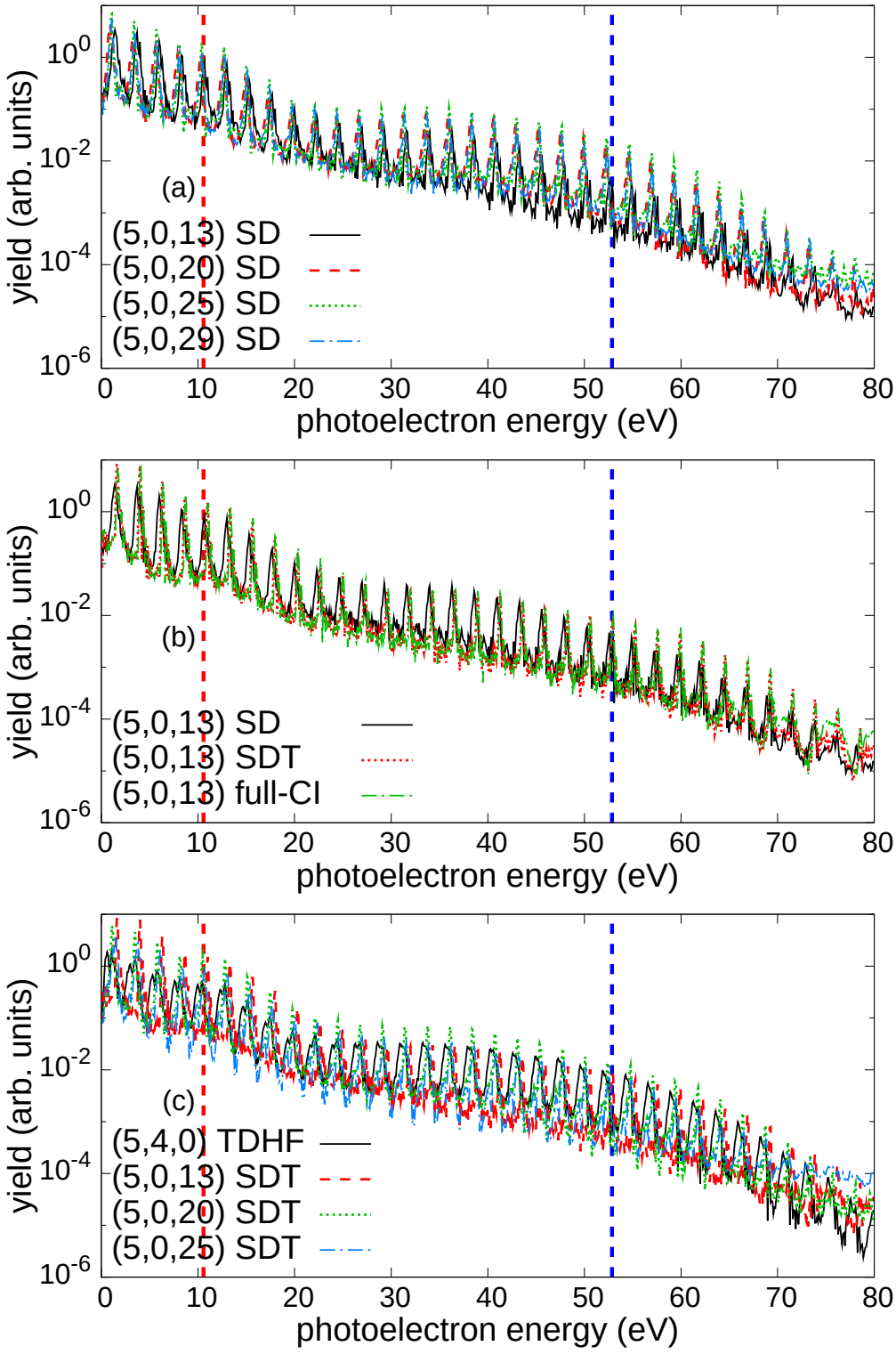

Figure 4.10: Photoelectron energy spectra of an Ar atom subject to a visible intense laser pulse with a wavelength of 532 nm and an intensity of 2.0×10^{14} W/cm^2. The red and blue dashed vertical lines show $2U_p$ and $10U_p$ ($U_p = 5.285$ eV). The results with different number of orbitals ($n_{\mathrm{fc}}, n_{\mathrm{dc}}, n_{\mathrm{a}}$) and excitation restrictions (SD, SDT, full-CI) are compared.

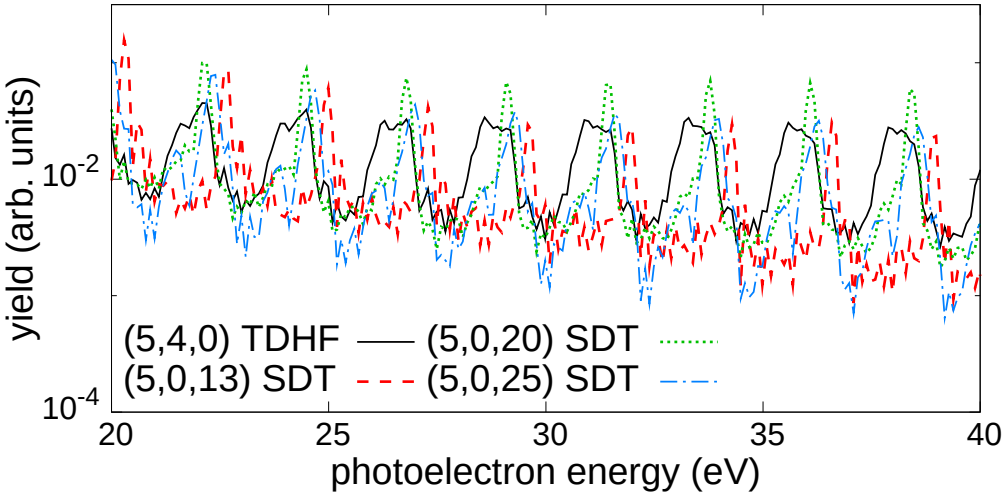

Figure 4.11: Enlarged view of Fig. 4.10(c)

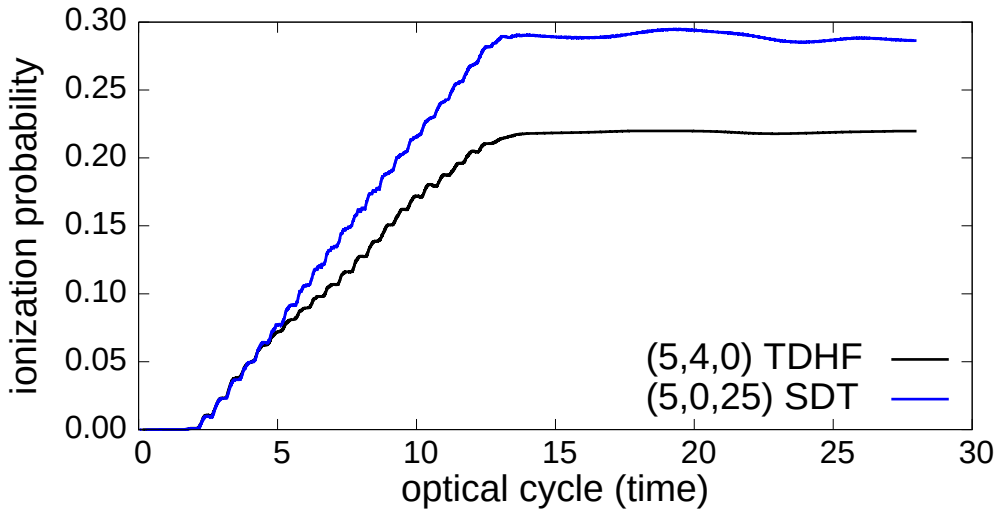

Figure 4.12: Time evolution of single ionization probabilities of an Ar atom exposed to a laser pulse with 532 nm wavelength, 2.0×10^{14} W/cm^2 peak intensity and 14 optical cycles. Single ionization probability is defined as probability of finding one electron outside the 20 a.u. radius. The results calculated with TDHF method and TD-ORMAS method using $(n_{\mathrm{fc}}, n_{\mathrm{dc}}, n_{\mathrm{a}}) = (5, 0, 25)$ and SDT excitation restriction are compared.

In Fig. 4.13, we show ARPES calculated with the TD-ORMAS method using 25 active orbitals with SDT excitation restriction and with the TDHF method using 4 dynamical-core orbitals. We see differences in detailed structure. In particular, the high-order ($> 2U_p$) rescattering contribution has much broader angular distribution in the TD-ORMAS result. The difference can also be clearly observed in Fig 4.14, which shows the photoelectron angular distribution (PAD) at 10 eV ($< 2U_p$) and 40 eV ($> 2U_p$), representatives of the lower and higher energy regions, respectively. At 10 eV photoelectron energy, where the main contribution is from direct ionization, all the results exhibit similar behavior. In contrast, at 40 eV photoelectron energy, for which rescattering from the parent ion is involved and thus strong electron correlation is expected, the calculated PAD varies with the number of orbitals till it approximately converges with $n_a = 25$. Especially, the TDHF method significantly underestimates the yield in the direction (90°) perpendicular to the laser polarization. This indicates that electronic correlation is non-negligible in detailed discussions of ATI ARPES.

Furthermore, we compare the TD-ORMAS simulations with classical simulations with classical trajectory Monte Carlo (CTMC) method in a collaborative research with the Institute of Nuclear Research of Hungarian Academy of Sciences [76]. The CTMC simulations were performed by Károly Tökési in Hungarian Academy of Sciences. The CTMC method numerically solves classical Newton's equations of motions with randomly generated initial conditions, and obtains a huge number of trajectories [77–80]. In this work, an Ar atom with 18 electrons is replaced with a one-electron atom [81, 82]. This model is the classical analogue of the quantum-mechanical effective single-electron treatment. The interaction between the ionic core and the active electron is described by a central model potential developed by Green [83], which is based on Hartree-Fock calculations. The potential can be written as

$$V(r) = \frac{Z - (N-1)\left(1 - \Omega^{-1}(r)\right)}{r} = \frac{Z(r)}{r}, \tag{4.27}$$

where Z is the nuclear charge, N is the total number of electrons in the atom, and

$$\Omega(r) = \frac{\eta}{\xi}\left(e^{r\xi} - 1\right) + 1. \tag{4.28}$$

The potential parameters ξ and η can be obtained by minimizing the energy for a given atom. For an Ar atom we used $\eta = 3.5$ and $\xi = 0.957$.

Figure. 4.15 shows ARPES calculated with the CTMC method. Comparing Fig. 4.15 with Fig. 4.14(b) using the TD-ORMAS method, we see that ARPES obtained with the CTMC method does not has the interference pattern, and the distribution is restricted to classically reachable region. In Fig. 4.16, we compare the photoelectron angular distributions (PAD) calculated with the TD-ORMAS method using 25 active orbitals and SDT excitation restriction and the CTMC method, at 10 eV and 40 eV. The PAD at 10 eV calculated with TD-ORMAS method oscillates centering that of the CTMC method. This indicates that the oscillation in the angular direction shows interference between different partial waves, which cannot be considered in the classical simulations. In Fig. 4.16(b) pre-

senting the PAD at 40 eV, the CTMC method shows a significantly different result from the TD-ORMAS one. In particular, in the direction perpendicular to the laser polarization (around 50° - 130°), the CTMC cannot reproduce the distribution of the TD-ORMAS method at all, since this is a region which electrons treated within classical mechanics are prohibited to reach.

As written in the first of this chapter, for direct projection, we would need to retain the complete wave function without being absorbed. Since the duration of the simulations in this subsection reaches ca. 50 fs, calculation of the photoelectron energy spectra at 40 eV, for example, would require the radius of the simulation box larger than 3500 a.u., which is unfeasibly large. Moreover, for Ar, an 18-electron atom, the computational cost of MCTDHF would be prohibitive. The introduction of orbital classification including frozen core and occupation restriction significantly reduces the number of Slater determinants, while keeping accuracy. Thus, the combination of the TD-ORMAS and the tSURFF methods enables converged simulations of ATI of an Ar atom and inspection of correlation effects in the ATI spectra.

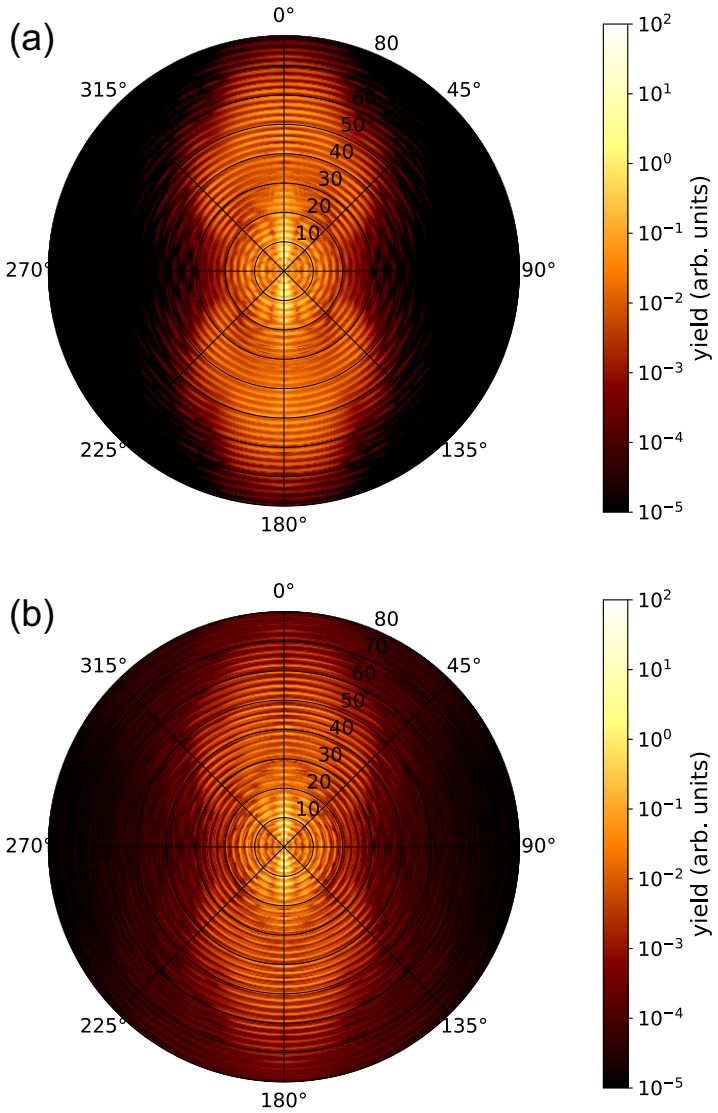

Figure 4.13: Angle-resolved photoelectron energy spectra of an Ar atom subject to a visible intense laser pulse with a wavelength of 532 nm and an intensity of 2.0×10^{14} W/cm^2. The laser polarization (z direction) corresponds to 0°. (a) $(n_{\mathrm{fc}}, n_{\mathrm{dc}}, n_{\mathrm{a}}) = (5, 4, 0)$, i.e., TDHF (b) $(n_{\mathrm{fc}}, n_{\mathrm{dc}}, n_{\mathrm{a}}) = (5, 0, 25)$ and SDT excitation restriction.

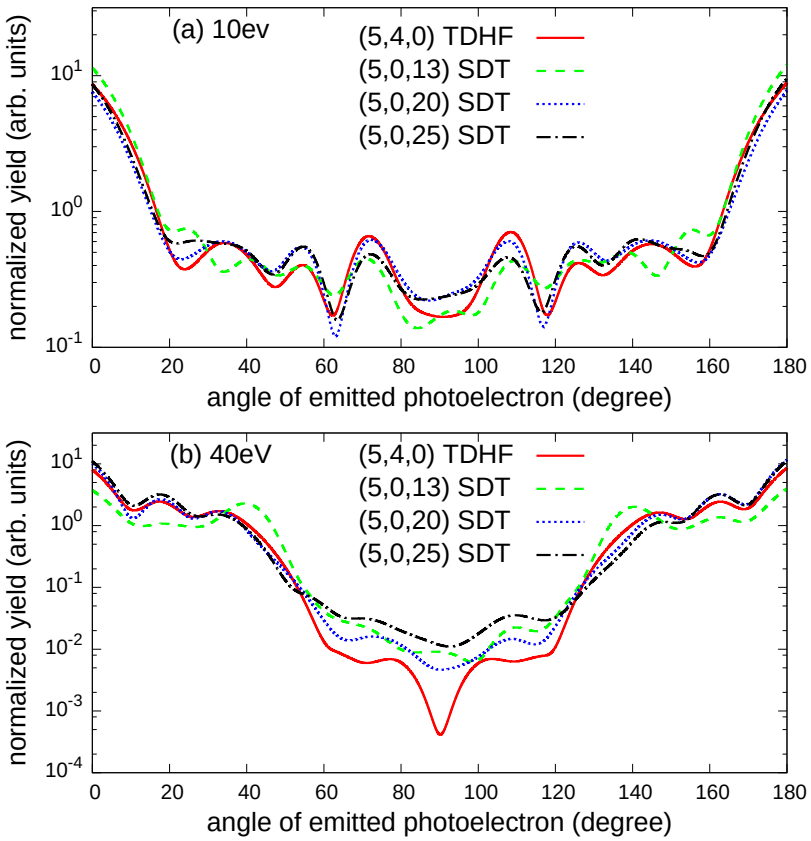

Figure 4.14: Angular distribution of photoelectron yields from an Ar atom at (a) 10 eV and (b) 40 eV, averaged over a $\pm$1.1eV energy range. The angle-integrated yield is normalized to unity. The results with different orbital conditions are compared.

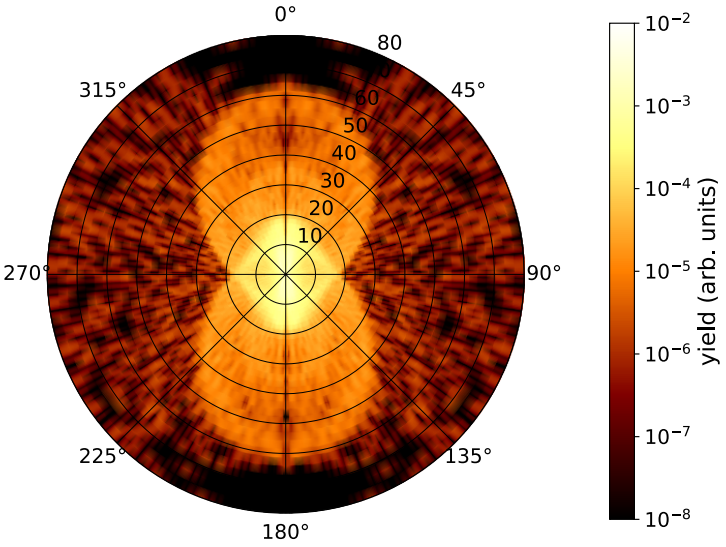

Figure 4.15: Angle-resolved photoelectron energy spectra of an Ar atom calculated with the CTMC method under the same laser parameter used in Fig. 4.13.

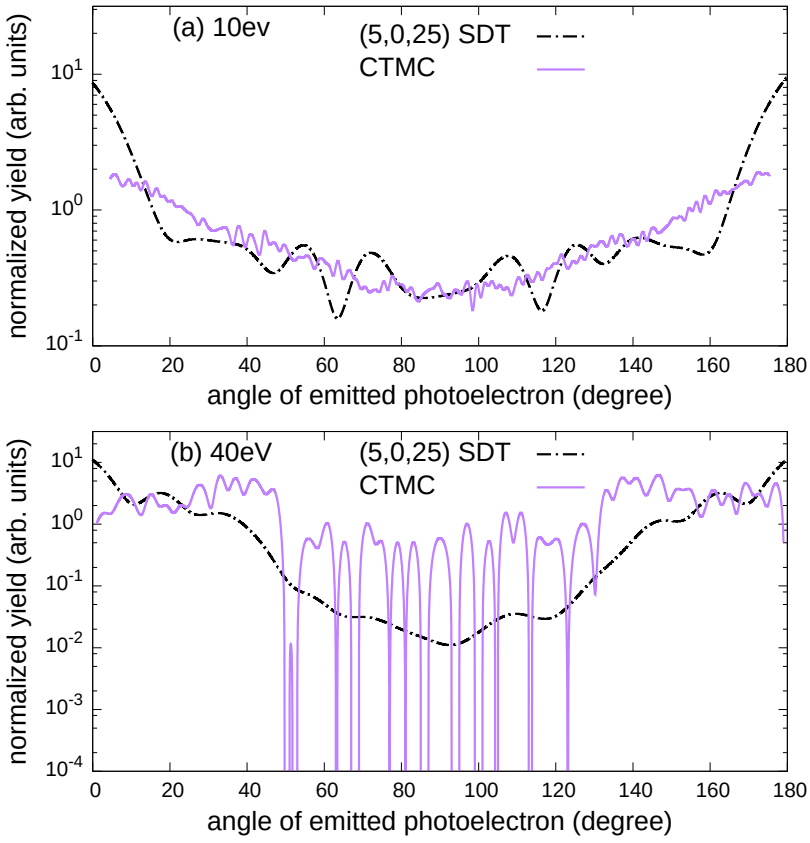

Figure 4.16: Angular distribution of photoelectron yields from an Ar atom at (a) 10 eV and (b) 40 eV, averaged over a ±1.1eV energy range. The angle-integrated yield is normalized to unity. The results calculated with the TD-ORMAS and CTMC method are compared.

Chapter 5

Extension to molecular systems

This chapter is not open to the public for the reason that the contents will be published in journals within 5 years.

Chapter 6
Conclusions

6.1 Summary

In this thesis, aiming for theoretical computation of accurate angle-resolved photoelectron spectra from multielectron atoms subject to intense and ultrafast laser pulses, we have developed a realtime *ab initio* simulation method by combining the TD-ORMAS method, irECS and the tSURFF method.

To reduce huge computational costs of the TD-ORMAS simulations due to a large simulation box, we have first applied irECS as an efficient absorbing boundary to the TD-ORMAS method. This application minimally neglects only the Coulomb force between electrons in the unscaled region and that acting from electrons in the scaled region on those in the unscaled region. For discretization of the scaled region, we have introduced Gauss-Laguerre-Radau quadrature points to construct exponentially dumped infinite-range FEDVR basis functions that are, conveniently, orthonormal and finite only at a grid point associated with each basis function. In order to demonstrate efficiency and accuracy, we have applied the present method to Be and Ne atoms and calculated ionization probabilities and HHG spectra for intense near-infrared laser pulses. We have obtained the results that perfectly agree with the converged results using much larger absorbing radii, even when atoms were massively ionized. While achieving excellent accuracy, decreasing the size of the simulation box thanks to irECS has led to the significant reduction of computational costs, by 66% for Be and 80% for Ne in the present case.

To obtain photoelectron spectra in systems described within the MCSCF framework such as the TD-ORMAS method, the photoelectron reduced density matrix has been introduced, whose diagonal elements in the momentum space correspond to photoelectron spectra. We have applied to the tSURFF method based on the assumption that the nuclear potentials and interelectronic Coulomb interaction do not affect the dynamics of photoelectrons in a region at a large distance from nuclei, and derived the equation of motion for photoelectron momentum amplitudes of each orbital. Since one of the biggest benefits of tSURFF is not needing to hold the complete wave function within the simulation box, it allows the combined use of an efficient absorbing boundary such as irECS. We have applied the present development to compute photoelectron spectra from Ne, Be and Ar atoms. In the calculation of a Ne atom subject to attosecond XUV pulses, we have observed the perfect agreement between PES obtained by the tSURFF method

and direct projection. This indicates that the neglect of electron-electron and nucleus-electron Coulomb interaction is a good approximation. Next, we have simulated one photon ionization process of a Be atom and computed one photon ionization cross section. The result agrees with the experimental one. This process includes the autoionization of doubly excited states, and thus this shows that we can correctly simulate phenomena in which electronic correlation plays an essential role. As a final demonstration, we have presented converged calculation of ATI spectra from an Ar atom including electronic correlation, which would require prohibitive computational cost without tSURFF and irECS. Comparing the ATI ARPES computed with the TDHF method and the converged one with the TD-ORMAS method, we have found a significant difference in a high energy region for which rescattering from the parent ion is involved, and especially in a direction perpendicular to the laser polarization. This indicates that electronic correlation is non-negligible in detailed discussions of ATI ARPES.

To extend the present development for atoms to molecules, we have implemented the TD-ORMAS method and the tSURFF method with the adaptive finite element method which employs a multiresolution mesh in the Cartesian coordinate. Smooth ECS, which is suited to a multiresolution mesh, has been applied to this implementation. With this implementation, we have performed TDHF simulations to compute photoelectron momentum spectra from a hydrogen molecule. The spectra qualitatively agree with that obtained by Fermi's golden rule reflecting a molecular structure and laser polarizations.

6.2 Future prospects

6.2.1 Ion-state-resolved photoelectron spectra

Electronic dynamics induced by intense and ultrashort laser pulses usually involves multichannel effects and multiple ionization dynamics. Furthermore, under intense fields, excitation and multiple ionization successively occur, and thus initially generated photoions and finally generated ones possibly have completely different states. However, it is difficult to understand such processes only from photoelectron spectra, in which all the processes are superpositioned.

These processes can be identified by observing not only photoelectron spectra but also associating photoionic states. This coincident observation can be achieved by introducing the ion-state-resolved photoelectron reduced density matrix $\tilde{P}_I(\boldsymbol{k}, \boldsymbol{k'})$, which is defined by resolving the photoelectron reduced density matrix (PRDM) defined in Eq. (4.8) into contributions from an ionic state I,

$$\tilde{P}_I(\boldsymbol{k}, \boldsymbol{k'}) = \langle I, \chi_{\boldsymbol{k}}(t) | \Psi(t) \rangle \langle \Psi(t) | I, \chi_{\boldsymbol{k'}}(t) \rangle . \tag{6.1}$$

$|I, \chi_{\boldsymbol{k}}(t)\rangle$ denotes a wave function with an ionic eigenstate I and a scattered state $\chi_{\boldsymbol{k}}$. Ionic eigenstates can be obtained by usual quantum chemistry computations for static states. As well as the PRDM, the diagonal part of the ion-state-resolved photoelectron reduced

density matrix is interpreted as photoelectron momentum spectra associated with an ionic state I. Through resolving photoelectron spectra based on ionic states, for example, we can study a correlation between generated ionic states and observed photoelectron spectra.

6.2.2 Application to larger systems and extension beyond the fixed-nuclei approximation

In this study, the application of the implementation for molecular systems has been limited to the TDHF method. The next step is to apply it to the TD-MCSCF methods such as the TD-ORMAS method. Furthermore, the time-dependent optimized coupled-cluster (TD-OCC) method has been recently proposed [84], which is size extensive, and thus applicable to further large systems. Applications of our developments for atoms and molecules to the TD-OCC method will enable to extract photoelectron spectra from larger systems.

Whereas we have treated systems under the fixed-nuclei approximation, electron-nuclear dynamics in molecules driven by a laser pulse is recently intensively studied [85, 86]. One of the simplest methods to consider nuclear dynamics is the Ehrenfest method, which classically treats nuclei [87, 88]. For the quantum treatment of nuclear dynamics, the multi-configuration time-dependent Hartree method [89], which expresses a total wave function as a superposition of Hartree products, has been applied to many phenomena [90–92]. In addition to this, a TD-MCSCF method for general particles have been recently proposed [93]. Since our application of the tSURFF method is based on the equation of motion of electronic orbitals and the reduced density matrix, it is straightforward to extend our present approach to other multielectron *ab initio* methods. The extension to molecular dynamics considering nuclear motion would enable precise prediction of photoelectron spectra from complicated processes and lead to a better understanding of experimental results such as electron-ion coincidence measurements in dissociation of molecules caused by strong laser pulses.

Appendix A

Atomic units

The atomic units (a.u.) is a convenient system for atomic physics, which defines the mass of a electron m_{e}, the elementary charge e and the reduced Planck's constant $\hbar$ as 1. In this system, the units of length and energy are given as the Bohr radius and the Hartree energy, respectively. We show typical atomic units in Table A.1.

Table A.1: Atomic units

dimension	value
length	5.29×10^{-11} m
energy	27.2 eV
time	0.00242 fs
velocity	2.19×10^{6} m/s
electric field	5.14×10^{11} V/m
field intensity	3.51×10^{16} W/cm^2

Bibliography

[1] D. Strickland and G. Mourou. Compression of amplified chirped optical pulses. *Optics Communications*, 56(3):219 – 221, 1985.

[2] T. J. McIlrath, P. H. Bucksbaum, R. R. Freeman, and M. Bashkansky. Above-threshold ionization processes in xenon and krypton. *Phys. Rev. A*, 35:4611–4623, Jun 1987.

[3] P. B. Corkum. Plasma perspective on strong field multiphoton ionization. *Phys. Rev. Lett.*, 71:1994–1997, Sep 1993.

[4] K. C. Kulander, K. J. Schafer, and J. L. Krause. Dynamics of short-pulse excitation, ionization and harmonic conversion. In *Super-Intense Laser-Atom Physics*, pages 95–110. Springer US, Boston, MA„ 1993.

[5] Z. Chang. *Fundamentals of attosecond optics*. CRC Press, 2011.

[6] F. Remacle and R. D. Levine. An electronic time scale in chemistry. *Proceedings of the National Academy of Sciences*, 103(18):6793–6798, 2006.

[7] L. Cederbaum and J. Zobeley. Ultrafast charge migration by electron correlation. *Chemical Physics Letters*, 307(3–4):205 – 210, 1999.

[8] J. Breidbach and L. S. Cederbaum. Universal attosecond response to the removal of an electron. *Phys. Rev. Lett.*, 94:033901, Jan 2005.

[9] F. Calegari, D. Ayuso, A. Trabattoni, L. Belshaw, S. De Camillis, S. Anumula, F. Frassetto, L. Poletto, A. Palacios, P. Decleva, J. B. Greenwood, F. Mart'in, and M. Nisoli. Ultrafast electron dynamics in phenylalanine initiated by attosecond pulses. *Science*, 346(6207):336–339, 2014.

[10] K. C. Kulander, K. J. Schafer, and J. L. Krause. Single-active electron calculation of multiphoton process in krypton. *International Journal of Quantum Chemistry*, 40(S25):415–429, 1991.

[11] J. Zanghellini, M. Kitzler, C. Fabian, T. Brabec, and A. Scrinzi. An mctdhf approach to multielectron dynamics in laser fields an mctdhf approach to multielectron dynamics in laser fields an mctdhf approach to multielectron dynamics in laser fields. *Laser Phys.*, 13:1064, 2003.

[12] T. Kato and H. Kono. Time-dependent multiconfiguration theory for electronic dynamics of molecules in an intense laser field. *Chem. Phys. Lett.*, 392(4-6):533–540, Jul 2004.

[13] J. Caillat, J. Zanghellini, M. Kitzler, O. Koch, W. Kreuzer, and A. Scrinzi. Correlated multielectron systems in strong laser fields: A multiconfiguration time-dependent hartree-fock approach. *Phys. Rev. A*, 71:012712, Jan 2005.

[14] T. Sato and K. L. Ishikawa. Time-dependent complete-active-space self-consistent-field method for multielectron dynamics in intense laser fields. *Phys. Rev. A*, 88:023402, Aug 2013.

[15] T. Sato and K. L. Ishikawa. Time-dependent multiconfiguration self-consistent-field method based on the occupation-restricted multiple-active-space model for multielectron dynamics in intense laser fields. *Phys. Rev. A*, 91:023417, Feb 2015.

[16] A. D. Bandrauk, F. Fillion-Gourdeau, and E. Lorin. Atoms and molecules in intense laser fields: gauge invariance of theory and models. *Journal of Physics B: Atomic, Molecular and Optical Physics*, 46(15):153001, jul 2013.

[17] J. Frenkel. *Wave Mechanics: Advanced General Theory.* Oxford, U.K.: Clarendon Press, 1934.

[18] P.-O. Löwdin and P. Mukherjee. Some comments on the time-dependent variation principle. *Chemical Physics Letters*, 14(1):1 – 7, 1972.

[19] R. Moccia. Time-dependent variational principle. *International Journal of Quantum Chemistry*, 7(4):779–783, 1973.

[20] K. C. Kulander. Time-dependent hartree-fock theory of multiphoton ionization: Helium. *Phys. Rev. A*, 36:2726–2738, Sep 1987.

[21] M. S. Pindzola, D. C. Griffin, and C. Bottcher. Validity of time-dependent hartree-fock theory for the multiphoton ionization of atoms. *Phys. Rev. Lett.*, 66:2305–2307, May 1991.

[22] M. S. Pindzola, P. Gavras, and T. W. Gorczyca. Time-dependent unrestricted hartree-fock theory for the multiphoton ionization of atoms. *Phys. Rev. A*, 51:3999–4004, May 1995.

[23] N. E. Dahlen and R. van Leeuwen. Double ionization of a two-electron system in the time-dependent extended hartree-fock approximation. *Phys. Rev. A*, 64:023405, Jul 2001.

[24] T. Sato, K. L. Ishikawa, I. Březinová, F. Lackner, S. Nagele, and J. Burgdörfer. Time-dependent complete-active-space self-consistent-field method for atoms: Application to high-order harmonic generation. *Phys. Rev. A*, 94:023405, Aug 2016.

[25] T. Sato, Y. Orimo, T. Teramura, O. Tugs, and K. L. Ishikawa. *Time-Dependent Complete-Active-Space Self-Consistent-Field Method for Ultrafast Intense Laser Science*, pages 143–171. Springer International Publishing, Cham, 2018.

[26] I. S. Wahyutama, T. Sato, and K. L. Ishikawa. Time-dependent multiconfiguration self-consistent-field study on resonantly enhanced high-order harmonic generation from transition-metal elements. *Phys. Rev. A*, 99:063420, Jun 2019.

[27] T. Sato and K. L. Ishikawa. Time-dependent multiconfiguration methods for intense laser-driven multielectron dynamics. In *High-Brightness Sources and Light-driven Interactions*, page HW1A.6. Optical Society of America, 2018.

[28] J. L. Krause, K. J. Schafer, and K. C. Kulander. Calculation of photoemission from atoms subject to intense laser fields. *Phys. Rev. A*, 45:4998–5010, Apr 1992.

[29] U. V. Riss and H. Meyer. Investigation on the reflection and transmission properties of complex absorbing potentials. *J. Chem. Phys.*, 105(4):1409–1419, 1996.

[30] L. Greenman, P. J. Ho, S. Pabst, E. Kamarchik, D. A. Mazziotti, and R. Santra. Implementation of the time-dependent configuration-interaction singles method for atomic strong-field processes. *Phys. Rev. A*, 82:023406, Aug 2010.

[31] C. W. McCurdy, C. K. Stroud, and M. K. Wisinski. Solving the time-dependent schrödinger equation using complex-coordinate contours. *Phys. Rev. A*, 43:5980–5990, Jun 1991.

[32] A. Scrinzi. Infinite-range exterior complex scaling as a perfect absorber in time-dependent problems. *Phys. Rev. A*, 81:053845, May 2010.

[33] D. J. Haxton, K. V. Lawler, and C. W. McCurdy. Multiconfiguration time-dependent hartree-fock treatment of electronic and nuclear dynamics in diatomic molecules. *Phys. Rev. A*, 83:063416, Jun 2011.

[34] D. A. Telnov, K. E. Sosnova, E. Rozenbaum, and Shih-I Chu. Exterior complex scaling method in time-dependent density-functional theory: Multiphoton ionization and high-order-harmonic generation of ar atoms. *Phys. Rev. A*, 87:053406, May 2013.

[35] V. P. Majety, A. Zielinski, and A. Scrinzi. Photoionization of few electron systems: a hybrid coupled channels approach. *New Journal of Physics*, 17(6):063002, 2015.

[36] A. Zielinski, V. P. Majety, and A. Scrinzi. Double photoelectron momentum spectra of helium at infrared wavelength. *Phys. Rev. A*, 93:023406, Feb 2016.

[37] P. M. Paul, E. S. Toma, P. Breger, G. Mullot, F. Aug'e, P. Balcou, H. G. Muller, and P. Agostini. Observation of a train of attosecond pulses from high harmonic generation. *Science*, 292(5522):1689–1692, 2001.

[38] E. Goulielmakis, M. Uiberacker, R. Kienberger, A. Baltuska, V. Yakovlev, A. Scrinzi, T. Westerwalbesloh, U. Kleineberg, U. Heinzmann, M. Drescher, and F. Krausz. Direct measurement of light waves. *Science*, 305(5688):1267–1269, 2004.

[39] V. Gruson, L. Barreau, Á. Jiménez-Galan, F. Risoud, J. Caillat, A. Maquet, B. Carré, F. Lepetit, J.-F. Hergott, T. Ruchon, L. Argenti, R. Taïeb, F. Martín, and P. Salières. Attosecond dynamics through a fano resonance: Monitoring the birth of a photoelectron. *Science*, 354(6313):734–738, 2016.

[40] A. Kaldun, A. Blättermann, V. Stooß, S. Donsa, H. Wei, R. Pazourek, S. Nagele, C. Ott, C. D. Lin, J. Burgdörfer, and T. Pfeifer. Observing the ultrafast buildup of a fano resonance in the time domain. *Science*, 354(6313):738–741, 2016.

[41] D. M. Villeneuve, P. Hockett, M. J. J. Vrakking, and H. Niikura. Coherent imaging of an attosecond electron wave packet. *Science*, 356(6343):1150–1153, 2017.

[42] M. Drescher, M. Hentschel, R. Kienberger, G. Tempea, C. Spielmann, G. A. Reider, P. B. Corkum, and F. Krausz. X-ray pulses approaching the attosecond frontier. *Science*, 291(5510):1923–1927, 2001.

[43] J. Itatani, F. Quéré, G. L. Yudin, M. Y. Ivanov, F. Krausz, and P. B. Corkum. Attosecond streak camera. *Phys. Rev. Lett.*, 88:173903, Apr 2002.

[44] M. Kitzler, N. Milosevic, A. Scrinzi, F. Krausz, and T. Brabec. Quantum theory of attosecond xuv pulse measurement by laser dressed photoionization. *Phys. Rev. Lett.*, 88:173904, Apr 2002.

[45] Y. Mairesse and F. Quéré. Frequency-resolved optical gating for complete reconstruction of attosecond bursts. *Phys. Rev. A*, 71:011401, Jan 2005.

[46] M. Schultze, M. Fieß, N. Karpowicz, J. Gagnon, M. Korbman, M. Hofstetter, S. Neppl, A. L. Cavalieri, Y. Komninos, T. Mercouris, C. A. Nicolaides, R. Pazourek, S. Nagele, J. Feist, J. Burgdörfer, A. M. Azzeer, R. Ernstorfer, R. Kienberger, U. Kleineberg, E. Goulielmakis, F. Krausz, and V. S. Yakovlev. Delay in photoemission. *Science*, 328(5986):1658–1662, 2010.

[47] L. Tao and A. Scrinzi. Photo-electron momentum spectra from minimal volumes: the time-dependent surface flux method. *New Journal of Physics*, 14(1):013021, jan 2012.

[48] A. Scrinzi. t-surff: fully differential two-electron photo-emission spectra. *New J. Phys.*, 14(8):085008, 2012.

[49] A. Karamatskou, S. Pabst, Y.-J. Chen, and R. Santra. Calculation of photoelectron spectra within the time-dependent configuration-interaction singles scheme. *Phys. Rev. A*, 89:033415, Mar 2014.

[50] P. Wopperer, U. De Giovannini, and A. Rubio. Efficient and accurate modeling of electron photoemission in nanostructures with tddft. *The European Physical Journal B*, 90(3):51, Mar 2017.

[51] T. N. Rescigno and C. W. McCurdy. Numerical grid methods for quantum-mechanical scattering problems. *Phys. Rev. A*, 62:032706, Aug 2000.

[52] C. W. McCurdy, M. Baertschy, and T. N. Rescigno. Solving the three-body coulomb breakup problem using exterior complex scaling. *J. Phys. B: At. Mol. Opt. Phys.*, 37(17):R137, 2004.

[53] B. I. Schneider, J. Feist, S. Nagele, R. Pazourek, S. Hu, L. A. Collins, and J. Burgdörfer. *Recent Advances in Computational Methods for the Solution of the Time-Dependent Schrödinger Equation for the Interaction of Short, Intense Radiation with One and Two Electron Systems*, pages 149–208. Springer New York, New York, NY, 2011.

[54] S. Cox and P. Matthews. Exponential time differencing for stiff systems. *Journal of Computational Physics*, 176(2):430 – 455, 2002.

[55] M. Tokman. Efficient integration of large stiff systems of odes with exponential propagation iterative (epi) methods. *Journal of Computational Physics*, 213(2):748 – 776, 2006.

[56] M. Tokman. A new class of exponential propagation iterative methods of runge–kutta type (epirk). *Journal of Computational Physics*, 230(24):8762 – 8778, 2011.

[57] Y. Orimo, T. Sato, A. Scrinzi, and K. L. Ishikawa. Implementation of the infinite-range exterior complex scaling to the time-dependent complete-active-space self-consistent-field method. *Phys. Rev. A*, 97:023423, Feb 2018.

[58] A. Scrinzi and N. Elander. A finite element implementation of exterior complex scaling for the accurate determination of resonance energies. *The Journal of Chemical Physics*, 98(5):3866–3875, Mar 1993.

[59] T. N. Rescigno, M. Baertschy, D. Byrum, and C. W. McCurdy. Making complex scaling work for long-range potentials. *Phys. Rev. A*, 55:4253–4262, Jun 1997.

[60] W. Gautschi. Gauss–radau formulae for jacobi and laguerre weight functions. *Math. Comput. Simulat.*, 54(4–5):403 – 412, 2000.

[61] M. Weinmüller, M. Weinmüller, J. Rohland, and A. Scrinzi. Perfect absorption in schrödinger-like problems using non-equidistant complex grids. *Journal of Computational Physics*, 333(Supplement C):199 – 211, 2017.

[62] K. L. Ishikawa and T. Sato. A review on ab initio approaches for multielectron dynamics. *IEEE J. Sel. Topics Quantum Electron.*, 21(5):8700916, 2015.

[63] J. Parker, K. T. Taylor, C. W. Clark, and S. Blodgett-Ford. Intense-field multiphoton ionization of a two-electron atom. *J. Phys. B: At. Mol. Opt. Phys.*, 29(2):L33, 1996.

[64] J. Colgan, M. S. Pindzola, and F. Robicheaux. Time-dependent close-coupling calculations for the double photoionization of he and h 2. *J. Phys. B: At. Mol. Opt. Phys.*, 37(23):L377, 2004.

[65] J. Feist, S. Nagele, R. Pazourek, E. Persson, B. I. Schneider, L. A. Collins, and J. Burgdörfer. Nonsequential two-photon double ionization of helium. *Phys. Rev. A*, 77:043420, Apr 2008.

[66] Y. Orimo, T. Sato, and K. L. Ishikawa. Application of the time-dependent surface flux method to the time-dependent multiconfiguration self-consistent-field method. *Phys. Rev. A*, 100:013419, Jul 2019.

[67] J. J. Omiste, W. Li, and L. B. Madsen. Electron correlation in beryllium: Effects in the ground state, short-pulse photoionization, and time-delay studies. *Phys. Rev. A*, 95:053422, May 2017.

[68] P. A. M. Dirac. Note on exchange phenomena in the thomas atom. *Mathematical Proceedings of the Cambridge Philosophical Society*, 26(3):376–385, 007 1930.

[69] NIST ASD Team. Atomic spectra database. *https://www.nist.gov/pml/atomic-spectra-database*.

[70] G. Mehlman-Balloffet and J. M. Esteva. Far-Ultraviolet Absorption Spectra with Auto-Ionized Levels of Beryllium and Magnesium. *Astrophys. J.*, 157:945, Aug 1969.

[71] P. F. O'Mahony and C. H. Greene. Doubly excited states of beryllium and magnesium. *Phys. Rev. A*, 31:250–259, Jan 1985.

[72] B. Zhou and C. D. Lin. Photoionization of the beryllium atom. *Phys. Rev. A*, 51:1286–1290, Feb 1995.

[73] U. Fano. Effects of configuration interaction on intensities and phase shifts. *Phys. Rev.*, 124:1866–1878, Dec 1961.

[74] R. Wehlitz, D. Lukić, and J. B. Bluett. Resonance parameters of autoionizing be $2pn\updownarrow$ states. *Phys. Rev. A*, 68:052708, Nov 2003.

[75] K. C. Kulander, K. J. Schafer, and J. L. Krause. Time-Dependent Studies of Multi-photon Processes. In *Atoms in Intense Laser Fields*, page 247, 1992.

[76] Orimo, Yuki, Tökési, Károly, Sato, Takeshi, and Ishikawa, Kenichi L. Comparison between quantum and classical calculations for above threshold ionization of argon. *Eur. Phys. J. D*, 73(7):153, 2019.

[77] R. Abrines and I. C. Percival. Classical theory of charge transfer and ionization of hydrogen atoms by protons. *Proceedings of the Physical Society*, 88(4):861–872, aug 1966.

[78] R. E. Olson and A. Salop. Charge-transfer and impact-ionization cross sections for fully and partially stripped positive ions colliding with atomic hydrogen. *Phys. Rev. A*, 16:531–541, Aug 1977.

[79] K. Tökési and G. Hock. Versatility of the exit channels in the three-body ctmc method. *Nuclear Instruments and Methods in Physics Research Section B: Beam Interactions with Materials and Atoms*, 86(1):201 – 204, 1994.

[80] K. Tokési and G. Hock. Double electron capture in collisions up to 1500 keV/amu projectile impact. *Journal of Physics B: Atomic, Molecular and Optical Physics*, 29(4):L119–L125, feb 1996.

[81] K. Tőkési and Á. Kövér. Existence of the electron capture to the continuum peak at positron impact. *Nuclear Instruments and Methods in Physics Research Section B: Beam Interactions with Materials and Atoms*, 154(1):259 – 262, 1999.

[82] K. Tökési and Á. Kövér. Electron capture to the continuum at 54.4 eV positron-argon atom collisions. *Journal of Physics B: Atomic, Molecular and Optical Physics*, 33(16):3067–3077, aug 2000.

[83] A. Green. An analytic independent particle model for atoms: I. initial studies. volume 7 of *Advances in Quantum Chemistry*, pages 221 – 262. Academic Press, 1973.

[84] T. Sato, H. Pathak, Y. Orimo, and K. L. Ishikawa. Communication: Time-dependent optimized coupled-cluster method for multielectron dynamics. *The Journal of Chemical Physics*, 148(5):051101, 2018.

[85] F. Lépine, M. Y. Ivanov, and M. J. J. Vrakking. Attosecond molecular dynamics: fact or fiction? *Nature Photonics*, 8(3):195–204, 2014.

[86] M. J. J. Vrakking and F. Lepine, editors. *Attosecond Molecular Dynamics*. Theoretical and Computational Chemistry Series. The Royal Society of Chemistry, 2019.

[87] P. Ehrenfest. Bemerkung über die angenäherte gültigkeit der klassischen mechanik innerhalb der quantenmechanik. *Zeitschrift für Physik*, 45(7):455–457, Jul 1927.

[88] X. Li, J. C. Tully, H. B. Schlegel, and M. J. Frisch. Ab initio ehrenfest dynamics. *The Journal of Chemical Physics*, 123(8):084106, 2005.

[89] M. Beck, A. Jäckle, G. Worth, and H.-D. Meyer. The multiconfiguration time-dependent hartree (mctdh) method: a highly efficient algorithm for propagating wavepackets. *Physics Reports*, 324(1):1 – 105, 2000.

[90] L. Wang, H.-D. Meyer, and V. May. Femtosecond laser pulse control of multidimensional vibrational dynamics: Computational studies on the pyrazine molecule. *The Journal of Chemical Physics*, 125(1):014102, 2006.

[91] C. Jhala and M. Lein. Multiconfiguration time-dependent hartree approach for electron-nuclear correlation in strong laser fields. *Phys. Rev. A*, 81:063421, Jun 2010.

[92] G. J. Halász, A. Vibók, N. Moiseyev, and L. S. Cederbaum. Nuclear-wave-packet quantum interference in the intense laser dissociation of the d_2^+ molecule. *Phys. Rev. A*, 88:043413, Oct 2013.

[93] R. Anzaki, T. Sato, and K. L. Ishikawa. A fully general time-dependent multiconfiguration self-consistent-field method for the electron–nuclear dynamics. *Phys. Chem. Chem. Phys.*, 19:22008–22015, 2017.

Acknowledgement

I would like to express my deepest gratitude to my supervisor Prof. Kenichi L. Ishikawa. Prof. Ishikawa has always kindly supported me and given a lot of opportunities to learn various things including not only my study but also many experiences in international conferences and joint researches. I also want to thank him for allowing me to freely choose my research theme.

I am deeply grateful to Assoc. Prof. Takeshi Sato. Without his devoted support and meaningful discussions with him, I could have never spent my beneficial doctoral course. Using and studying his wonderful simulation codes have inspired me and opened a way to develop a simulator for molecules presented in Ch. 5.

I greatly thank Prof. Armin Scrinzi in Ludwig Maximilian University of Munich. My short stay in his laboratory was a valuable experience for me and became an important opportunity to consider my advance to the doctoral course. I also appreciate his insightful comments and suggestions for the application of ECS and irECS to the multielectron systems presented Ch. 3.

I also really thank Prof. Károly Tökési in the Institute of Nuclear Research of Hungarian Academy of Sciences. The collaborative research with him expanded my knowledge and gave me a fruitful experience.

I would like to thank Dr. Yasushi Shinohara in Ishikawa laboratory. His advice on developments of simulation codes and linear algebra algorithms were very helpful.

I want to thank all the members and the former members in Ishikawa laboratory, namely, Dr. Himadri Pathak, Dr. Imam S. Wahyutama, Mr. Ryoji Anzaki, Mr. Takuma Teramura, Mr. Kazma Komatsu, Ms. Oyunbileg Tugs, Ms. Chisa Koriyama, Mr. Mizuki Tani, Mr. Yutaro Isono, and Mr. Kakeru Sasaki. I also express my thanks to Dr. Takuya Ikemachi, a former student in Gonokami laboratory. I was able to spend my enjoyable Ph.D. life thanks to them. I am also grateful to Ms. Yumiko Kumaoka, the secretary in Ishikawa laboratory, for her plenty of support for me.

This research was supported by CREST (Grant No. JPMJCR15N1), JST, by JSPS and HAS under the Japan-Hungary Research Cooperative Program, by the Graduate School of Engineering, University of Tokyo, Doctoral Student Special Incentives Program (SEUT Fellowship program), and by JSPS Research Fellowship for Doctoral Course Students (DC2). I gratefully acknowledge all the financial supports.

Finally, I would like to express my sincere thanks to my family for their support and encouragement.